

# Z BOSON CROSS SECTION MEASUREMENT USING CMS AT THE LHC

*by*

JESSICA LYNN LEONARD

A dissertation submitted in partial fulfillment of the  
requirements for the degree of

DOCTOR OF PHILOSOPHY  
(PHYSICS)

*at the*

UNIVERSITY OF WISCONSIN – MADISON

2011

© Copyright by Jessica Lynn Leonard 2011

All Rights Reserved

# Z BOSON CROSS SECTION MEASUREMENT USING CMS AT THE LHC

Jessica Lynn Leonard

Under the supervision of Professor Wesley H. Smith

At the University of Wisconsin — Madison

The cross section of  $pp \rightarrow Z \rightarrow e^+e^-$  was measured for  $\sqrt{s} = 7$  TeV  $pp$  collisions at the Large Hadron Collider using the Compact Muon Solenoid detector. Well-reconstructed electrons within the region  $|\eta| < 1.4442, 1.566 < |\eta| < 2.5$  and with a transverse energy of at least 25 GeV were used, with an invariant mass window of 60 to 120 GeV. In  $36.1 \text{ pb}^{-1}$  of data, 8453 candidate events were found. The cross section was measured to be  $990 \pm 48 \text{ pb}$ , which agrees well with the NNLO prediction of 972 pb.

## Abstract

The cross section of  $pp \rightarrow Z \rightarrow e^+e^-$  was measured for  $\sqrt{s} = 7$  TeV  $pp$  collisions at the Large Hadron Collider using the Compact Muon Solenoid detector. Well-reconstructed electrons within the region  $|\eta| < 1.4442, 1.566 < |\eta| < 2.5$  and with a transverse energy of at least 25 GeV were used, with an invariant mass window of 60 to 120 GeV. In  $36.1 \text{ pb}^{-1}$  of data, 8453 candidate events were found. The cross section was measured to be  $990 \pm 48 \text{ pb}$ , which agrees well with the NNLO prediction of 972 pb.

## Acknowledgements

I would like to thank the professors who have mentored and advised me during my time as a grad student, Wesley Smith and Sridhara Dasu, as well as the scientists I have worked with over the years: Pam Klabbers, Sascha Savin, and Monika Grothe. I would also like to thank my fellow CMS students for their camaraderie and willingness to share knowledge, and my friends in Madison and in Geneva for providing a social outlet and a listening ear.

Finally, I would like to thank my family, who never stopped encouraging me throughout this journey.

# Contents

<b>Abstract</b>	<b>i</b>
<b>Acknowledgements</b>	<b>ii</b>
<b>1 Overview</b>	<b>1</b>
1.1 Short Overview of Particle Physics . . . . .	1
1.2 Introduction to the Z Boson . . . . .	5
1.3 Useful Concepts . . . . .	6
1.4 Anatomy of an Event . . . . .	7
1.5 Measurement of Cross Section . . . . .	10
1.6 Reference Frame and Coordinates . . . . .	13
1.7 General Analysis Tools . . . . .	15
1.7.1 Software . . . . .	16
<b>2 Theory of Z Boson Production</b>	<b>18</b>
2.1 The Standard Model . . . . .	18
2.1.1 Particles . . . . .	19
2.1.2 Forces . . . . .	23

2.1.2.1	Electromagnetic Force . . . . .	23
2.1.2.2	Weak Force . . . . .	23
2.1.2.3	Strong Force . . . . .	24
2.1.3	Parton Distribution Functions . . . . .	24
2.1.4	Electroweak Physics . . . . .	26
2.1.4.1	Spontaneous Symmetry Breaking . . . . .	27
2.2	Z Production . . . . .	27
2.2.1	Relativistic Kinematics . . . . .	28
2.2.2	Feynman Diagrams . . . . .	30
2.2.3	Interference from $q\bar{q} \rightarrow \gamma^* \rightarrow e^+e^-$ . . . . .	31
2.2.4	Mass Distribution . . . . .	32
2.2.5	Higher-Order Diagrams . . . . .	33
2.2.6	$Z \rightarrow e^+e^-$ Cross Section . . . . .	35
2.3	Results from Previous Experiments . . . . .	38
2.3.1	LEP . . . . .	38
2.3.2	Tevatron . . . . .	39
<b>3</b>	<b>Experimental Setup</b>	<b>41</b>
3.1	CERN . . . . .	41
3.2	Large Hadron Collider . . . . .	41
3.3	Compact Muon Solenoid . . . . .	42
3.3.1	Detection of Particle Interactions . . . . .	43
3.3.2	Coordinate System . . . . .	46
3.3.3	Magnet . . . . .	47

3.3.4	Tracker . . . . .	48
3.3.4.1	Pixels . . . . .	48
3.3.4.2	Strips . . . . .	49
3.3.5	Calorimeters . . . . .	51
3.3.5.1	ECAL . . . . .	51
3.3.5.2	HCAL . . . . .	53
3.3.6	Muon System . . . . .	54
3.3.7	Trigger . . . . .	56
3.3.7.1	Level-1 Trigger . . . . .	57
3.3.7.2	Regional Calorimeter Trigger . . . . .	58
3.3.7.3	High-Level Trigger . . . . .	62
3.3.7.4	Trigger Menus . . . . .	63
3.3.8	Luminosity . . . . .	64
<b>4</b>	<b>Event Simulation</b>	<b>66</b>
4.1	Monte Carlo Event Generation . . . . .	67
4.1.1	Types of Monte Carlo Simulation Programs . . . . .	68
4.1.2	Monte Carlo Generator Programs . . . . .	72
4.1.2.1	PYTHIA . . . . .	73
4.1.2.2	POWHEG . . . . .	75
4.1.2.3	Other Generators . . . . .	76
4.1.3	Generated Samples . . . . .	77
4.2	Detector Simulation . . . . .	80
4.2.1	GEANT Detector Model . . . . .	80



4.2.2	Level-1 Trigger Emulator . . . . .	81
<b>5</b>	<b>Event Reconstruction</b>	<b>82</b>
5.1	Detector Object Reconstruction . . . . .	82
5.1.1	Electromagnetic Calorimeter Reconstruction . . . . .	83
5.1.2	Track Reconstruction . . . . .	83
5.1.2.1	Kalman Filter . . . . .	84
5.1.2.2	Gaussian Sum Filter . . . . .	85
5.2	Electron Reconstruction . . . . .	85
5.2.1	ECAL-driven Electron Seeding . . . . .	86
5.2.1.1	Superclusters . . . . .	87
5.2.1.2	Pixel Hit-matching . . . . .	89
5.2.2	Tracker-driven Electron Seeding . . . . .	90
5.2.3	Electron Track Reconstruction . . . . .	92
5.3	Beam Spot Reconstruction . . . . .	93
5.4	Primary Vertex Reconstruction . . . . .	95
<b>6</b>	<b>Event Selection</b>	<b>97</b>
6.1	Online . . . . .	97
6.1.1	Trigger Eras . . . . .	98
6.1.2	Level-1 Trigger . . . . .	98
6.1.3	High-Level Trigger . . . . .	100
6.1.4	Primary Datasets . . . . .	104
6.2	Offline . . . . .	106
6.2.1	Electron Selection . . . . .	106

6.2.1.1	Conversion Rejection . . . . .	108
6.2.1.2	Electron Isolation . . . . .	109
6.2.1.3	Electron Identification . . . . .	109
6.2.1.4	Matching Offline-Reconstructed Objects to Trigger Ob- jects . . . . .	111
6.2.2	$Z \rightarrow e^+e^-$ Event Selection . . . . .	112
6.2.2.1	Acceptance for $Z \rightarrow e^+e^-$ Events . . . . .	112
6.2.2.2	Efficiency of Selection for $Z \rightarrow e^+e^-$ Events . . . . .	114
<b>7</b>	<b>Analysis Method</b>	<b>127</b>
7.1	Background Subtraction . . . . .	127
7.1.1	Monte Carlo Estimation . . . . .	128
7.1.2	Template Method . . . . .	129
7.1.2.1	Template Definitions . . . . .	130
7.1.2.2	Results . . . . .	132
7.1.3	Sideband Subtraction . . . . .	135
7.1.4	Comparison of Background Subtraction Methods . . . . .	137
7.2	Estimation of Systematic Uncertainties . . . . .	138
7.2.1	Introduction to Error Analysis . . . . .	138
7.2.2	Systematic Uncertainty Due to Luminosity . . . . .	141
7.2.3	Systematic Uncertainties from Theory . . . . .	141
7.2.4	Other Sources of Systematic Uncertainty . . . . .	143
7.2.4.1	Electron Energy Scale . . . . .	143
7.2.4.2	Monte Carlo Sample for Efficiency . . . . .	144

7.2.4.3	Fitting for Efficiency . . . . .	145
7.2.4.4	Background Subtraction/Modeling . . . . .	145
7.2.5	Summary of Uncertainties . . . . .	145
<b>8</b>	<b>Results</b>	<b>147</b>
8.1	Distributions of Electron Kinematic Variables . . . . .	147
8.2	Invariant Mass Spectrum . . . . .	148
8.3	Distributions of Z Kinematic Variables . . . . .	149
8.4	Cross Section Measurement . . . . .	150
8.5	Comparison to Theory . . . . .	151
8.6	Comparison to Other Experiments . . . . .	151
<b>9</b>	<b>Summary and Conclusions</b>	<b>158</b>

## List of Figures

1.1	The “plum-pudding” and the planetary atomic models. . . . .	4
2.1	Particles of the standard model . . . . .	19
2.2	Quark model of proton . . . . .	25
2.3	Feynman diagram of $q\bar{q} \rightarrow Z \rightarrow e^+e^-$ . . . . .	31
2.4	Feynman diagrams for $q\bar{q} \rightarrow Z/\gamma^* \rightarrow e^+e^-$ interference . . . . .	31
2.5	Higher-order Feynman diagrams for the process $q\bar{q} \rightarrow Z \rightarrow e^+e^-$ . . . .	33
3.1	Diagram of the LHC layout . . . . .	43
3.2	Expanded view of the CMS detector . . . . .	44
3.3	Cross-sectional view of the CMS detector . . . . .	45
3.4	Detection of particles in the CMS detector . . . . .	46
3.5	Three-dimensional display of a $Z \rightarrow e^+e^-$ event in the CMS detector .	47
3.6	Structure of pixel detector layers . . . . .	49
3.7	Diagram of layers in tracker barrel . . . . .	50
3.8	Conceptual diagram of drift tube chambers . . . . .	55
3.9	Diagram of cathode strip chamber . . . . .	55
3.10	Diagram of resistive plate chamber . . . . .	56

3.11	Structure of the Level-1 trigger . . . . .	58
3.12	Diagram of the RCT structure . . . . .	59
3.13	Diagram of the RCT electron/photon algorithm . . . . .	61
3.14	Diagram of the RCT $\tau$ algorithm . . . . .	62
3.15	Luminosity collected by CMS as a function of time, 2010 . . . . .	65
4.1	Diagram of typical steps used to simulate event in parton shower method	72
4.2	Schematics showing the Lund string model of hadronization . . . . .	75
5.1	The $\phi$ difference between Monte Carlo generated electrons and recon- structed tracks . . . . .	86
5.2	Typical energy distribution in a basic cluster . . . . .	87
5.3	Illustration of the “Hybrid” supercluster algorithm . . . . .	89
5.4	Illustration of the “Multi5x5” supercluster algorithm . . . . .	90
5.5	Schematic of pixel-hit search algorithm in electron-seeding . . . . .	91
5.6	Electron (GSF) track reconstruction efficiencies . . . . .	93
5.7	Electron energy resolution from ECAL, tracker, and combined . . . . .	94
6.1	Efficiency as a function of reconstructed supercluster $E_T$ for Level-1 triggers . . . . .	101
6.2	Efficiency as a function of reconstructed supercluster $E_T$ for an early HLT trigger . . . . .	104
6.3	Conversion rejection variables after $E_T$ cut . . . . .	120
6.4	Electron tracker isolation variables after $E_T$ and conversion rejection cuts	121

6.5	Electron ECAL isolation variables after $E_T$ , conversion rejection, and tracker isolation cuts . . . . .	122
6.6	Electron HCAL isolation variables after $E_T$ , conversion rejection, and tracker and ECAL isolation cuts . . . . .	123
6.7	$\Delta\eta_{in}$ electron identification variables after $E_T$ , conversion rejection, and isolation cuts . . . . .	123
6.8	$\Delta\phi_{in}$ electron identification variables after $E_T$ , conversion rejection, isolation, and $\Delta\eta_{in}$ cuts . . . . .	124
6.9	$\sigma_{i\eta i\eta}$ electron identification variables after $E_T$ , conversion rejection, isolation, $\Delta\eta_{in}$ , and $\Delta\phi_{in}$ cuts . . . . .	124
6.10	H/E electron identification variables after $E_T$ , conversion rejection, isolation, $\Delta\eta_{in}$ , $\Delta\phi_{in}$ , and $\sigma_{i\eta i\eta}$ cuts . . . . .	125
6.11	Example of tag-and-probe fits . . . . .	126
7.1	Shapes of signal and background templates used in template method of background subtraction . . . . .	133
7.2	Results of template fit to data . . . . .	134
7.3	Functional fit of $Z \rightarrow e^+e^-$ invariant mass peak for background sub- traction . . . . .	136
8.1	Reconstructed electron $p_T$ , $\eta$ , $\phi$ spectra after full selection . . . . .	153
8.2	Electron-pair invariant mass after full selection . . . . .	154
8.3	Electron-pair invariant mass by $\eta$ region . . . . .	155
8.4	Kinematic quantities of Z candidates after full selection . . . . .	156
8.5	LHC $Z \rightarrow e^+e^-$ cross section results, with Tevatron results and theory	157

# List of Tables

2.1	Masses and charges of the Standard Model particles . . . . .	20
2.2	Charge and third component of weak isospin for left-handed Standard Model fermions. . . . .	37
2.3	Electron-positron Z production cross sections, measured by LEP exper- iments . . . . .	39
2.4	Proton-antiproton Z production cross sections, measured by Tevatron experiments. . . . .	40
4.1	Monte Carlo samples used in this analysis . . . . .	78
6.1	Trigger paths used to select data . . . . .	102
6.2	Primary datasets used in this analysis. . . . .	105
6.3	WP80 thresholds for relative isolation . . . . .	110
6.4	WP80 thresholds for electron identification variables . . . . .	111
6.5	Criteria for determining acceptance of $Z \rightarrow e^+e^-$ events . . . . .	113
6.6	Acceptance values for $Z \rightarrow e^+e^-$ events . . . . .	114
6.7	Individual efficiencies of electron selection steps . . . . .	119
6.8	Efficiencies of trigger paths used in data . . . . .	119

7.1	Number of events passing full selection for each background, estimated from Monte Carlo simulation. . . . .	128
7.2	Summary of the standard working point and the working points used in the template method. . . . .	131
7.3	Signal and background fractions of data sample . . . . .	135
7.4	Summary of background estimates from different methods . . . . .	138
7.5	Summary of uncertainties . . . . .	146
8.1	Quantities used to calculate cross section. . . . .	151



# Chapter 1

## Overview

It is natural for humans to wonder how the world works. Small children commonly ask a plethora of questions, sometimes pushing their parents to the point of exasperation. I was one such child, always asking questions, and later devouring books and magazines, with a hunger to learn more. My first exposure to particle physics came at age eleven when I discovered my parents' copy of *A Brief History of Time* by Stephen Hawking. The ideas described therein – fundamental particles with exotic properties, the flexible nature of spacetime, what might lie beyond the edges of our understanding – boggled my mind, and I loved it. Over the following years I checked out much of the local library's collection of popular physics books. It is this desire to know more about the fundamental nature of the universe that has brought me to the point of pursuing a doctorate in experimental particle physics.

### 1.1 Short Overview of Particle Physics

This hunger to figure out how things work has long been a part of human life. One of the most lasting questions has been “What, exactly, are things made of?” The ancient Greeks tried to distill all matter into four elements: fire, earth, water, and

air. They also came up with the idea of an “atom,” the smallest possible piece of matter, a piece that could be divided no further. Natural philosophers through the ages discovered various chemical elements. However, not until relatively recently was the concept of the atom accepted scientifically. Up until the late 19th century, the issue was still debated. Dmitri Mendeleev’s organization of the elements into a table according to the similarity of their properties hinted at an underlying structure. In addition, an atomic theory explained certain features of the behavior of gases, as applied by Ludwig Boltzmann and Amedeo Avogadro. However, the issue was not fully settled until the beginning of the 20th century. During this period Albert Einstein used an atomic theory of matter to explain the random motion of particles in a fluid (called Brownian motion after Robert Brown, who first observed it), and Jean Perrin verified the theory experimentally. Around this time progress was also being made on investigations into the structure of the atom. J.J. Thomson discovered that the cathode rays he was working with were made up of light, negatively-charged particles, dubbed electrons. He believed that these particles formed atoms, electrons floating in a sea of positive charge so that the overall element was electrically neutral: the so-called “plum pudding model.” However, experiments by Ernest Rutherford shooting positively-charged alpha particles at a sheet of gold foil demonstrated that the atom included a hard, positively-charged nucleus, illustrated in Figure 1.1. This led Rutherford to propose the planetary model of the atom, in which the positive nucleus is orbited by a cloud of negative electrons. The model did not explain why the electrons did not lose energy and fall into the nucleus, though; this explanation came when Niels Bohr applied a quantized idea of energy to the atom. The quantum theory of

light, proposed by Max Planck and Albert Einstein, said that light existed in packets of a given energy, known as quanta. Applied to the atom, it meant that electrons were only permitted to possess energy and angular momentum in discrete steps. They moved between these energy levels by absorbing or emitting light of specific energies. Rutherford later noticed that the atomic masses were roughly integer multiples of the hydrogen mass; he proposed that atomic nuclei were made of positively-charged protons, and later added electrically neutral neutrons to make up the needed leftover mass. Meanwhile, quantum mechanics was soon formulated to describe the properties of particles' behavior in terms of waves of quantized energy. Paul Dirac formulated a quantum theory that was consistent with Einstein's special relativity, which dealt with motion at speeds approaching that of light. In addition, the idea of forces being mediated by the exchange of force particles was gaining traction: quantum electrodynamics formulated the electromagnetic force as the interaction between charged particles and photons, or particles of light. At this point many new particles were being discovered, including the pion, the positron, and the muon, along with a large number of heavier particles. Quarks were proposed in Murray Gell-Mann's "Eightfold Way" to explain the many new heavy particles being found. The quark model successfully explained the properties of neutrons and protons: those particles along with some of the new discoveries were "baryons," made up of three quarks, while other new particles were "mesons," made up of a quark and an anti-quark. The force between the quarks was the same one keeping the protons and neutrons together inside the atomic nucleus, mediated by particles called gluons. Since it was strong enough to overcome the repulsion between the positively-charged protons, it was called the strong force. Another

force, called the weak force, was known to be responsible for the decay of neutrons into protons. Through the development of modern particle theory, it was predicted that heavy particles mediated this force. The discoveries of these particles, the W and the Z bosons, marked a success for the current theory: it had predicted particles that had previously been undiscovered.

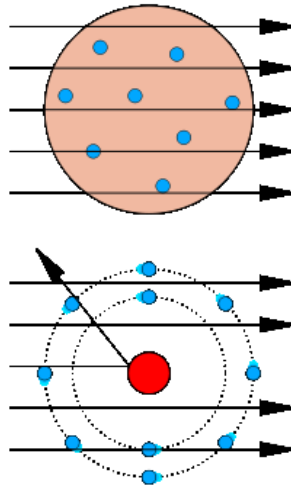


Figure 1.1: The “plum-pudding” and the planetary atomic models. Observations showed incident particles back-scattering consistent with the dense, positive nucleus of the planetary model.

Experiments making all these particle discoveries have progressed from observing cosmic rays in cloud chambers and bubble chambers to observing collisions created in higher- and higher-energy accelerators (hence the current name of the field, “high-energy physics”). Most recently, the last of the six quarks, the top quark, was discovered at the Tevatron accelerator in 1995 [1] [2]. All these particles and their interactions are described within the framework of the Standard Model of particle physics; the Standard Model combines the quantum electrodynamics of charged par-

ticles and photons, the quark and gluon model, called quantum chromodynamics, and the interactions of the weak force into one framework. The Standard Model will be further explained in Chapter 2. Currently, the Standard Model is considered to be the primary description of particle physics. However, it predicts one particle that has not yet been observed, the Higgs boson. Finding the Higgs and verifying this last piece of the Standard Model is one of the current goals of particle physics. However, there are observations that the Standard Model cannot explain, such as the fact that neutrinos have mass. The Standard Model is also incomplete in that it does not incorporate the last fundamental force, gravity. Further, some physicists think that various additions to the Standard Model make it more elegant. These new models predict various new particles. Therefore, scientists are also on the lookout for any evidence of particle physics existing outside the Standard Model.

## 1.2 Introduction to the Z Boson

This analysis studies the production of the Z boson. The Z is one of the particles that mediates the weak force. It was first observed in decays to oppositely-charged electrons and muons at the Super Proton Synchrotron (SPS) accelerator at CERN in 1983 [3], [4].

The Z has a relatively large mass, like the other mediator of the weak force, the W; however, unlike the electrically-charged W, the Z is chargeless. The Z interacts with all matter particles; it can be formed in a high-energy interaction between two particles that are oppositely-charged but otherwise alike. This includes the quark constituents of protons, which means it can be formed in the proton-proton collisions of the LHC. The Z can also decay into similar pairs of particles, one such possible pair

being the electron and the positron; this is the decay studied in this analysis.

The Z has been well-studied in previous experiments, particularly at the Large Electron-Positron (LEP) and Tevatron colliders (Section 2.3), which makes it an ideal initial study for the LHC experiments [5]. Its mass is known well enough to be used to calibrate the experiments. In addition, the fact that the Z is produced from the constituents of protons means that it can shed light on the protons' internal structure. The Z also tends to decay in a similar way as the proposed Higgs boson: to two oppositely-charged particles. A particular Z decay signature may look like the Higgs and vice versa. Therefore, in order to look for the Higgs, the decays that may resemble it must be very well-studied. This way, if the Higgs is seen, it will clearly be something new.

This analysis measures the cross section (see Section 1.5) of the Z produced in proton-proton collisions as it decays to an electron and a positron. The result of this measurement can be used to validate the predictions of the current model of particle interactions.

### 1.3 Useful Concepts

A few definitions and concepts should be introduced before moving on to more specific explanations of the analysis. In the following pages, much will be described by the word “kinematic” or “kinematics.” This refers to the properties of position or motion. So, “kinematic criteria” means selections applied according to quantities such as momentum or angle. Often, a calculation may need to deal with the full range of possible values for multiple quantities, or the “phase space.” Phase space refers to the collection of total possible values for a set of quantities. A given system is represented

by one set of values out of that collection. For some calculations it is necessary to include contributions from the entire phase space, for example integrating over all possible angles for a particle's direction.

Experimental particle physics observations are built on “events.” An event is the name for a particle interaction that has been captured and recorded by the detector. In general, events caused by the specific process being studied are termed “signal,” while events from other sources are called “background.” A significant part of any analysis is designing criteria that select signal events while rejecting background events, so that the analysis focuses only on data containing the signal process. The number of events for a given signal can be used to calculate quantities of interest, for example how often that process occurs relative to others.

Energies at this scale are typically measured in GeV, or giga-electron-volts. One electron-volt (eV) is the amount of energy an electron gains from one volt of potential difference. At the GeV level ( $10^9$  eV), particles essentially move at the speed of light.

## 1.4 Anatomy of an Event

A proton-proton interaction begins with beams of protons accelerated in opposite directions. The protons are formed into “bunches,” with many, many millions of protons per bunch. These beams of proton bunches are directed to cross at the center of the detector. In an encounter between two protons, the fundamental interaction takes place between individual “partons,” which is the collective term for the quarks and gluons that make up the proton. Each “bunch crossing” results in a small number of interactions, the majority of which do not produce high-enough energy particles in the detector to be interesting. However, sometimes two partons from separate

protons interact very strongly. These are the types of interactions that are typically interesting. An interaction in which the partons interact very energetically is a “hard interaction.” Conceptually, the partons “hit each other hard.” Hard interactions are detected by having end-product particles with high momentum (tens of GeV) in the transverse direction, perpendicular to the protons’ original direction of motion. In hard interactions the original proton momentum is disturbed significantly, while in “soft,” or low-energy, interactions, most of the protons’ momentum continues in the same direction, down the beam-pipe.

Oftentimes the two partons exchange a particle, such as a photon or gluon. In other cases another particle is produced, such as a Z boson; this is the scenario studied in this analysis. Particles formed in this way are typically heavy and therefore short-lived, decaying into lighter, more stable particles. The Z, for example, has a mean lifetime of  $3 \times 10^{-25}$  seconds. This analysis studies the Z’s decay into an electron and its antiparticle, the positron, which are the lightest charged particles and therefore (to conserve charge) do not themselves decay. These decay products are what fly “out” into the detector with some energy and direction, and it is these quantities that are measured by the detector.

However, additional processes may contribute to the signature left in the detector. One of the initial partons or final decay products may radiate additional particles (photons or gluons) which end up in the detector. This is known as “initial-state radiation” (ISR) and “final-state radiation” (FSR) respectively. In addition, there are two ways that particles unrelated to the hard interaction may show up in the detector: underlying event and pileup. The “underlying event” refers to the interactions taking



place between the proton remnants, the constituents of the proton not participating in the hard interaction. “Pileup” refers to any interactions that happen between other protons in the bunch. Statistically, at most only one hard interaction happens in any given bunch crossing; the rest are soft. Both underlying event and pileup can contribute energy deposits that are recorded as part of the event. Typically they are both fairly low-energy and therefore easily filtered out as background.

Fully-decayed, end-product particles leave a signature in the detector by interacting with its material. Some detector material emits light when particles pass through; in these materials, the amount of light is proportional to the energy of the particle. Other parts of the detector rely on an electric signal generated as the particle passes by. These particle interactions with the detector are collectively known as “hits.” In the process of reconstruction, hits are linked together to follow the path of the particle that caused them. For example, a series of hits in the tracker could show the trajectory of a charged particle as it passed through. The curvature of the trajectory could be measured and turned into a value for the momentum, knowing the value of the magnetic field. This track could then be linked with a significant emission of light in the calorimeter. If the energy from the light matches the momentum from the track, this object is reconstructed as an electron. A rough, on-the-fly reconstruction process takes place in real time to decide whether or not to save the event, called triggering. Saved events undergo a more thorough reconstruction of their detector signals later, since this more thorough version takes too long to do in real time. However, not all objects reconstructed as a given particle are actually due to a real particle of that type passing through the detector: some reconstructed objects are

“fakes.” These fakes are typically selected out by more stringent criteria on various particle properties. However, this selection is done at the analysis level, not during reconstruction.

## 1.5 Measurement of Cross Section

The cross section, the quantity being calculated in this analysis, is a measure of “how often things happen.” However, it is not measured as a rate (occurrences per unit time); instead it is measured as a cross-sectional area and represents the probability of the given interaction occurring. An analogy may be made to trying to hit a target with a tennis ball. The bigger the target is, the more likely you will be able to hit it. The sizes of both objects matter: a trajectory that would cause a tennis ball to just miss the target would cause a basketball to clip the edge, solely because of the basketball’s larger size. Therefore “cross section” may be more precisely defined as the effective cross-sectional area of the target, taking into account the sizes of both the target and the projectile. When both the target and projectile are particles, they may interact “at a distance,” that is, without “touching” each other, through the fundamental forces. (For example, electrons are thought to be point particles and therefore have no spatial extent, but they still attract and repel other particles through the electromagnetic force.) This interaction-at-a-distance increases the effective cross section. A particular interaction between two particles that interact strongly with each other has a large cross section: the cross section depends on the strength of the force between them.

According to the definition, “interaction cross section” applies only to the colliding particles. However, a cross section is usually associated with the entire process,

including the decay, such as (in this case)  $q\bar{q} \rightarrow Z/\gamma^* \rightarrow e^+e^-$ . Here, the number calculated as the cross section takes into account only those events where a  $Z/\gamma^*$  is formed, as well as the fact that only some of those events decay into electrons. The fraction of events that decay to a certain final state is known as the branching ratio, abbreviated BR. When it is not explicitly mentioned along with the cross section for a given final state, it is understood to be included. Adding up the cross sections for all of these possible interactions would give the full proton-proton interaction cross section.

The cross section  $\sigma$  is related to the event count  $n$  by

$$n = \sigma \times \mathcal{L}$$

$\mathcal{L}$  in this equation is the “luminosity,” a measure of the number of proton collisions. Two types of luminosity are spoken of in particle physics: instantaneous luminosity and integrated luminosity. Instantaneous luminosity, denoted here by  $L$ , refers to the rate of potential proton interactions. Specifically, it is defined as the number of protons passing through a given area in a given amount of time. (The units are therefore  $\frac{1}{\text{area} \times \text{time}}$ , typically  $\text{cm}^{-2}\text{s}^{-1}$ .) If the same number of protons are squeezed into a smaller area, the instantaneous luminosity is higher; the protons in the colliding beams are more likely to interact. This is analogous to trying to walk through a room with many other people in it; you are much more likely to bump into people in a small, crowded room than a large room in which the people are more spread out. Integrated luminosity, or  $\mathcal{L}$  here, is the instantaneous luminosity accumulated over a definite period of time, effectively the total number of protons that have passed through a unit of area. (Integrated luminosity is measure in units of  $\frac{1}{\text{area}}$ , the conventional unit

being powers of the *barn*, equal to  $10^{-28}\text{m}^2$ .) It is a measure of the total amount of data gathered. The luminosity in the above equation refers to the integrated luminosity. Essentially, the equation says that the total amount of data (the luminosity) times the likelihood a specific interaction will happen (the cross section) gives you the total number of events of that type that have happened (the event count,  $n$ ). In practice this formula must be modified to account for the natural limitations of the detector: Two new factors,  $A$  and  $\epsilon$ , must be introduced.  $A$ , the “acceptance,” accounts for the fact that the detector cannot be designed in a way that allows it to see every possible particle. In particular, any particles that continue in the direction of the proton beam will be lost – the presence of the beam pipe precludes detector material in that direction. The value of the acceptance is the fraction of the events that can theoretically be seen by the detector, often defined in terms of a region of kinematic phase space: “above energy  $X$  and within angular constraints  $Y$ .” For simplicity’s sake, these constraints are typically chosen to include only regions of the detector and particle energies for which the particles of interest can be well-reconstructed. The “efficiency,”  $\epsilon$ , takes into account the fact that even for particles that leave a definite signature in the detector, they may still not be recorded as such. High efficiency is a primary goal of any experiment, but the sources of inefficiency can never be completely eliminated. The efficiency is often broken down into efficiencies of the individual steps:

$$\epsilon = \epsilon_{trig} \times \epsilon_{reco} \times \epsilon_{sel}$$

The individual efficiencies correspond to triggering, reconstruction, and selection. The boundary between what is considered for the acceptance versus for the efficiency is somewhat fluid: failing to record a particle with a very low energy may be considered

an issue of acceptance (because the detector is not designed for such small energies) or a matter of efficiency (because though the particle left a signature in the detector, it was not reconstructed). It is merely a matter of definition, and in the end result makes no difference.

The inclusion of acceptance and efficiency turn the previous expression of event count and cross section into

$$n = \sigma \times \mathcal{L} \times \epsilon \times A$$

The number of events actually seen ( $n$ ) is reduced by the factors accounting for the detector limitations. In order to calculate the cross section  $\sigma$  (including the branching ratio) of the  $q\bar{q} \rightarrow Z/\gamma^* \rightarrow e^+e^-$  interaction, which is the quantity this analysis aims to get, the equation must be rearranged into

$$\sigma_Z \times \text{BR} (Z \rightarrow ee) = \frac{n_{Z \rightarrow ee}}{\mathcal{L} \times \epsilon \times A}$$

Now  $\sigma \times \text{BR}$  is expressed in terms of other quantities which can be measured or calculated. This equation is the heart of this analysis. The “meat” of the analysis is then measuring the quantities that combine to make up the cross section,  $n$ ,  $\mathcal{L}$ ,  $\epsilon$ , and  $A$ , and putting it all together.

## 1.6 Reference Frame and Coordinates

For some high-energy physics experiments, there is a choice of several reference frames that can be used for measurement, each with its own benefits. However, in the case of proton-proton collisions, the logical reference frame for measurements is the frame at rest with respect to the detector, the “lab frame,” because it is the same as the proton-proton center-of-momentum frame. Therefore all measurements are done

in the lab frame.

A particular set of coordinates is often used to describe the direction of outgoing or intermediate particles. The direction of the incoming particles defines an axis, the beam axis. The azimuthal angle, measured around this axis and analogous to longitude on the earth's surface, is labeled  $\phi$ . The angle along the axis, the polar angle (analogous to latitude), is labeled by  $\theta$ . However, it is much more common to measure this angle in terms of pseudorapidity,  $\eta$ , which is given as a function of  $\theta$ :

$$\eta = -\ln \left[ \tan \left( \frac{\theta}{2} \right) \right]$$

$\eta$  is preferred because of its relation to another quantity, rapidity,  $y$ , which is a function of the particle's energy and momentum:

$$y = \frac{1}{2} \ln \left( \frac{E + p_L}{E - p_L} \right)$$

where  $p_L$  is the longitudinal component of the particle's momentum (the component parallel to the beam axis). Rapidity is useful when dealing with relativistic speeds, such as those at which the particles typically travel in this experiment. When viewed from separate reference frames that are moving at relativistic speeds with respect to each other, a particle's speed, direction, and energy appear to be different. However, rapidity has special status in that the difference in rapidity between two particles does not change when the reference frame is changed. A particle's rapidity can be approximated by the pseudorapidity if it is very light or traveling very fast (pseudorapidity is identical to rapidity if the particle has zero mass, in which case it is also moving at the speed of light). In addition, outgoing particles tend to be distributed uniformly in terms of rapidity, as opposed to the polar angle  $\theta$ , which does not enjoy the same

uniform distribution. Pseudorapidity is used as the coordinate because it is easily computed from the location of the particles' signatures in the detector. Rapidity is calculated in cases where the particle of interest may be heavy and may not have a high speed, for example the Z boson examined in this analysis.

Differences between particle positions are often given in terms of  $\Delta\eta$  and  $\Delta\phi$ ; a two-dimensional angular distance  $\Delta R$  can also be defined as

$$\Delta R = \sqrt{\Delta\eta^2 + \Delta\phi^2}$$

This is useful when requiring that particles be at least a certain distance apart.

## 1.7 General Analysis Tools

A few concepts are common to particle physics analyses and should be mentioned in general.

One of the primary tools in an analysis is a type of data graph known as a “histogram.” A histogram is a graphical representation of a data set, used often in statistical analysis. In general, each point in the data set has a value, and the points are grouped into intervals or “bins” according to that value. These histograms show distributions of a particular quantity, for example an electron's energy. Having more events than expected in a certain bin or a series of bins can signal some new physics process. The benefit of grouping the data into bins is that the bins can be widened or narrowed, according to how many events are being studied. For very few events, wide bins are used in order to get a statistically significant number of events in each bin. For very many events, when statistical significance is not as much of an issue, narrow bins are preferable, up to the resolution of the variable being plotted: the shape of the

distribution can be seen in more detail. In general, any distribution mentioned means a histogram has been used.

One particularly useful tool in particle physics is the ability to simulate events. The current machinery (described in detail in Chapter 4) encompasses what is known about particles and how they interact. Comparing distributions from the simulated data, what is expected, to those from real data, what actually happened, can aid in the discovery of new physics: something that was not expected will not be in the simulation. Some new physics scenarios are included in various simulation programs, so any potential discovery can be checked against those predictions to see if they agree.

However, the simulations may not be theoretically complete, or may include defects that noticeably affect the output. The term “data-driven” is used to describe an analysis method that uses only real data, taken with the detector, instead of relying on simulated data. The purpose of using a data-driven method is to eliminate the possibility of a physics result being affected by an error or inaccuracy in the simulation itself. Since some quantities, such as efficiency, are much easier to measure using simulated data, devising data-driven methods to measure those quantities is an important and potentially challenging part of analysis.

### **1.7.1 Software**

This analysis made use of many software packages to perform specific functions within the process of analyzing the data. Most of the software will be explained in the chapter to which each piece is particularly relevant. However, two programs in particular served many purposes throughout the whole of the analysis and should therefore be mentioned separately. The CMS Software (CMSSW) framework [6] is



the collaboration-developed software used for many aspects of CMS operation and use. It encompasses data-taking, reconstruction, simulation, and analysis. ROOT [7] is a general data analysis package, written in C++, and developed and maintained at CERN. It is widely used in the field of experimental particle physics. ROOT implements many tools and functions necessary to various types of analysis, such as histograms, fitting, and statistics. CMSSW can interface with ROOT, providing access to ROOT's capabilities within a CMSSW analysis setting.

## Chapter 2

# Theory of Z Boson Production <sup>1</sup>

Any physics analysis must be based on a solid understanding of the underlying theory and mathematics. This chapter's aim is to introduce the context for a Z production cross section analysis.

### 2.1 The Standard Model

The Standard Model describes the current understanding of how fundamental particles interact. There are three different types of particles: quarks and leptons, which make up matter, and bosons, which transmit forces. Quarks and leptons are collectively called fermions; two fermions cannot exist in the exact same state. Bosons do not have this constraint; many bosons can be in the same state. The particles are shown in Figure 2.1, with more detailed information given in Table 2.1. The first three columns of the figure show the first three generations of the quarks and leptons, while the last column shows the bosons. Each fermion generation contains two quarks, a neutrino, and a charged lepton. In general, the generations get progressively heavier. The electron is lighter than the muon, which is lighter than the  $\tau$ . The same relation

---

<sup>1</sup>Much of the material for this chapter was taken from [8].

exists between the quark generations; the top quark is the heaviest known particle in the Standard Model. Normal, everyday matter is made up solely of particles from the first generation. All normal matter is made of atoms, which in turn consist of a nucleus and electrons surrounding the nucleus. Atomic nuclei are made of protons and neutrons, which are made of up and down quarks: the proton by  $uud$  and the neutron by  $udd$ .

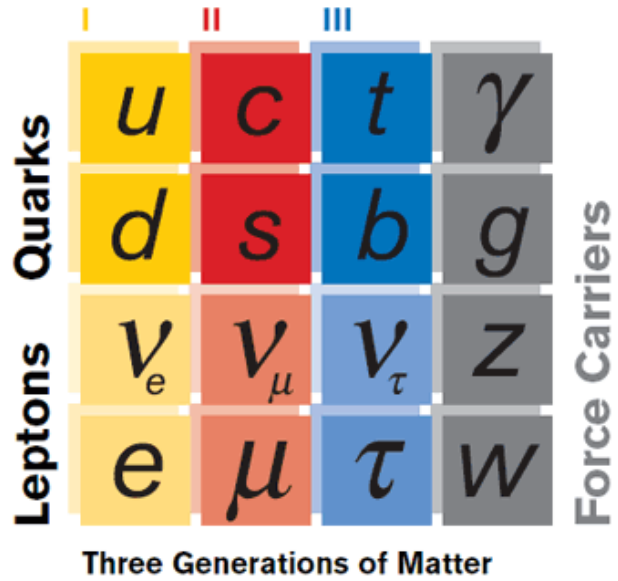


Figure 2.1: Known particles of the standard model, represented in three generations.

### 2.1.1 Particles

There are six “flavors” of quarks, often represented by their first letters: up ( $u$ ), down ( $d$ ), charm ( $c$ ), strange ( $s$ ), top ( $t$ ), and bottom ( $b$ ). The first quark in each pair has charge  $+\frac{2}{3}$ , while the second has charge  $-\frac{1}{3}$ . These charges are given in terms of the electron charge; though the charges are fractional, the quarks are always

Table 2.1: Masses and charges of the Standard Model particles, as well as forces they are subject to.

Particle	Mass (GeV)	Charge (e)	Weak	EM	Strong
Quarks					
up, $u$	$2.5 \times 10^{-3}$	$+\frac{2}{3}$	Yes	Yes	Yes
down, $d$	$5.0 \times 10^{-3}$	$-\frac{1}{3}$	Yes	Yes	Yes
charm, $c$	0.10	$+\frac{2}{3}$	Yes	Yes	Yes
strange, $s$	1.29	$-\frac{1}{3}$	Yes	Yes	Yes
top, $t$	173	$+\frac{2}{3}$	Yes	Yes	Yes
bottom, $b$	4.2	$-\frac{1}{3}$	Yes	Yes	Yes
Leptons					
electron, $e$	$0.511 \times 10^{-3}$	-1	Yes	Yes	No
muon, $\mu$	$106 \times 10^{-3}$	-1	Yes	Yes	No
tau, $\tau$	1.78	-1	Yes	Yes	No
electron neutrino, $\nu_e$	$< 2 \times 10^{-6}$	0	Yes	No	No
muon neutrino, $\nu_\mu$	$< 2 \times 10^{-6}$	0	Yes	No	No
tau neutrino, $\nu_\tau$	$< 2 \times 10^{-6}$	0	Yes	No	No
Bosons					
photon, $\gamma$	0	0	No	No	No
$W^\pm$	80.4	$\pm 1$	No	Yes	No
$Z$	91.2	0	No	No	No
gluon, $g$	0	0	No	No	Yes

arranged into composite particles that have integer multiples of the electron charge. These composite particles are known as “hadrons” and are divided into two categories: “mesons,” made of a quark and an antiquark, and “baryons,” made of three quarks (or three antiquarks).

The leptons consist of the electron, muon, and tau ( $\tau$ ), each with charge -1, and their corresponding neutrinos, the electron neutrino, muon neutrino, and  $\tau$  neutrino, which are chargeless. Until recently it was believed that all the neutrinos are massless. However, recent results indicate that neutrinos do have a small mass [9].

The bosons in the last column transmit the forces by which particles interact. The massless photon ( $\gamma$ ) transmits the electromagnetic (EM) force; this particle is more familiar in its everyday context as the particle that makes up light. The gluon ( $g$ ), also massless, transmits the strong force, which holds protons and neutrons together (like glue, hence the name). The relatively heavy  $Z$  and  $W$  bosons transmit the weak force, which causes nuclear decay. Each force has an intrinsic strength, represented by its “coupling constant.” The strong force’s coupling constant ( $\alpha_S$ ) is larger than that of the electromagnetic force ( $\alpha$ ); the weak force’s ( $G_F$ ) is weaker.

In general, each particle has an antiparticle partner, often denoted by a bar ( $\bar{u}$ ), of the opposite charge and quantum numbers; quantum numbers are used to describe the properties of the particles and corresponding interactions. For instance, all leptons have a non-zero “lepton number;” if the initial state of a set of particles has a total lepton number of 1, then any interaction between those particles will result in a final state with the same lepton number. Lepton number is always conserved in this way, as are charge and other quantum numbers. The antiparticle of the electron ( $e^-$ ) has the

opposite charge and lepton number and is called the positron ( $e^+$ ). Neutrinos, being chargeless, have antineutrinos with opposite lepton number. Quarks and gluons have another quantum “number” known as color. The three colors are red, green, and blue, with the corresponding “anti-colors” being anti-red, anti-green, and anti-blue. Color is unique in that all observed states of quarks and gluons are “colorless.” In two-quark states, a color and its anti-color “combine” to make a colorless state. Three-quark states are also colorless, but through a different combination: the three quarks are colored red, green, and blue (or the corresponding anticolors), which “combine” (like colored light) to form a state with no color. In practice, antiparticles are often called by their particle names; since it is known that a neutral Z must decay to one positive and one negative particle, no distinction is made between “positron” and “electron” – both are called “electrons.”

Not shown in Figure 2.1 is the Higgs boson, which is predicted by the Standard Model to give mass to the other particles. The Higgs has not yet been discovered; finding it (if it exists) is one of the goals of the LHC.

The Standard Model does not include the final fundamental force, gravity. Gravity is the weakest of the forces and does not measurably affect interactions between fundamental particles. The reason that it is the only one observable on a cosmological scale is because its “charge,” mass, is cumulative; there is no anti-mass to counter it the way a negatively-charged electron and a positively-charged proton combine to make an electrically neutral hydrogen atom. Gravity has been described on a macroscopic scale, but so far no theory has fully united gravity with the other fundamental forces. Such a “theory of everything” is one of the goals that theoretical physics pursues.

### 2.1.2 Forces

The forces in the Standard Model can be described by group mathematics. A “group” is a set of elements with specific properties. In particular, a transformation applied to an element in the group results in another element in the group. A “Lie” group is one in which any transformation can be done in very small steps, each of which results in an element still in the group. The different fundamental forces are each described by such a Lie group. Each group is represented by a set of square matrices of some dimension, given by the number in parentheses in the name of the group. The matrices used for these representations are all unitary (hence the common “U” designation). “Unitary” means that the matrix’s inverse is equal to its complex conjugate transpose. In other words, if you flip the matrix’s elements about its diagonal and replace each imaginary unit  $i$  with  $-i$ , then multiply it by the original matrix, the result is the identity matrix  $I$ .

#### 2.1.2.1 Electromagnetic Force

The electromagnetic force is described by the  $U(1)$  group. Essentially, this describes rotation about an axis. The single parameter (an angle) requires only one matrix, corresponding to a single force carrier, the photon. The electromagnetic force causes interactions between photons and any particles that have electric charge. This includes quarks, leptons, and the charged weak bosons.

#### 2.1.2.2 Weak Force

The weak force is described by the  $SU(2)$  group. The “S” addition in the name stands for “special” and means that each matrix’s trace (the sum of elements along

the matrix's diagonal) is zero.  $SU(2)$  represents rotations in three dimensions using three matrices, and therefore has three parameters corresponding to the single angle of  $U(1)$ . These give rise to the three carriers of the weak force, the two oppositely-charged  $W$ 's and the  $Z$ . The weak force acts on any particles that have the “weak version” of electrical charge, namely all fermions. In particular, the weak force is the only way neutrinos interact.

### 2.1.2.3 Strong Force

Finally, the strong force is represented by  $SU(3)$ , which does not have an easy analogy to rotations like the previous two groups. It uses eight matrices, which correspond to the eight different gluon states that mediate the force. The three dimensions of the group relate to the three “color charges,” red, green, and blue. Strong force interactions happen between all particles that carry this color charge, namely quarks, but also gluons themselves. This so-called self-interaction on the part of the gluons causes the strong force to increase with distance. At short distances, the quarks making up another particle essentially act free; only when they get further apart do they feel the force keeping them in their bound state. This situation is related to the fact that quarks are never observed alone, only within these bound states. An interaction that is energetic enough to cause quarks to separate is also energetic enough to create more quarks with which the original quarks form new bound states.

### 2.1.3 Parton Distribution Functions

Since quarks do not exist in an isolated state outside hadrons, any interaction between them must take into account the structure of those hadrons, in this case



protons. The quark structure of protons is given by a set of functions called “parton distribution functions” or PDFs,  $f_i(x)$ . These functions represent the probability of finding a given quark flavor  $i$  inside the proton with a given momentum. The quark’s momentum itself is not used; rather, the functions depend on the fraction of the proton’s momentum that the quark carries, or  $x$ . Since no quark can have momentum greater than that of the proton itself, the value of  $x$  ranges from 0 to 1. A proton is said to consist of two up quarks and a down quark; however, these represent the “valence” quarks only. A “sea” of quarks is also present, formed from gluons and each existing only momentarily, illustrated in Figure 2.2. Therefore the PDFs represent all quark flavors, not just  $u$  and  $d$ .

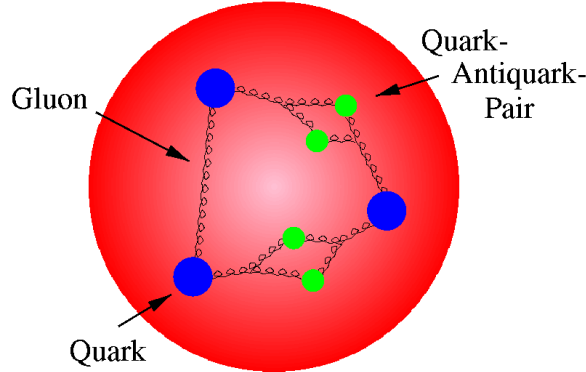


Figure 2.2: Quark model of the proton, showing the three valence quarks and the quark-antiquark pairs that make up the quark sea.

PDFs cannot be calculated from first principles and must be measured by fits to experimental data. The simulated signal samples used in this analysis were generated with the CT10 PDF set [10], while the theoretical cross section calculation used the MSTW set [11]. The background samples used a slightly older version of CT10 called

CTEQ6L1 [12]. The currently-distributed PDF sets account for data from all major past experiments. However, there is still some uncertainty, and precision measurements of Z production at the LHC can improve the knowledge of PDFs.

#### 2.1.4 Electroweak Physics

The forces have been given in terms of mathematical groups. However, the individual groups by themselves do not necessarily represent the reality of particles. It is known experimentally that the bosons carrying the weak force have mass. In order for the theory to correctly predict the fact those particles should be massive, the electromagnetic and weak interactions had to be combined into a single framework,  $SU(2) \times U(1)$ , using a specific method. The integrated  $SU(2) \times U(1)$  group allows for the collective four force-carrying bosons (photon, positively- and negatively-charged W's, and Z) to be described as compositions of the same underlying states. The electroweak interaction has its own set of quantum numbers: “weak isospin,” and “hypercharge;” hypercharge combines weak isospin with electric charge.  $T_3$  is the third component of the weak isospin and relates to how the fermions are arranged within the standard model generations (refer back to Figure 2.1). Each generation consists of two pairs, one pair of quarks and one pair of leptons. The placement of each particle within its pair reflects how it interacts with the weak force. For the upper particle in each pair, the hypercharge is  $+\frac{1}{2}$ ; for the lower particle, it is  $-\frac{1}{2}$ . (Note: this only applies to particles whose spin is “left-handed,” or oriented to spin left with respect to its direction of motion. Particles with “right-handed” spin have zero weak isospin; right-handed neutrinos do not interact in the Standard Model. This is equivalent with the assertion that neutrinos must be moving at the speed of light

and therefore do not have mass. If neutrinos had mass, they would be moving slower than the speed of light and there could be a reference frame – where the observer moves faster than the neutrino – in which the neutrino would actually be left-handed. Because recent observations have indicated neutrinos do in fact have mass, this aspect of the Standard Model is inaccurate.)

#### **2.1.4.1 Spontaneous Symmetry Breaking**

The fact that the three weak bosons are massive, though, comes from applying a process called “spontaneous symmetry breaking.” This method uses the fact that the groups mentioned above have underlying symmetries: that is, they contain parameters that do not affect the physical description of the forces in any way. They are symmetric with respect to variations in these parameters. However, the values of these parameters can be chosen in a strategic way and the result manipulated to give masses to the weak bosons. (A consequence of this “strategic choice” is the appearance of another massive particle in the theory: the Higgs boson. The Higgs boson is therefore predicted by the theoretical mechanism used to account for massive weak bosons. Time – and collision data – will tell if the theory in this form is correct.)

## **2.2 Z Production**

Theoretical treatment of Z production requires a wide variety of tools. The following sections attempt to introduce and explain those concepts, arriving at a discussion of the cross section calculation.

### 2.2.1 Relativistic Kinematics

A particle's coordinates can be described in terms of four quantities: its three spatial coordinates and its point in time. This is conventionally represented as

$$x^\mu = (t, x, y, z)$$

(where we are treating the speed of light to be equal to 1). A particle (or everyday object) can appear to have different properties of motion depending on the reference frame from which it is viewed. If you are sitting on an airplane at cruising altitude, the plane is not moving with respect to your body. However, if you are on the ground, the plane is moving very fast. The physics of the situation cannot depend on the reference frame of the observer, even at the relativistic speeds of interacting particles. There is, however, a certain combination of those time and position coordinates that is invariant – that is, it remains the same no matter the speed or reference frame. This invariant can be constructed as

$$t^2 - x^2 - y^2 - z^2 = x^\mu x_\mu$$

In the same way, a particle's motion can be described in terms of its energy and the three components of its momentum, called “four-momentum:”

$$p^\mu = (E, p_x, p_y, p_z)$$

The invariant combination is called “invariant mass” and is equal to the particle's rest mass. In addition, since the energy and momentum of a system are conserved, the invariant mass is also conserved throughout the entire interaction, in particular the decay. The general definition is given by

$$p^\mu p_\mu = M_{inv}^2 = \left(\sum E\right)^2 - \left\|\sum \mathbf{p}\right\|^2$$

or

$$M_{inv} = \sqrt{\left(\sum E\right)^2 - \left\|\sum \mathbf{p}\right\|^2}$$

For a single particle, the expression simplifies to the particle's mass. This analysis makes use of the fact that the invariant mass of the decay particles (the two electrons) is the same as the (invariant) mass of the particle which decayed, the Z. The above formula, simplified to two particles,

$$M_{inv} = \sqrt{(E_1 + E_2)^2 - \|\mathbf{p}_1 + \mathbf{p}_2\|^2}$$

reconstructs the mass of the Z boson based on the energies and momenta of the decay products.

It is also useful to define variables characterizing the collision itself. The quantity  $s$  is the square of the center-of-momentum energy of the colliding proton system. (Therefore  $\sqrt{s}$  is the center-of-momentum energy itself.) It is obtained by adding together the four-momenta of the colliding protons, designated 1 and 2:

$$s = (p_1 + p_2)^2$$

However, since only a single quark participates in the interaction, not the full proton, the energy of the interaction must be reduced. Since  $x$  is the fraction of the proton's momentum that is carried by the quark (see Section 2.1.3), the quark's momentum is then  $xp$ . We can then define a center-of-momentum energy,  $\hat{s}$  (or  $Q^2$ ), for the quark-quark system, the interacting part of the proton system:

$$\hat{s} = (x_1 p_1 + x_2 p_2)^2 = Q^2$$

( $\hat{s}$  and  $Q^2$  will be used interchangeably.) This can be approximated in terms of the

original (proton)  $s$  as

$$\hat{s} \simeq x_1 x_2 s$$

In a center-of-momentum frame,  $\hat{s}$  is equal to the invariant mass of the quark pair, and therefore the mass of the Z that is produced.

### 2.2.2 Feynman Diagrams

The concept of matrices that transform a particle's state was introduced in Section 2.1.2. Matrices are often used to represent transitions from one quantum mechanical state to another. This can be broadened to the full interaction. Such a matrix acts on the set of initial states and results in the set of final states. Each element in the matrix, mapping an initial state to a final state, gives the amplitude with which the transformation happens. Essentially, squaring the matrix element gives the relative probability of that particular transformation.

A transformation from an initial state, in our case two quarks from colliding protons, to a final state, an electron and a positron, is represented by a Feynman diagram, shown in Figure 2.3. The interaction can be thought to progress to the right. Each straight line represents a fermion, either the quark or the electron. The wavy line represents a boson, the Z. (Gluons are represented by curly lines.) The intersections between particle lines, or vertices, show interactions between the given particles. The matrix element corresponding to this transformation can be written down by attributing factors to the various elements of the Feynman diagram, the particle lines and the vertices. In this way, the diagrams are not just useful conceptual pictures but also powerful calculational tools.

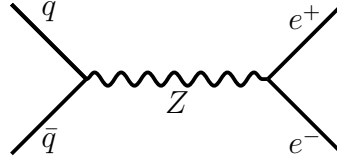


Figure 2.3: Feynman diagram of  $q\bar{q} \rightarrow Z \rightarrow e^+e^-$ .

### 2.2.3 Interference from $q\bar{q} \rightarrow \gamma^* \rightarrow e^+e^-$

In this case, another diagram contributes to the process being studied: a photon replaces the  $Z$  boson as the link between the quarks and the electrons. This is known as the Drell-Yan process. Both cases are illustrated in Figure 2.4. Because these diagrams have the exact same initial and final states, they “interfere” with each other. Experimentally, it is impossible to tell which one happened; both must be included in the calculations.

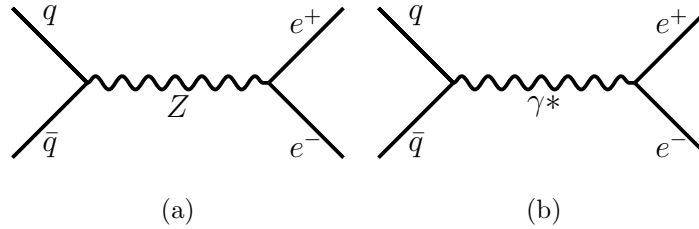


Figure 2.4: Feynman diagrams for  $q\bar{q} \rightarrow Z/\gamma^* \rightarrow e^+e^-$ : the  $Z$  and  $\gamma$  production interfere.

It is necessary to note that the photon that takes part in this interaction is a “virtual” photon – it cannot be directly observed. The reason for this is that there is always a center-of-momentum reference frame for the two particles colliding to form the photon. In other words, there is always some way that you, the observer,

can be moving, such that it looks like the two particles have the same speed but opposite directions. In this reference frame, the photon would be formed at rest, which violates the principle that the speed of light is the same in all reference frames – the speed of light can never be zero. Equivalently, such a photon would have mass, while real photons are massless. The mass of this virtual photon is indeed the same as the invariant mass of the system. Such virtual particles are allowed to exist by the uncertainty principle of quantum mechanics, which governs the “borrowing” of energy from the vacuum. The smaller the time scale over which the energy fluctuation happens, the larger the energy fluctuation allowed.

#### **2.2.4 Mass Distribution**

Having a specific mass defines a thin surface or “shell” in kinematic phase space; only certain combinations of energy and momentum are allowed, because of the relations between mass, energy, and momentum. Particles that are virtual, i.e. have a mass much different than their defined “real” mass, are called “off-shell” – they are “off the mass shell.”

The Z boson, while it has a defined mass, can be “off-shell” in the same way as the virtual photon. That is, in general the mass does not take on a single precise value; instead, over many events it manifests as a distribution peaked around the “real” value. This is typical of particles that are measured only by their decays, called “resonances;” these particles tend to be at least slightly virtual because of their short lifetimes. In addition, the width of the peak is inversely proportional to the lifetime of the particle. The wider the peak, the more final states the particle can decay into, and the more likely it is to decay. The contribution of each final state is called the



“partial width;” this quantity plays a role in calculating how often a given resonance is produced.

### 2.2.5 Higher-Order Diagrams

In real life a given interaction is never represented by just a finite set of diagrams. For each simple diagram, such as Figure 2.3, there is an infinite number of more-complicated diagrams that represent the same initial and final states. A few examples are illustrated in Figure 2.5.

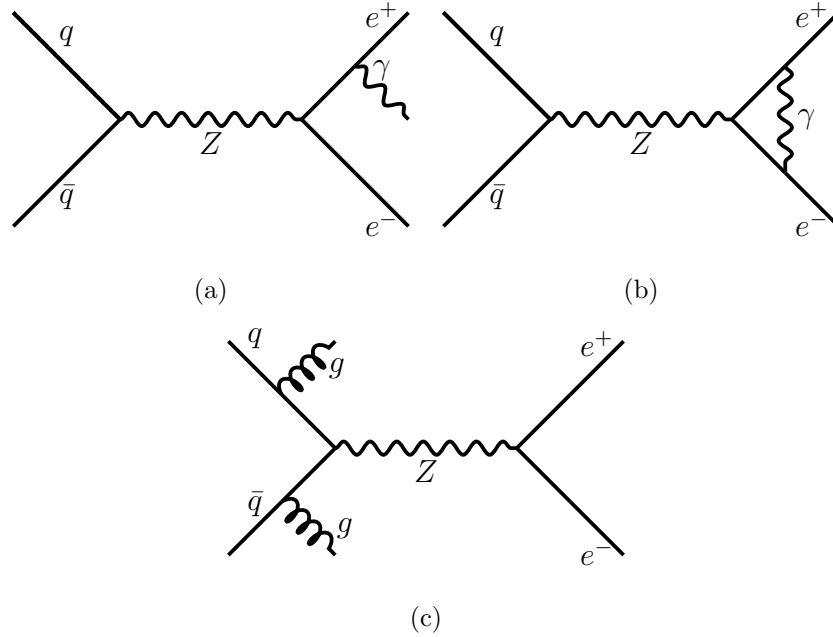


Figure 2.5: Higher-order Feynman diagrams for the process  $q\bar{q} \rightarrow Z \rightarrow e^+e^-$ .

Fortunately, the more complicated a diagram, the smaller its contribution. Each vertex in the diagram contributes one factor of the relevant coupling constant. Since the coupling constants are small, a two-vertex diagram contributes much more than a three-vertex diagram, which contributes more than a four-vertex diagram, etc. How-

ever, the corrections from the higher-vertex (or “higher-order”) diagrams make noticeable contributions to the overall result, and therefore they should be taken into account as far as possible. In mathematical terms, any measurable quantity can be written as a series expansion in terms of the coupling constant  $\alpha$ , as long as  $\alpha$  is small (much less than 1):

$$T(\alpha) = T_0\alpha^0 + T_1\alpha^1 + T_2\alpha^2 + \dots$$

This treats each successively-higher power of  $\alpha$  as a successively-smaller correction to the overall value of the measurable quantity. Therefore, a reasonable approximation of the value can be calculated by using only the first few terms in the series. The “order” of a calculation is given by the highest power of  $\alpha$  taken into account.

Commonly a particle in the initial or final state will radiate a photon or a gluon, creating another vertex in the diagram. These particles will also produce a signature in the detector (the gluon after branching to quarks, which then continue to form a “jet” of hadrons, called “hadronization”). These radiative processes are called “initial-state radiation” (ISR) and “final-state radiation” (FSR). Calculating the contributions from successively higher-order diagrams can be difficult, and many specialized programs exist (see Chapter 4.) The simplest Feynman diagram is called “leading order” (LO), and the successively higher levels, i.e. the higher powers of  $\alpha$  in the series expansion, are “next-to-leading order” (NLO) and “next-to-next-to-leading order” (NNLO). This analysis uses a theoretical cross section calculation that was done at NNLO, which gives a result accurate to around 1%.

### 2.2.6 $Z \rightarrow e^+e^-$ Cross Section

The concept of the cross section was introduced previously, in terms of how to calculate it from experimentally-measured quantities. In principle, though, the cross section can also be calculated from the underlying physics. The cross section element for a transition between two states can be expressed as

$$d\sigma = \frac{|\mathcal{M}|^2}{F} dQ$$

In this formula,  $\mathcal{M}$  is the amplitude (or matrix element) governing the probability of transitioning from the initial state to the final state,  $F$  is the particle flux (total number of initial particles per unit time), and  $dQ$  is the phase space element. An initial state within the phase space element  $dQ$  will contribute the element  $d\sigma$  to the overall interaction cross section. Therefore, to get the full cross section, one must integrate over the full phase space. For an interaction with two initial particles and two final particles (a  $2 \rightarrow 2$  interaction), this can be integrated partially to

$$\left. \frac{d\sigma}{d\Omega} \right|_{CM} = \frac{1}{64\pi^2 s} \frac{p_f}{p_i} |\mathcal{M}|^2$$

where  $p_i$  and  $p_f$  are the momenta of the initial and final particles (in the center-of-momentum frame with two particles, the two particles' momenta have the same magnitude). Here  $d\Omega$  is the solid angle element; the formula cannot be further integrated without knowing the (angular-dependent) form of  $|\mathcal{M}|^2$ .

For any given Feynman diagram, such as Figure 2.3, a set of rules makes it possible to write down the elements of the interaction amplitude,  $|\mathcal{M}|^2$ . Electromagnetic interactions are fairly simple in structure and can be written down (and then calculated out) relatively easily. Electroweak interactions are somewhat more complicated.

The full differential cross section for the interaction  $q_A \bar{q}_B \rightarrow Z \rightarrow e_C e_D^-$  (where  $q_A$  and  $\bar{q}_B$  are the initial quarks and  $e_C$  and  $e_D^-$  are the final electrons) is given by [13]

$$\begin{aligned} \frac{d\sigma}{d\Omega}(q\bar{q} \rightarrow Z \rightarrow e^+e^-) &= \frac{1}{3} \times \frac{1}{256\pi s} \times \frac{s^2}{(s - m_Z^2)^2 + s\Gamma^2} \\ &\times [(L^2 + R^2)(L'^2 + R'^2)(1 + \cos^2 \theta) \\ &\quad + (L^2 - R^2)(L'^2 - R'^2)2\cos \theta] \end{aligned}$$

$\Gamma$  is the  $Z \rightarrow e^+e^-$  decay's partial width (see Section 2.2.4), given by

$$\Gamma(Z \rightarrow e\bar{e}) = \frac{\sqrt{2}G_F m_Z^3}{6\pi} \times [(T_3 - Q_f \sin^2 \theta_W)^2 + (Q_f \sin \theta_W)^2]$$

The  $L$  and  $R$  in the cross section equation refer to factors from left-handed and right-handed initial quarks, respectively (likewise  $L'$  and  $R'$  refer to the final electrons).

These factors are

$$\begin{aligned} L &= \sqrt{\frac{8G_F m_Z^2}{\sqrt{2}}}(T_3 - \sin^2 \theta_W Q) \\ R &= -\sqrt{\frac{8G_F m_Z^2}{\sqrt{2}}}\sin^2 \theta_W Q \end{aligned}$$

$T_3$  is the weak isospin of the left-handed particle (the right-handed particle has isospin 0, hence  $T_3$  does not show up in  $R$ ).  $Q$  is the particle's electric charge. The  $T_3$  and  $Q$  values for the relevant particles are given in Table 2.2.

Since the final-state particles are already known to be electrons, their values can be plugged into the equation. However, the flavor of the initial quarks is not known. Therefore, all the possible initial quark states must be taken into account, by adding up the contribution from each one.

The cross section for the photon process is more easily calculated and is given

Table 2.2: Charge and third component of weak isospin for left-handed Standard Model fermions.

Particle	$Q$ (e)	$T_3$
$u, c, t$	$+\frac{2}{3}$	$+\frac{1}{2}$
$d, s, b$	$-\frac{1}{3}$	$-\frac{1}{2}$
$e, \mu, \tau$	$-1$	$-\frac{1}{2}$
$\nu_e, \nu_\mu, \nu_\tau$	$0$	$+\frac{1}{2}$

by the formula

$$\sigma(q\bar{q} \rightarrow e^+e^-) = \frac{4\pi\alpha^2}{3Q^2} e_q^2$$

However, the cross sections of the Z and the photon processes are not additive; rather, the diagrams interfere, so the full amplitude must be calculated taking both into account at once.

In this case, only the area around the Z peak is being studied, not the full spectrum. The main contribution in this area is the Z itself; however, the photon contribution must still be included in the discussion.

In addition, the interaction does not happen between two quarks in isolation. The cross section calculation must take into account the fact that the quarks come from protons with internal structure. The following formula gives the full cross section in terms of the one given by the quark-level diagram:

$$\begin{aligned} \frac{d\sigma}{dQ^2}(pp \rightarrow Z \rightarrow e^+e^-) &= \left(\frac{1}{3}\right) \left(\frac{1}{3}\right) 3 \sum_q \int dx_1 \int dx_2 f_q(x_1) f_{\bar{q}}(x_2) \\ &\quad \times \frac{d\sigma}{dQ^2}(q\bar{q} \rightarrow Z \rightarrow e^+e^-) \end{aligned}$$

Here  $q$  is the sum over the possible quark flavors and  $f_q(x)$  are the parton distribution functions (see Section 2.1.3) for each quark flavor. Since the Z differential cross section

depends on the PDFs in this way, it is useful as a test of current PDF knowledge. Precision measurements of the differential cross section can distinguish between different implementations of the PDFs.

However, this formula only gives the cross section for the simplest Feynman diagrams; higher-order diagrams contribute as well. As mentioned previously, various programs in existence attempt to include some of these higher-order diagrams in their calculations. More details on the program used for this analysis is available in Section 4.1.2.3.

## 2.3 Results from Previous Experiments

Previous experiments have measured the Z production cross section; however, these experiments have been at electron- positron or proton-antiproton colliders. In addition, they were made using lower collision energies. The LHC marks the first opportunity to study Z production in proton-proton collisions, and at such a high energy.

### 2.3.1 LEP

The Large Electron-Positron Collider (LEP), formerly housed in the LHC tunnel, collided electrons and positrons at a series of center-of-momentum energies. The four associated experiments, OPAL, DELPHI, L3, and ALEPH, performed studies of the Z production when the center-of-momentum energy was scanned across the Z mass, from 88 to 94 GeV (the Z mass being 91 GeV) [14]. Interactions between beams of point particles is different from that of protons in that there are no remnants and hence no leftover energy – aside from initial-state and final-state radiation, all the

energy goes into the interaction. This means that in the case with no ISR or FSR, the invariant mass, the Z mass, is exactly the beams' energy. The beam energy was therefore scanned to measure the Z production at different points along the Z mass spectrum. The data from these measurements was parameterized in terms of a set of fit values to the lineshape. The primary cross section measured was the production of Z decaying to hadrons, which dominates the decay to leptons, at the Z peak ( $\sigma_{had}^0$ ). The value determined for this was consistently around 41.5 nb across the experiments. The ratio of hadronic to leptonic decay rates was also calculated ( $R_l^0$ ), and this was found to be about 20.8. More detailed results are shown in Table 2.3.

Table 2.3: Electron-positron Z production cross sections, measured by LEP experiments.  $\sigma_{had}^0$  is the cross section for hadronic final states, measured at the Z peak.  $R_X^0$  shows the ratio of Z decays into hadrons to decays into lepton flavor X, while  $R_l^0$  gives the averaged result for all leptons.

Experiment	$\sigma_{had}^0$ (pb)	$R_e^0$	$R_\mu^0$	$R_\tau^0$
ALEPH	41.558±0.057	20.690±0.075	20.801±0.056	20.708±0.062
DELPHI	41.578±0.069	20.88±0.12	20.650±0.076	20.84±0.13
L3	41.535±0.054	20.815±0.089	20.861±0.097	20.79±0.13
OPAL	41.501±0.055	20.901±0.084	20.811±0.058	20.832±0.091
Combined	41.541±0.037	20.804±0.050	20.785±0.033	20.764±0.045
		Combined $R_l^0$ value		20.767±0.025

### 2.3.2 Tevatron

The Tevatron at Fermilab collides protons and antiprotons at a center-of-momentum energy of 1.96 TeV. The two general-purpose detectors, CDF and D0, have each produced a Z cross section measurement [15], [16]. CDF measured a cross sec-

tion of  $255 \pm 16$  pb, while D0 measured  $265 \pm 18$  pb. These results are also shown in Table 2.4. However, the Z cross section for proton-antiproton collisions is expected to be higher than that for proton-proton collisions, due to the makeup of the colliding particles. Since a Z can form from a quark and an antiquark, but not two quarks, the chances of a favorable interaction are higher with proton-antiproton pairs. In the proton-proton case, the antiquark must come from the sea (see Section 2.1.3), while both may be valence quarks in proton-antiproton interactions. The exact difference depends on the parton distribution functions, which in turn depend on the interaction energy.

Table 2.4: Proton-antiproton Z production cross sections, measured by Tevatron experiments.

Experiment	$\sigma \times BR(Z \rightarrow ll)$ (pb)
CDF	$254.9 \pm 3.3$ (stat) $\pm 2.6$ (syst) $\pm 15.2$ (lumi)
D0	$264.9 \pm 3.9$ (stat) $\pm 3.5$ (sys) $\pm 17.2$ (lumi)



## Chapter 3

# Experimental Setup

### 3.1 CERN

The European Organization for Nuclear Research, or CERN, is an international laboratory just outside Geneva, Switzerland. It was founded in 1954 as a collaborative effort between twelve European countries. It now has twenty member states, as well as many observer and other non-member states, and is one of the world's major particle physics facilities.

### 3.2 Large Hadron Collider

The Large Hadron Collider (LHC) [17] is a circular particle accelerator near Geneva, Switzerland, with a circumference of 27 km. Two proton beams circulate in opposite directions around the ring and cross at several points, which are home to large particle detectors. Figure 3.1 shows a diagram of the LHC layout. The two general-purpose detectors, CMS and ATLAS, sit on opposite sides of the ring, while the two smaller specialty detectors, LHCb and ALICE, sit at the interaction points to either side of ATLAS. Each beam consists of a series of proton bunches, with a

maximum of 2835 “buckets” in the beam to be filled by bunches. The bunch structure is such that the nominal bunch crossing rate is 40 MHz.

The proton beams are accelerated from injection energy by radio frequency (RF) cavities, which provides an energy boost with each circulation of the beam until the collision energy is achieved. The beams are steered around the ring by 8-Tesla magnetic fields produced in 15-meter-long superconducting niobium-titanium dipole magnets, and focused by quadrupole magnets, 5-7 m long. The LHC uses a design in which both proton beampipes are contained in the same housing, allowing the same liquid helium cooling system to serve both.

The LHC began colliding proton beams in March 2010, quickly reaching its 2010 center-of-mass operating energy of 7 TeV (3.5 TeV per proton beam). At this energy it delivered over  $47 \text{ pb}^{-1}$  of collisions, with a maximum instantaneous luminosity of over  $2 \times 10^{32} \text{ cm}^{-2}\text{s}^{-1}$ . The LHC maximum design energy is 14 TeV (7 TeV per beam), and its design luminosity is  $10^{34} \text{ cm}^{-2}\text{s}^{-1}$ .

### 3.3 Compact Muon Solenoid

The Compact Muon Solenoid (CMS) [18] is one of the two general-purpose experiments for the LHC. Figures 3.2 and 3.3 show the structure of the CMS detector. It is cylindrical, 21.5 m long and with a 15-m diameter, and weighs 12,500 tons. The overall structure of the detector is formed by the iron yoke framework surrounding the inner detector, with the central section, the “barrel,” divided into five ring-shaped slices, while each end of the cylinder, or “endcap,” consists of several circular plates. These sections fit around the solenoid and inner detector, enclosing it completely.

Particle detection is done by several dedicated subdetectors. The electromag-

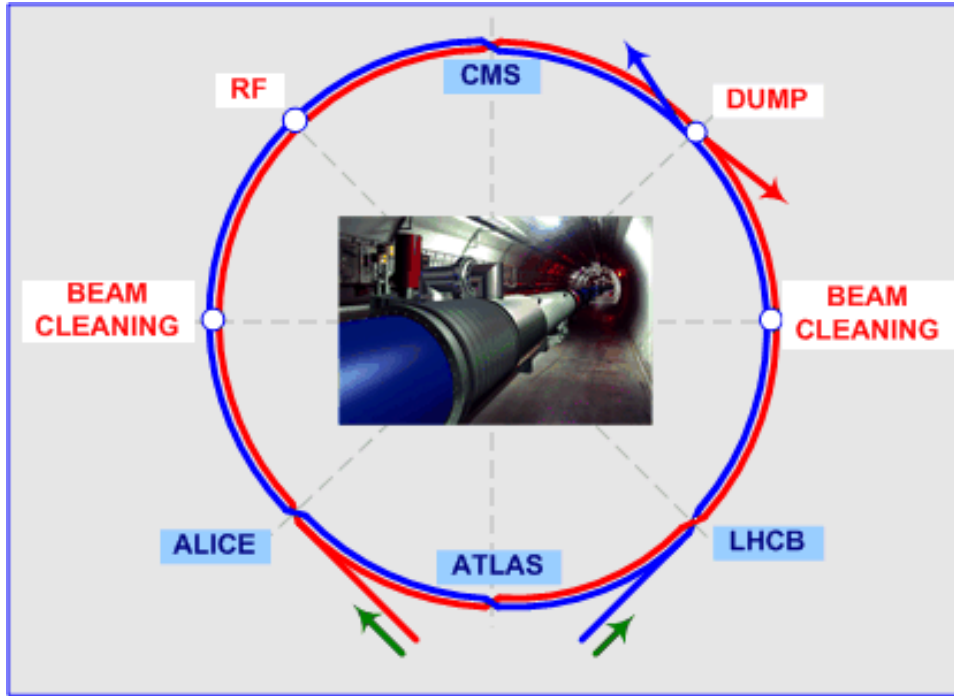


Figure 3.1: Diagram of the LHC layout.

netic and hadronic calorimeters fit inside the solenoid, with the tracking system inside the calorimeters. The three components of the muon system are outside the solenoid, integrated with the iron magnetic field return yoke: the drift tube chambers, resistive plate chambers, and cathode strip chambers.

### 3.3.1 Detection of Particle Interactions

The various parts of the CMS detector work together to differentiate the final particles produced in proton interactions. As these particles traverse their outward trajectory, they pass through the different subdetectors in turn. Figure 3.4 shows how final particles interact with the subsystems of the CMS detector. The innermost subdetector is the tracker, which reconstructs a particle's track through it from a set

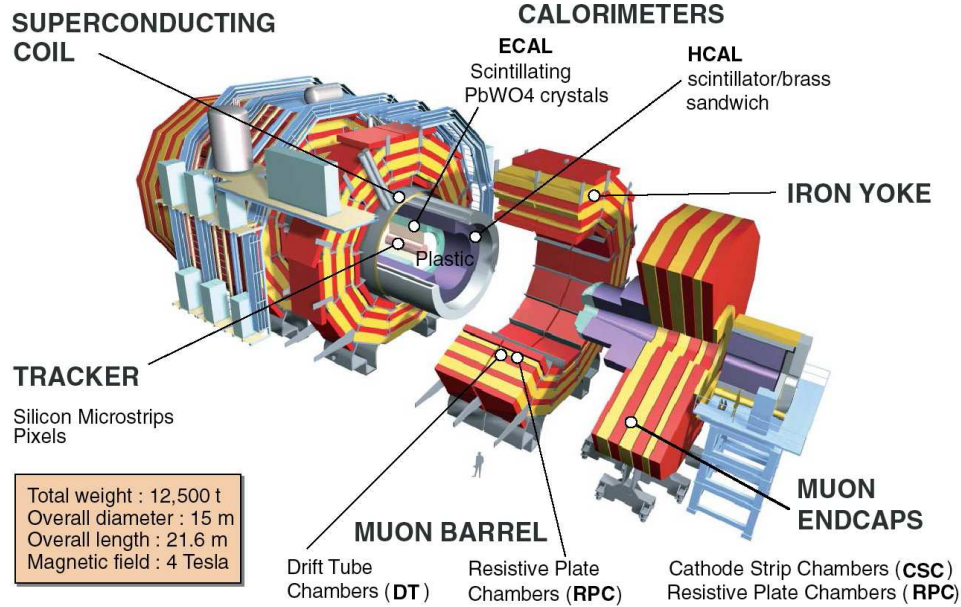


Figure 3.2: Expanded view of the CMS detector, showing the ring and slice structure as well as the placement of each subsystem.

of points where it detected an interaction. The tracker only registers particles with an electric charge; neutral particles pass through undetected. The electromagnetic calorimeter detects particles that interact primarily electromagnetically. In this way the first two “layers” of the detector can differentiate electrons from photons: both are seen in the electromagnetic calorimeter, but only electrons leave traces in the tracker. Outside of the electromagnetic calorimeter is the hadronic calorimeter, which primarily detects hadrons. Hadrons are also detected in the electromagnetic calorimeter, but they leave the largest signature in the hadronic calorimeter, which differentiates the hadrons from the electromagnetic particles like electrons and photons. Hadrons are often found in large quantities called “jets” (see Section 2.2.5), so summing together the energy deposits from sizable electromagnetic and hadronic calorimeter regions

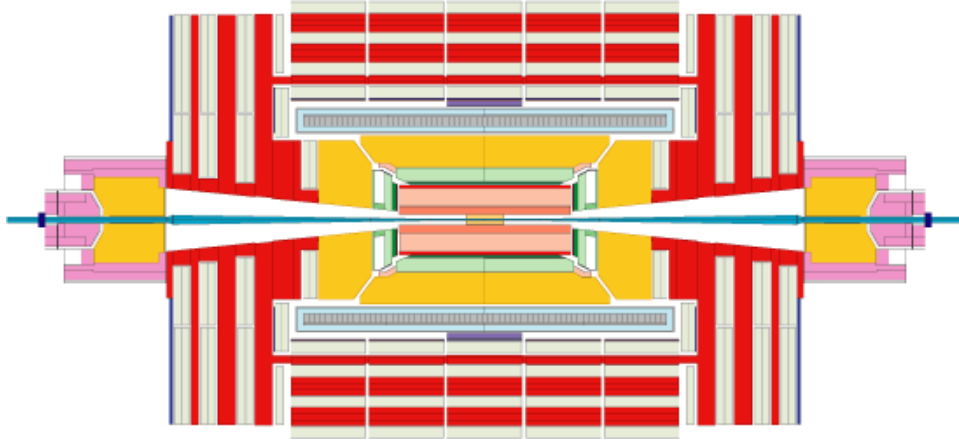


Figure 3.3: Cross-sectional view of the CMS detector.

is important in event reconstruction. Surrounding the tracker and the calorimeters is the solenoid, which generates the magnetic field. The charge of a particle can be determined from which way it bends in the magnetic field. Finally, outside the solenoid and interwoven with the panels of the iron return yoke, is the muon system. Muons leave traces in the inner subdetectors, but they are the only particles to live long enough to reach the muon system. This differentiates them from the other particles detected by the inner subdetectors. Since the muon system is outside the solenoid, the magnetic field points in the opposite direction, and hence the muon trajectories bend in the other direction from their paths inside the solenoid. The last category of final particles, neutrinos, generally cannot be detected. However, their direction and energy in the radial plane can be reconstructed by summing the energy of all the particles in the event. Because the initial protons have zero momentum in the radial plane, and momentum is always conserved, any significant “missing” component to the final energy can be taken as the signature of a neutrino.

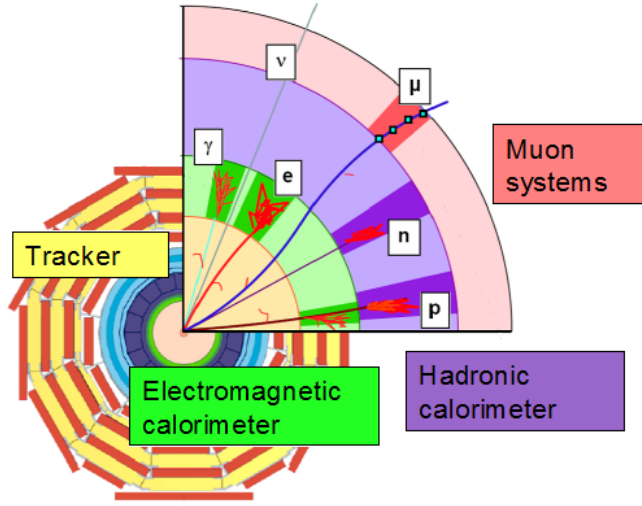


Figure 3.4: Detection of particles in the CMS detector.

A CMS event display from 2010 running can be seen in Figure 3.5.

### 3.3.2 Coordinate System

A standardized set of coordinates is used to describe points and directions within the CMS detector. The origin of the coordinate system is at the interaction point, with the  $x$ -direction pointing horizontally south towards the LHC center (ignoring the slight tilt of the LHC ring with respect to the vertical), and the  $y$ -direction pointing directly upwards. The  $z$ -axis points horizontally west along the beam direction, and the magnetic field inside the solenoid points in the positive  $z$ -direction. The azimuthal angle  $\phi$ , measured in the  $x$ - $y$  plane and ranging from  $-\pi$  to  $+\pi$  radians, is oriented such that  $\phi = 0$  is equivalent to the positive  $x$ -axis and  $\phi = \pi/2$  is equivalent to the positive  $y$ -axis. The longitudinal angle  $\theta$  is measured from the positive  $z$ -axis, and the

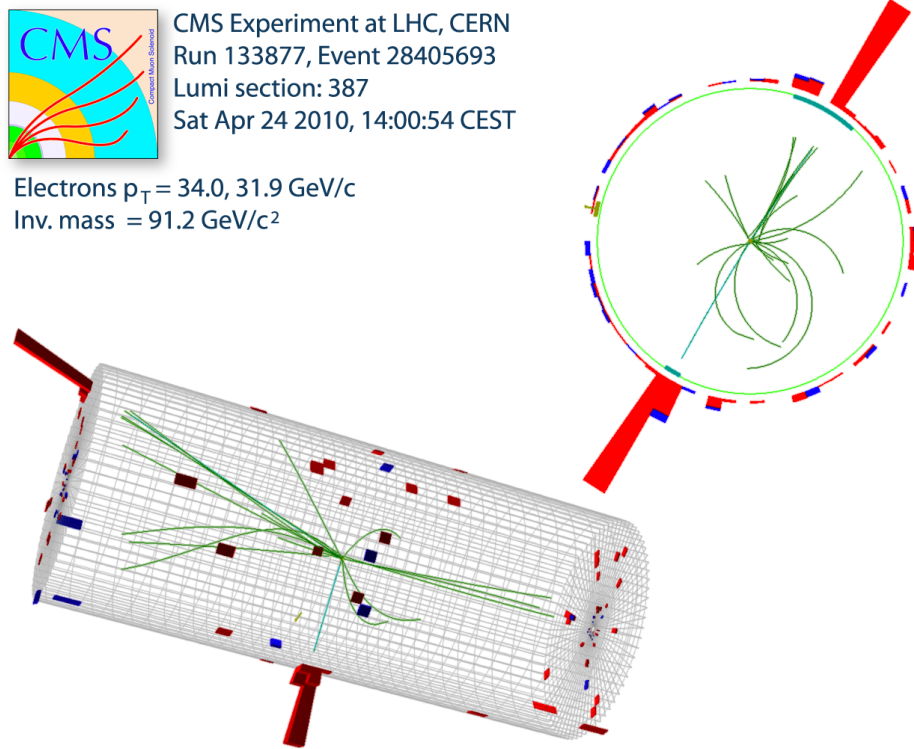


Figure 3.5: Three-dimensional display of a  $Z \rightarrow e^+e^-$  event in the CMS detector.

sign of  $\eta = -\ln \tan(\theta/2)$  is equal to the sign of  $z$ .

### 3.3.3 Magnet

Since charged particles bend in a magnetic field, particle detectors use some sort of magnetic field to determine the charges of decay products. CMS uses a solenoid, or electromagnet in the shape of a coil, to produce a uniform magnetic field in the detector's inner region. The magnet coil is 12.5 m long with a 6 m diameter, and it weighs 220 metric tons. The CMS solenoid is made of a superconducting material, a niobium-titanium alloy, to handle the large amount of current necessary: it generates a field of 4 Tesla using a current of almost 20 kA in a four-layer winding.

The magnetic field is returned through a 10,000 metric ton iron yoke, which also serves as a support structure for the detector. The yoke consists of three concentric cylinders divided into the same 5-ring barrel and 3-disk endcap structure as mentioned previously.

### **3.3.4 Tracker**

The purpose of the tracker is to detect the tracks from final-state particles; only those which are charged can be detected in the tracker. The CMS tracker contains 75 million channels and is specifically designed to get good performance using only a small number of hits per track. It is the innermost layer of the CMS detector and is made up of two different systems: the pixel detector, which is closest to the interaction point and hence has the finer granularity, and the strip tracker, covering the volume out to the calorimeter. Both systems are made of silicon and register charged particles in the same way. When a charged particle passes through the silicon, it knocks electrons out of the material, creating a net positive charge. The electric current needed to return the silicon to its neutral state is measured and amplified by the readout electronics. This readout technology is fast compared to the 25 ns bunch spacing of the LHC. A single track is reconstructed by stringing together the measurements from each of the layers.

#### **3.3.4.1 Pixels**

The silicon pixel detector requires a very fine accuracy due to the high density of tracks near the interaction point. It consists of 65 million readout channels arranged on modules in several layers around the interaction point. In the barrel, the layers are



cylindrical and situated at radii of 4, 7, and 11 cm, while each endcap has two disks, at 6 and 15 cm from the interaction point. Each module consists of a rectangular array of  $100\text{ }\mu\text{m} \times 150\text{ }\mu\text{m}$  pixels, with a resolution of  $15\text{ }\mu\text{m}$ . The pixels on each module are read out by a dedicated chip attached to the module. The chip contains readout unit cells, one corresponding to each pixel, which are connected to the pixels with a small bump of solder in the so-called bump-bonding method.

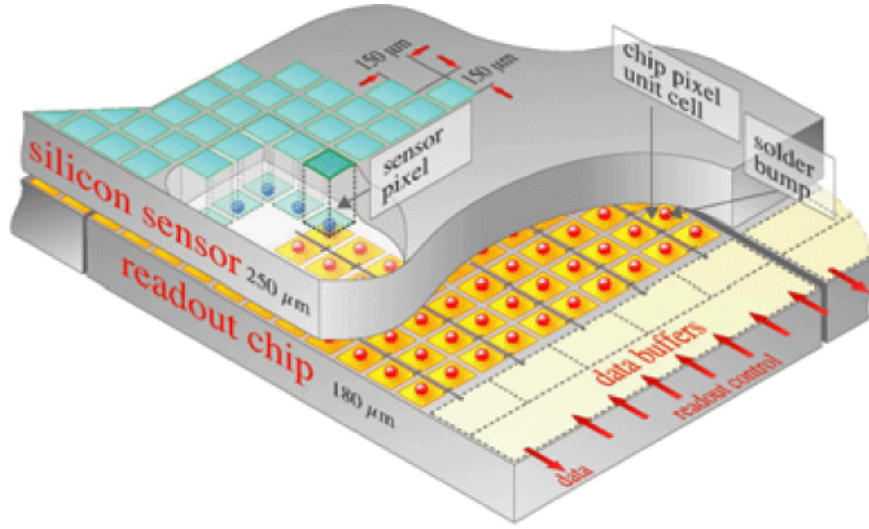


Figure 3.6: Structure of pixel detector layers.

#### 3.3.4.2 Strips

The silicon strip detector consists of 10 million channels arranged in 10 layers of strips, in both the barrel and the endcap, and extends to a radius of 130 cm from the interaction point and to an  $|\eta|$  value of 2.5. The track density at this stage is much less than in the pixel detector, so the granularity does not need to be as fine. Each strip is between about 12 and 16 cm long, with a resolution ranging from  $15\text{ }\mu\text{m}$  in

the inner barrel to  $50\ \mu\text{m}$  in the outer tracker. The strips are arranged in modules of 6 inches in length, with the geometry of each module dependent on its position in the tracker. The strip tracker consists of four different parts: the tracker inner barrel (TIB) with four layers of strips reaching to a radius of 50 cm, the tracker inner endcap disks (TID) with three layers to  $\pm 90\text{ cm}$  in  $z$ , the tracker outer barrel (TOB) with six layers to 1.16 m radially, and the tracker outer endcap (TEC) with nine layers, extending to  $\pm 2.8\text{ m}$  in  $z$ . Several of the layers are double-sided: they contain two sets of silicon modules. The two sets of modules are arranged in a stereo geometry to accurately measure the longitudinal (or radial, in the endcap) coordinate of the hit as well as the azimuthal.

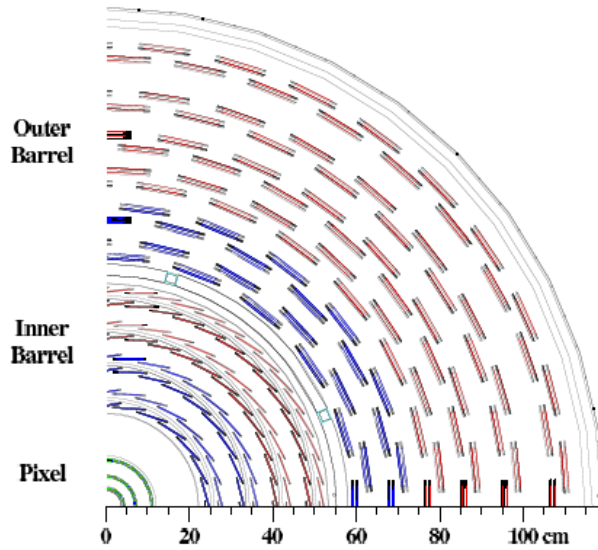


Figure 3.7: Diagram of layers in tracker barrel.

### 3.3.5 Calorimeters

The general purpose of a calorimeter is to measure energy passing through it. CMS measures particles' energies with a scintillating electromagnetic calorimeter (ECAL), situated just outside the tracker, and a sampling hadronic calorimeter (HCAL), surrounding the ECAL. Both calorimeters are contained within the solenoid. This solves a problem seen in other detector designs, in which energy lost in the magnet material leads to an uncertainty in the energy measurement.

#### 3.3.5.1 ECAL

The electromagnetic calorimeter takes advantage of the fact that an electron moving relativistically within a material loses energy by radiating photons, a process known as bremsstrahlung. A photon in the same situation produce an electron-positron pair. Therefore, an electron or photon in the ECAL will produce more electrons and photons, each of which also have a high energy; the bremsstrahlung and pair-production continue in a cascade until the electrons and photons do not have enough energy to create new particles. This cascade is known as an electromagnetic shower. Showers have different spatial extents in different materials; the characteristic lengths are called “radiation length” for the direction of the original particle’s motion, and “Molière radius” for the plane transverse to that motion. The definition of radiation length is the mean distance over which an electron’s energy decreases to  $1/e$  of its original value through bremsstrahlung, so a shower takes place over many radiation lengths. The Molière radius, on the other hand, contains about 90% of the shower energy.

The ECAL is made up of 76,000 lead tungstate crystals, arranged in a cylindrical

barrel and disk-shaped endcap geometry. The barrel is divided into 18 sections in  $\phi$  and two in  $\eta$ , called supermodules. Each endcap is divided into two half-disks, called dees. Each lead tungstate crystal is 2.2 cm x 2.2 cm wide and 23 cm long for the barrel, and 3 cm x 3 cm wide and 22 cm long in the endcap. The dimensions were chosen such that the width of each crystal is approximately the characteristic size of an electromagnetic shower within it (Molière radius of 2.19 cm), and the length is 25 times the radiation length of the material (0.89 cm for lead tungstate). In the barrel, the crystals are oriented with the long axis directed towards the interaction point. However, to avoid particles being lost in the cracks between the crystals, the crystals are offset by 3 degrees in both the  $\phi$  and  $\eta$  directions. An electromagnetically-interacting particle will induce a shower inside the crystals, and the resulting light is captured by photodetectors situated at the back of each crystal. The energy resolution was measured to be

$$\left(\frac{\sigma}{E}\right)^2 = \left(\frac{2.8\%}{\sqrt{E}}\right)^2 + \left(\frac{0.12}{E}\right)^2 + (0.30\%)^2$$

A preshower detector, consisting of lead radiators and silicon sensors, is situated on the face of each endcap. The preshower serves to identify electron pairs due to low-energy pion decays and differentiate them from more interesting signatures. Pions typically decay on the scale of the distance between the interaction point and the ECAL endcap; therefore there is no preshower detector for the barrel, which is too close to the interaction point.

### 3.3.5.2 HCAL

The hadronic calorimeter surrounds the ECAL and covers  $|\eta| < 3$  in the barrel (HB) and endcap (HE) and up to  $|\eta| < 5$  in the forward calorimeter (HF), both within the magnet coil. Additionally, the outer calorimeter (HO) is situated outside the solenoid and serves to detect and measure any leak-through. In general HCAL uses sampling calorimeter technology, with brass and scintillator layers interleaved in the barrel and endcap, and steel plates and quartz fibers for HF; quartz was used in the forward region because of its ability to withstand very high particle fluxes. In a sampling calorimeter, the layers of metal absorber induce particle showers, which are then “sampled” by the layers of scintillator attached to photodetectors. Not all of the energy is directly detected, some being lost in the metal, so the energy measurement is scaled using experimentally-determined factors. The depth of the HCAL in terms of interaction lengths ( $\lambda_I$ , the hadronic equivalent of radiation length) varies between  $5.82 \lambda_I$  at  $\eta = 0$  and  $10.6 \lambda_I$  at the edge of HB and throughout the endcap, with the ECAL adding  $1.1 \lambda_I$ . The HO extends the HCAL depth to at least  $11.8 \lambda_I$  in the barrel, with the magnet material acting as the absorber for the HO scintillator layer. (An additional layer of iron and a second scintillator exist at the  $\eta = 0$  ring, where the HB depth is the least.) Since there is no ECAL in the forward region, the HF is equipped to distinguish electromagnetic objects from hadronic jets with different lengths of quartz fibers. The long fibers reach the entire depth of HF, while the short fibers only start halfway through the detector. Since electromagnetic showers tend to occur in the first half of the detector, and hadronic showers throughout the full HF, a shower detected only by the long fibers is likely to be electromagnetic in nature.

### 3.3.6 Muon System

The CMS muon system serves to identify muons, which are the only particles that leave a signature very far from the interaction point, and also to measure their momentum. The system is situated outside the magnet coil, within the iron return yoke, and provides coverage up to  $|\eta| < 2.4$ . The return yoke also functions as an absorber to filter out backgrounds to the muon signal. The muon system consists of three separate subsystems: drift tube chambers (DTs) in the barrel up to  $|\eta| < 1.2$ , cathode strip chambers (CSCs) in the endcap with an  $\eta$  range  $0.9 < |\eta| < 2.4$ , and resistive plate chambers (RPCs) in the region  $|\eta| < 1.6$ .

The DTs are used in the barrel due to relatively low muon rates in this area, in addition to a uniform magnetic field in the return yoke. Four stations of chambers are interspersed within the iron frame to form concentric cylinders around the beam pipe, with a total of 172,000 detection wires. Orthogonal positioning of the wires within each chamber provides measurement of both azimuthal and longitudinal position. Each wire detects charge that drifts toward it due to an applied voltage when a muon ionizes the surrounding gas, as illustrated in Figure 3.8. Neighboring chambers overlap to ensure full coverage.

The CSCs are used in the endcap, where the muon rate and overall particle flux are higher. Cathode strips in each chamber measure the  $\phi$ -position of a hit, while anode wires oriented perpedicularly measure the  $\eta$ -position. There are on the order of 200,000 readout channels for each type of measurement. Four stations of CSCs are used in each endcap; each muon in the range  $1.2 < |\eta| < 2.4$  crosses either 3 or 4 stations. For  $|\eta|$  between 0.9 and 1.2, muons are detected both by the CSCs in

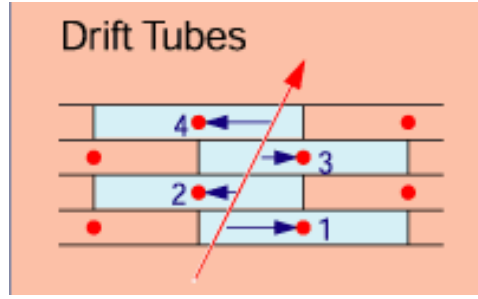


Figure 3.8: Conceptual diagram of drift tube chambers.

the endcap and the DTs in the barrel. Coverage is provided by overlapping layers of chambers at each station.

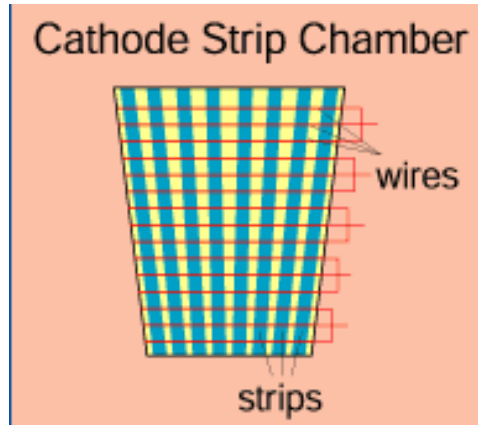


Figure 3.9: Diagram of cathode strip chamber, showing the cathode strips and anode wires for measuring the  $\phi$  and  $\eta$  coordinates, respectively.

The RPCs provide redundancy for the previous two systems as well as a faster response time in place of a highly accurate position measurement. The RPCs measure the timing of a hit with a 1 ns resolution, compared to the 25 ns LHC bunch spacing and hundreds of ns drift time in the drift chambers. Six layers of RPCs are interspersed with the drift tubes in the barrel, while three layers are used in the endcap with the

CSCs. Again, overlapping chambers ensure full coverage. Each chamber consists of two or three double-gap modules, each of which has a single readout module between two thin gas chambers. The readout module consists of metal strips, which capture the electric charge created when a muon ionizes the gas, causing an avalanche of charge. Figure 3.10 shows a diagram of the structure.

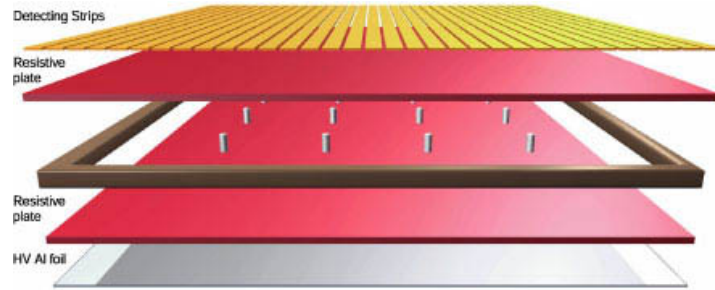


Figure 3.10: Diagram of resistive plate chamber.

Overall, the muon system has a momentum resolution of 9% for relatively moderate- $p_T$ , low- $\eta$  muons, and ranging from 15% to 40% for very-high- $p_T$  muons. When combined with the information from the inner tracker, however, this resolution improves to 1% and 5%, respectively.

### 3.3.7 Trigger

The purpose of the CMS trigger is to identify potentially interesting events. Storing the data from every collision is unfeasible; resources allow only a very small fraction of events to be kept. Therefore the trigger reduces the effective event rate, keeping only the events with an interesting signature, for example a large energy deposit. There are two levels to the CMS trigger. The Level-1 Trigger uses hardware-implemented algorithms to reduce the event rate from the LHC collision frequency of



40 MHz to a maximum of 100 kHz; this must be done quickly since the initial event rate is high. The High-Level Trigger reduces the rate further to about 200 Hz, using a computer farm to process each event in more detail; having a lower input rate, it can afford more processing time per event.

### 3.3.7.1 Level-1 Trigger

The Level-1 trigger (L1) [19] uses mostly programmable, hardware-based algorithms to identify and roughly reconstruct possibly interesting physics objects, such as electrons and muons. This is done within  $3\ \mu\text{s}$ . The structure of the L1 is shown in Figure 3.11. Parallel chains process the muon system and calorimeter objects separately. Tracking information is not included in the L1, which means the L1 algorithms do not distinguish between electrons and photons. The first step of the Level-1 trigger is the generation of coarse versions of the readout information from each of the muon and calorimeter channels; this information is called trigger primitives. The trigger primitives are passed to regional trigger systems, which combine them into trigger objects. The objects for each region are then passed to a global system, which picks out the highest-energy (and therefore most interesting) objects of each type. The final set of objects gets passed on to the last level, the global trigger, which combines information from both the calorimeter and muon chains and makes a single decision based on the set of criteria implemented.

The trigger system must combine all the pieces of information according to the bunch crossing they originate in. This is complicated by the fact that the time it takes particles to reach the outer edge of the muon system is more than that of the bunch crossing interval. In addition, the cable lengths between the subdetectors

and the trigger subsystems and within the trigger are all different, and each of the trigger systems has a different processing time. Despite these challenges, the timing of each piece of the L1 trigger has successfully been tuned to keep everything running synchronously.

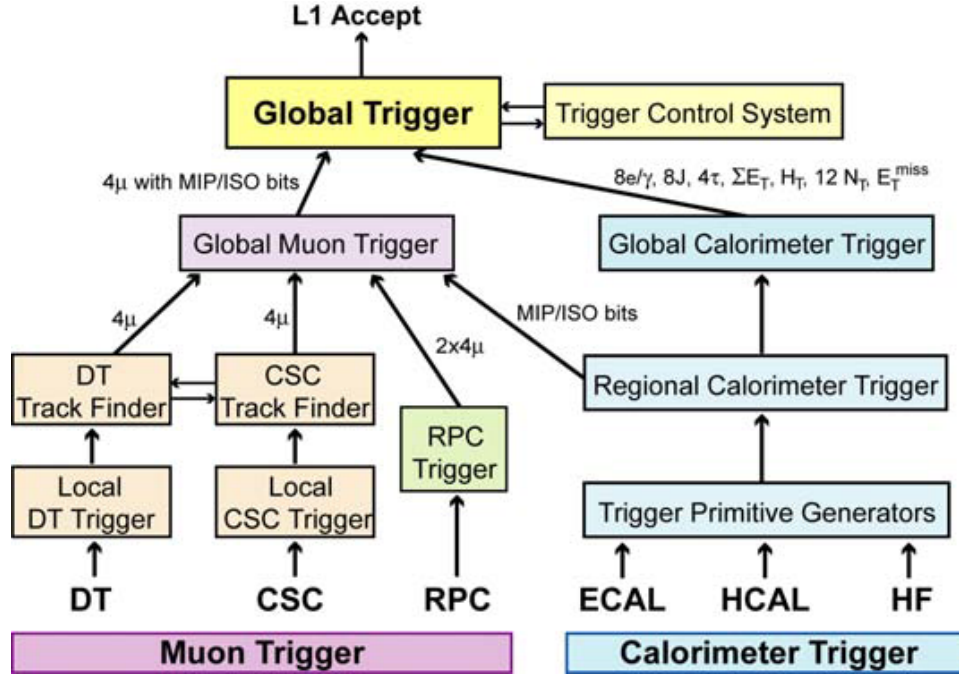


Figure 3.11: Structure of the Level-1 trigger.

### 3.3.7.2 Regional Calorimeter Trigger

The Regional Calorimeter Trigger (RCT) [20] was designed and built and is maintained by the University of Wisconsin at Madison. It sits in eighteen crates in nine racks in the CMS underground electronics room. Each crate deals with one slice of  $\eta$ - $\phi$  space. The general purpose of the RCT is to take energy information from ECAL and HCAL and combine it to generate electron/photon candidates as well as energy

sums for jet-finding. A diagram illustrating the structure of the RCT processing is shown in Figure 3.12.

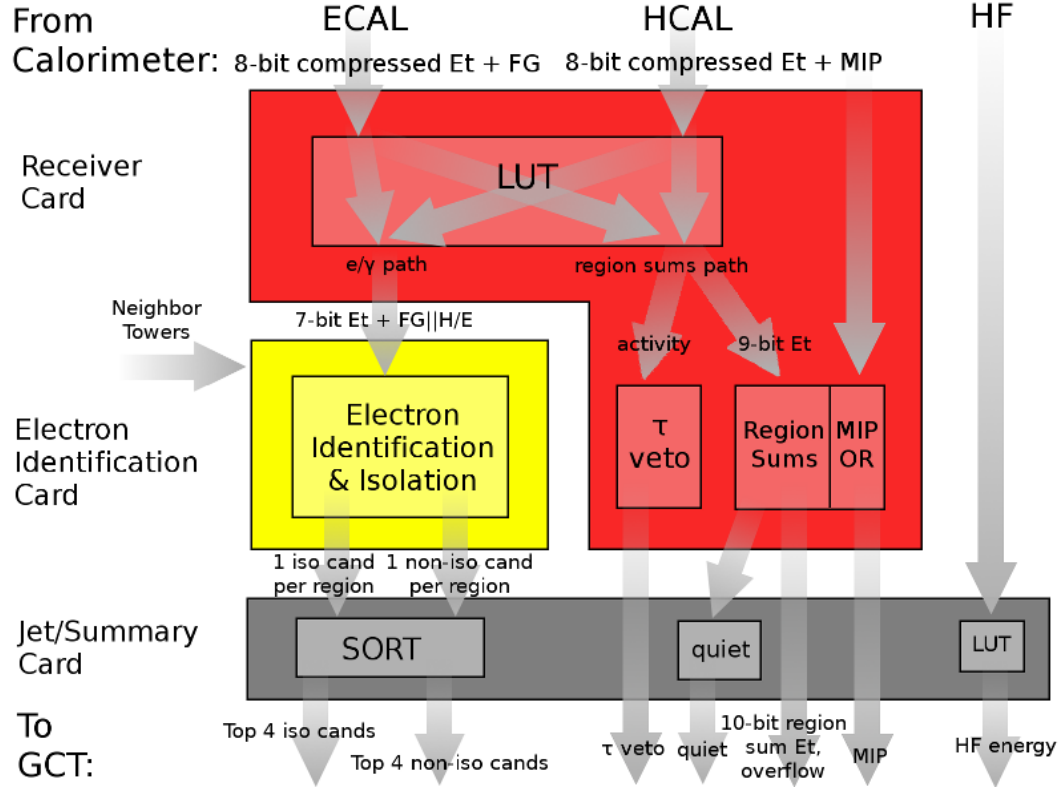


Figure 3.12: Diagram of the RCT structure. The RCT (Regional Calorimeter Trigger) takes energy information at the tower level from the electromagnetic and hadronic calorimeters. It processes this information to produce regional energy sums, electron candidates, and other regional information to be used in the GCT (Global Calorimeter Trigger) processing further downstream.

The information from the calorimeters arrives at the level of trigger towers, a larger granularity than that sent to the full readout. Each ECAL tower corresponds to an HCAL tower behind it. For each ECAL+HCAL tower, the RCT uses memory lookup tables (LUTs) to calculate the total energy sum as well as the ratio of HCAL energy to ECAL energy. If that ratio is higher than a certain value, too much en-

ergy has been deposited in the HCAL tower for it to contain a probable electron or photon. The electron/photon candidates are constructed starting from towers whose energy deposit is higher than any of their four immediate neighbors, as illustrated in Figure 3.13. This primary tower must not have the ECAL fine grain bit set; this fine grain bit indicates a structure in the energy deposit inconsistent with an electron or photon. The tower’s energy is then combined with that of its highest-energy neighbor, to account for particles that deposite energy in more than one tower; this is the energy of the candidate. The candidate is then determined to be either “isolated” or “non-isolated” depending on the character of the deposits in the neighboring towers. If the eight towers forming a square around the primary tower have two full sides (five contiguous towers) with deposits below a configurable threshold (the “quiet” threshold), and these towers’ fine grain bits are not set, then the candidate is isolated. Otherwise, it is non-isolated. Each crate sorts the isolated and non-isolated candidates found according to energy, and the four highest-energy of each type are kept and passed on.

The RCT also calculates the total energy sums of square regions of the calorimeter, 4 trigger towers to a side. The topology of the energy deposits in each region is examined to determine whether or not the deposit is consistent with that from a  $\tau$  particle that has decayed hadronically, i.e. decayed into a jet of hadrons. Only deposits above a configurable threshold are considered. If the deposits in the region make up a single, small, contiguous area as shown in Figure 3.14, then they are consistent with a  $\tau$ . In this case the  $\tau$  veto bit associated with the region is set to false; in all other cases, it is set to true. In addition, the HCAL sends a bit for each HCAL tower indicating whether the energy deposit is consistent with a minimum ionizing

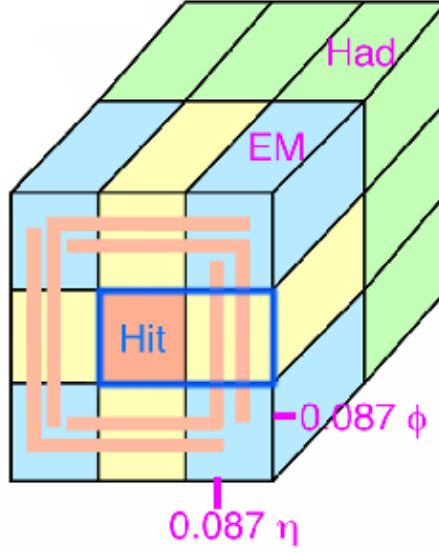


Figure 3.13: Diagram of the RCT electron/photon algorithm. The candidate is defined as a tower whose four immediate neighbor towers have lower energies. The candidate tower’s energy is combined with the energy of its highest-energy neighbor. The candidate is defined as “isolated” if five contiguous towers out of the eight surrounding it (two full sides of the square) have energies below a “quiet” threshold and do not have the fine grain bit set. Otherwise the candidate is “non-isolated.”

particle (MIP), or muon. If any individual tower’s MIP bit is true, then the overall MIP bit associated with the region is also set to true. Otherwise it is set to false. A “quiet” bit is also set to true if any region’s energy is below a configurable threshold.

Finally, the RCT sends the regional energy sums and the list of possible electrons or photons, along with the associated bits (MIP,  $\tau$  veto, quiet), to the Global Calorimeter Trigger (GCT) level. The GCT groups the regional energy sums into jets and collects the four highest-energy isolated and non-isolated electron/photon candidates, and sends this information to the Global Trigger (GT), the last step in the chain. The Global Trigger makes the final decision on whether to accept or reject an

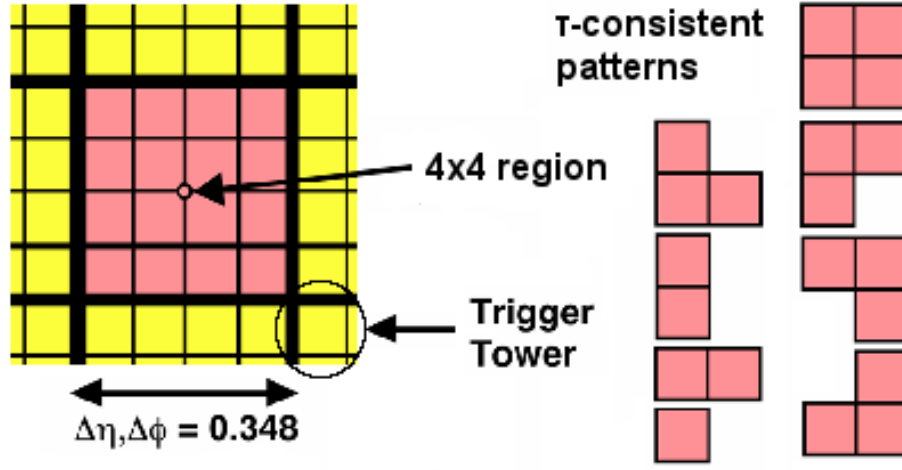


Figure 3.14: Diagram of the RCT  $\tau$  algorithm. The energy deposits in each region are examined to determine whether they are consistent with that from a  $\tau$  that has decayed hadronically. A single small, contiguous region is consistent with a  $\tau$ .

event at the Level-1.

### 3.3.7.3 High-Level Trigger

The High-Level Trigger (HLT) [21] is implemented on a computer farm in the CMS above-ground control room building. It serves to reduce the L1 output event rate from 100 kHz to a rate suitable for transfer and storage to disk, around 200 Hz. An event must pass the HLT to be analyzed offline. The input rate at this stage is lower than that at the Level-1, so more time can be spent on the decision, and more detailed reconstruction can be done. The HLT uses versions of the standard offline physics-object reconstruction algorithms optimized for fast performance. The algorithms need to be more accurate than those of the L1, but absolute accuracy at the offline reconstruction level is not necessary. Still, the HLT algorithms are kept as

close to the offline ones as possible. Specific algorithms are dealt with in more detail in Section 6.1.3.

#### 3.3.7.4 Trigger Menus

Both the L1 and High-Level Triggers use the concept of a trigger menu. There are different sets of criteria defining an “interesting” event at any one time; each set of criteria is called a trigger path. When an event fulfills all the criteria for a given path, that path “fires” and the event is accepted. Some paths may fire at a higher rate than desired, so a prescaling factor is implemented: only a fraction of events firing that path are kept. For example, a path with a prescale of 5 only has 1/5 of its passing events actually saved. In this way, events passing a certain path can still be studied without taking too much of the available resources. The set of paths that are being checked at any given time, along with their prescale factors, is called the trigger menu. The Level-1 and High-Level Triggers each have their own trigger menus. Since the L1 must do things quickly, its criteria are simple, whereas the HLT may have more complex criteria. Passing a given L1 path causes related HLT paths to be run on that event.

At the beginning of collision running, the event rate was low enough to allow very loose trigger menus to be used. At the HLT, a “keep-everything” pass-through menu recorded essentially all activity. As the luminosity increased, however, more stringent criteria had to be applied to maintain an acceptable event rate, for example, raising the amount of energy needed to accept an “interesting” object. The successive algorithms have been studied in detail and commissioned successfully throughout the

2010 running conditions.

### 3.3.8 Luminosity

CMS measures luminosity with the forward calorimeter (HF) [22], which sits between  $|\eta|$  of 3 and 5, close to the beam pipe. Two different methods of measurement are used. The first method counts the number of occupied towers in the HF (above some energy threshold to avoid noise), using the principle that that number is proportional to the luminosity. However, at high luminosity the number of occupied towers may begin to saturate, making this method less accurate. The second method does not saturate in this way: it measures the total energy deposited in the HF, which is also proportional to the luminosity. The information from both of these methods is combined into one luminosity value.

Calibration of the luminosity measurement is done by Van der Meer scans [23], named after their pioneer Simon van der Meer. The luminosity depends on the cross-sectional distribution of the protons in the beam. The distribution functions are taken to be independent in the  $x$  and  $y$  directions, and so can be represented as products of two separate functions,  $f(x, y) = f_x(x)f_y(y)$ . The Van der Meer scans measure these distributions by changing the beams' relative position in small steps, in both the  $x$  and  $y$  directions. The interaction rate at each measurement step is recorded using the CMS detector, and the data points are fit using the sum of two Gaussian distributions: one for the core peak, and one to model the tails of the distribution. The beam-shape parameters used in the calibration are extracted from these fits. The calibration calculation also factors in the orbit frequency and number of colliding bunches, as well as the beam intensities, which are measured using Fast Beam Current



Transformers [24].

Figure 3.15 shows the total integrated luminosity at CMS as a function of time for the 2010 running period [25]. The amount of data validated for physics analysis was  $36.1 \text{ pb}^{-1}$ .

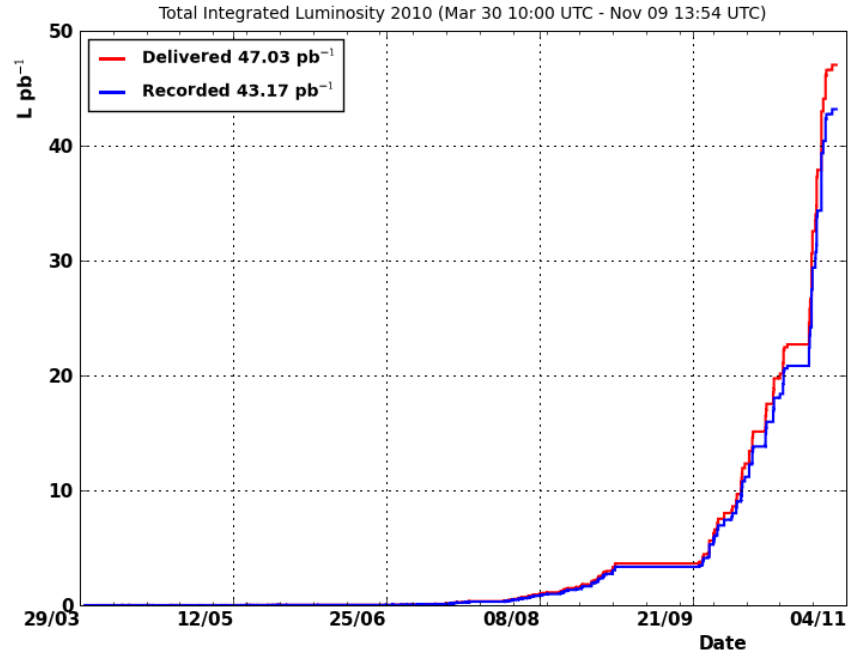


Figure 3.15: Luminosity collected by CMS as a function of time, 2010.

## Chapter 4

### Event Simulation

Within a high-energy physics experiment's role of making discoveries and measurements, it is necessary to know ahead of time what exactly should be expected. What will the detector signature of a new process look like? How will we know whether we've seen something unexpected? This is where event simulation contributes. Essentially, a series of programs is used to carefully generate and calculate all the relevant quantities for a set of fake events. This information is then used to aid analysis in ways for which real data alone cannot suffice.

Having the ability to simulate physics processes serves multiple purposes. It aids in detector design: knowing the expected typical characteristics of particle interactions is essential to design a detector suited for those interactions. Once the detector design is settled, simulation of the detector is useful to design the algorithms used to reconstruct particles from their signature interactions with the detector material. In addition, simulating the physics processes can give estimates of how many events of a particular type are expected, further aiding the design process. The event simulation also contributes directly to many analyses, in the way of calculating the acceptance, the fraction of events that can theoretically be detected (see Section 1.5): it is impos-

sible to know from observation how many events are missed by the detector, because of the very fact that they are unseen. It is instead necessary to get that fraction from a framework in which the characteristics of all events are inherently known, not reconstructed. Finally, simulated data is directly compared with “real” data from the detector to interpret the real-data results. If the data shows something significantly different from the simulation, then something is missing: perhaps a calibration needs to be applied, or the response of a detector unit needs to be further understood. Or, perhaps, there is a new physics process appearing for the first time, which was not previously known and which was therefore not present in the simulation. In this case simulation of proposed new physics processes may narrow down the identity of the observed new process. Whatever the case, discrepancy between observed data and the event simulation indicates that further investigation is necessary.

The entire detection process is simulated, including the protons’ direct interaction and any subsequent particle decays, as well as how the end-product particles interact with the detector as they pass through and how the detector itself responds. This latter part includes not only the material of the individual subdetectors but also the algorithms of the Level-1 Trigger, which are implemented in hardware (see Section 3.3.7.1). The High-Level Trigger does not need to be simulated in this way; since its algorithms are all software-based, the same code can be run without modification on both real data and simulated data.

## 4.1 Monte Carlo Event Generation

“Event generation” refers to creating a set of simulated physics events, usually realistic, for purposes of study and comparison with real data. The term “Monte

Carlo” is connected with this process because at the most fundamental level it is based on random numbers. All physics interactions happen in terms of probabilities: process X is more likely to happen than process Y, so process X is observed more often. For any given fake event, which physics process is actually simulated is randomly determined according to those probabilities. The kinematics of the event (energies and directions of involved particles) are also assigned according to probabilities. The final result is that having enough events will reproduce the original probabilities of each interaction. (It is worth noting that in terms of software, nothing is really random; in general, programs to create “random numbers” are really only pseudorandom, because computers by nature do things according to programmed rules. However, for the purpose of event generation, pseudorandom numbers are suitable if they are sufficiently random-like. Moreover, using a deterministic pseudorandom generation algorithm aids in debugging – the results of the algorithm are reproducible, which cannot happen with truly random numbers.)

#### 4.1.1 Types of Monte Carlo Simulation Programs<sup>1</sup>

There are two sorts of programs that can be called “Monte Carlo event simulators.” They both use the matrix elements derived from the Feynman diagrams of the physics interactions of interest (explained in Section 2.2.2), but they use the matrix element formalism in different ways to achieve different ends. As a reminder, the equation to obtain the differential cross section element from the matrix element for a given diagram is

---

<sup>1</sup>Material in this section was taken from [26].

$$d\sigma = \frac{1}{64\pi^2 s} \frac{p_f}{p_i} |\mathcal{M}|^2 d\Omega$$

The first type of Monte Carlo program outputs a single quantity or set of quantities characteristic of the given process, such as the cross section. These programs are called “cross section integrators.” They calculate  $d\sigma$  for each of a uniform distribution of phase space values (i.e. uniform increments of  $\cos\theta$  and  $\phi$ ). The value of  $d\sigma$  represents each event’s “weight”; the total cross section  $\sigma$  is then obtained by integrating over the full collection of  $d\sigma$  values. The final result is a value for the cross section; hence the name “cross section integrator.” However, since the events themselves are distributed uniformly in  $\cos\theta$  and  $\phi$ , their characteristics do not represent actual event distributions (real event distributions in data have non-uniform distributions, in  $\cos\theta$  in particular). Therefore they can only be used to calculate a few select quantities; they can’t be used to predict distributions.

The second set of programs are called “event generators.” They also use the matrix element to calculate the differential cross section element with the equation given above. However, instead of using  $d\sigma$  as an event weight, they “unweight” the events to obtain the physical distributions. They do this through the so-called acceptance-rejection method: first the maximum possible value of  $d\sigma$  is calculated,  $d\sigma_{max}$ . Each event’s individual  $d\sigma$  value, the ratio  $\frac{d\sigma}{d\sigma_{max}}$  is taken; this number is necessarily a fraction between 0 and 1. A random number  $g$  between 0 and 1 is then generated. If the ratio  $\frac{d\sigma}{d\sigma_{max}}$  is greater than  $g$ , then the event is kept; otherwise, it is rejected. This method causes the generated events to have the properties and distributions that real events would have – sections of phase space with a higher “event weight” are more

likely to be represented.

However, using a single Feynman diagram is not typically sufficient to make very accurate calculations. In general, there are significant contributions from the higher-order diagrams (diagrams with more legs and loops, but still representing the same final arrangement of particles; see Section 2.2.5 for more detail on higher-order diagrams and calculations). These corrections must be taken into account. Corrections from both QED (photons and electrons) and QCD (quarks and gluons) affect the outcome. However, due to the strength of the strong force (i.e. the high value of the QCD coupling constant), QCD has the greater effect and therefore drives the development of calculation methods, although some of the same methods can also be applied to QED. There are two complementary approaches commonly in use to deal with the corrections. In the first, the “matrix element” method, higher-order diagrams are explicitly included in the matrix element calculation. Since the higher the order, the more complex the calculation, only diagrams of up to a given order are generally used. Two approaches exist: in one implementation, more “legs” can be dealt with, but diagrams containing virtual loops are ignored. In the other, all diagrams, including those with virtual loops, of a single order are used, but at the moment there exist satisfactory solutions only for next-to-leading-order diagrams (or NLO, explained in Section 2.2.5). In the second of the two approaches, the “parton shower” method, the particles involved in the basic tree-level interaction are made to radiate according to probabilities and rules coded into the program. The process is iterative, repeating for any quarks or gluons that branch off at any point. The matrix element and parton shower methods can be used as complements; in particular, the

parton shower method can take output from the matrix element method and apply the radiation process.

The philosophy of parton-shower generators in particular is that the entire process of simulating a physics event can be done in a modular fashion. Figure 4.1 shows the typical steps necessary to simulate an event. The incoming protons are modeled in terms of the parton distribution functions (Section 2.1.3). The “hard subprocess” refers to the main physics interaction. Not shown in the diagram are other interactions involving different parts of the protons or other protons in the same bunch, the “underlying event” (see Section 1.4). The participant particles in the main interaction are then “evolved” through the showering process, which includes emissions of photons or gluons by the initial- or final-state particles, as well as “branchings” of final particles. Any resulting quarks and gluons are formed into “colorless” hadrons, which may then decay into other particles. These final particles are the ones seen in the detector. The fact that the full process can be separated into these steps makes it easier for different programs to handle individual steps. For example, one program may simulate the hard process, while another is better-equipped to take care of the showering and hadronization, and a third is specialized in the decay of a particular particle. Taking the theme of modularity even further, the set of fully-decayed particles is then plugged into a program simulating the passage of the particles through the detector and the detector’s response (Section 4.2).

The process of hadronization is not directly relevant to this analysis, since the analysis does not require hadrons to exist in the final state. However, since initial- or final-state radiation may cause jets incidental to the main interaction that nevertheless

affect its kinematics, hadronization is included here. In addition, for radiation due to QED, electrons and photons in the final state can be treated as “partons,” in the same category as the quarks and gluons, to simplify the description. Even though they are not constituents of the proton, they can be modeled as having “distribution functions” and subject to “showers” of photons and electrons. This lets these two very different processes be plugged into the same parton shower machinery and treated the same way.

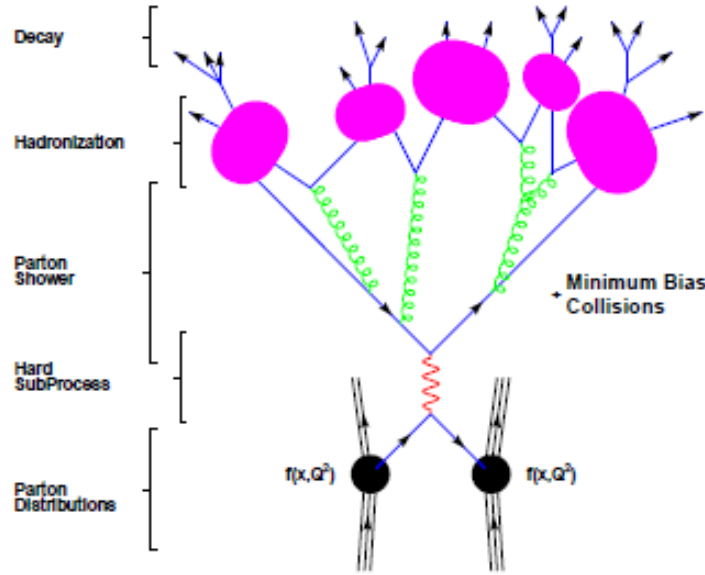


Figure 4.1: Diagram of typical steps used to simulate event in parton shower method. The incoming protons are modeled in terms of the parton distribution functions. The “hard subprocess” refers to the main physics interaction.

#### 4.1.2 Monte Carlo Generator Programs

Several Monte Carlo programs were used to fulfill different roles in this analysis. Two programs were used to generate the simulation events used: one general-purpose



generator for background events, and a more specialized generator for the signal sample. A few of the background samples used a dedicated decay program to decay specific particles in the end state. Finally, a cross section integrator was used to obtain a highly precise estimate of the theoretical value of the interaction cross section. These programs will be detailed in the following sections.

#### 4.1.2.1 PYTHIA

CMS makes use of one of the standard Monte Carlo event generation workhorses, a program known as PYTHIA (v6.4) [27]. PYTHIA was used to generate the background samples used in this analysis, with the CTEQ6L1 PDF set [12]. PYTHIA is a general-purpose event generator using the parton-shower approach to corrections. It encompasses most of the steps necessary to generate an event: the parton distribution functions that describe the colliding protons, the main physics interaction process, the non-interacting remnants (underlying event), and how the end products shower, hadronize, and decay. Over its long history PYTHIA has built up a large collection of tools, which include many main physics processes and various methods of dealing with each of the steps mentioned above. PYTHIA also includes many non-standard-model physics processes in order to study new physics theories. Most of what it does can be adjusted by the user via changing parameters; however, its default values are chosen to produce valid output without the need to necessarily adjust settings. Because PYTHIA is such a wide-ranging program, it does not treat everything it handles in depth. For this reason, specialized programs are sometimes used to work with specific areas of the simulation process, including the ones in the following sections.

This analysis does not directly deal with quarks or jets; however, since jets can

be present in the final state and can play a role in the kinematics of the  $pp \rightarrow Z$  interaction, the method of dealing with hadronization is relevant here. PYTHIA by default uses the Lund string model [28] (illustrated in Figure 4.2) to evolve quarks and gluons through the process of hadronization and formation into jets. Conceptually, an interaction’s final state may have quarks “flying off in different directions.” However, quarks cannot exist alone: they must always exist with other quarks, held together by the strong force. If the individual quarks do not have very much energy as they move apart, the increasing energy of their interaction will hold them together. However, if the quarks have much energy, the interaction energy will not be enough to hold them together, and they will need to form new “quark partners” in order to remain in a bound state with other quarks. According to the Lund string model, the energy between opposite color charges increases approximately linearly with distance. The energy is concentrated into a linear area, like a tube or string. These strings are always stretched between two quarks. Enough energy on the part of the quarks will “break” the string and create a new quark-antiquark pair, which then fills the need for “quark partners,” as illustrated in Fig 4.2b. The process continues until the quarks do not have enough energy to overcome the force holding them together.

The underlying event can be represented in PYTHIA by different configurations of parameters, known as “tunes.” The tunes have been chosen to correctly model already-existing distributions from previous experiments. This analysis uses samples generated according to the default tune used in CMS, Tune Z2 [29]. However, differences between the tunes are very slight and affect final results very little; these effects are accounted for in the systematic errors (Section 7.2.4).

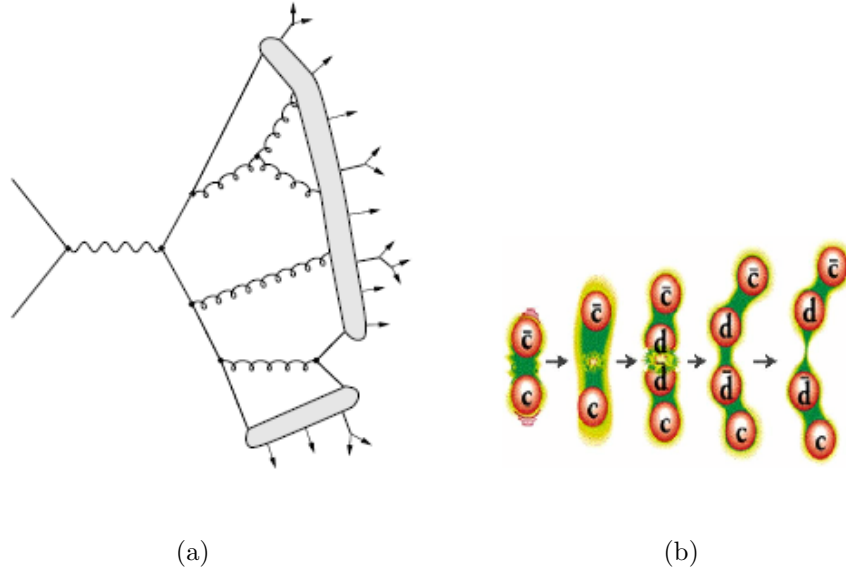


Figure 4.2: Schematics showing the Lund string model of hadronization. (a) In the Lund string model, the quarks are joined by strings which “break” to form new quark-antiquark pairs. The process continues until the quarks’ energies are not enough to overcome the force holding them together. The gray areas represent chains of quarks joined by such strings. (b) An illustration of a possible creation of a quark-antiquark pair.

#### 4.1.2.2 POWHEG

POWHEG (for “POsitive Weight Hardest Emission Generator”) [30] is a method for making next-to-leading order (NLO) corrections within a parton shower framework. At low energies, the showering algorithms implemented in parton shower generators (such as PYTHIA) model the corrections well. However, at higher energies, a next-to-leading order matrix calculation is more accurate. An ideal solution combines the two approaches to get the best of each. Since POWHEG does this, it therefore produces a more accurate picture of the radiation corrections and their effects on final-state kinematic quantities when compared to a standard parton-shower generator, which

only includes some (the real part) of these corrections. POWHEG consists of a number of routines representing various interactions, including  $Z \rightarrow e^+e^-$ . Processes that are not already included in the set may be implemented by the user.

POWHEG was used to generate the hard process for each event of the  $Z \rightarrow e^+e^-$  signal sample, using the CT10 PDF set [10]; this part of the interaction was then fed through PYTHIA (by the modular procedure previously described) to undergo hadronization. It was more important for the signal sample to be accurate to higher order than for the background samples; the background samples are only of interest in terms of how much they may contaminate the signal sample. Slight variations in their distributions due to missing higher-order corrections are therefore not as relevant.

#### 4.1.2.3 Other Generators

Two other Monte Carlo event generators played roles in the analysis. In the first case, particles in some of the background samples called for a specialized decay package. In the second, a precise theoretical prediction was needed to compare with data, and the standard programs used to generate the events cannot reach the necessary precision.

Many particle decays are handled by the primary event generator, PYTHIA. However, there are several aspects of decays that PYTHIA does not deal with, such as spin polarization. Because these aspects can have small effects on the kinematic distributions of the decayed particles, CMS decided to use a separate package, TAUOLA [31], to decay  $\tau$  particles in the samples that included at least one  $\tau$  per event. TAUOLA specifically takes spin polarization into account, and includes first order QED corrections. The TAUOLA package was only necessary for the  $Z/\gamma^* \rightarrow \tau^+\tau^-$

and  $W \rightarrow \tau\nu$  background samples.

The theoretical prediction for the cross section value was obtained with FEWZ [32], a cross section integration program specifically dealing with production of the W and Z, using the MSTW PDF set [11]. Previously, all calculations of the cross section had been done at next-to-leading order (NLO) in QCD, which entails several percent uncertainty. However, since the statistical error on W and Z results at the LHC was quickly expected to reach the order of 1%, it was deemed necessary to undertake a calculation at next-to-next-to-leading order (NNLO), which gives a theoretical uncertainty of approximately the same value. (In essence, all higher-order corrections beyond NNLO contribute about a percent or less of uncertainty.) FEWZ was chosen to calculate the cross sections for the CMS analysis because of this treatment of NNLO QCD corrections.

#### 4.1.3 Generated Samples

The full list of Monte Carlo generated samples used for this analysis is given in Table 4.1. The first line is signal; the rest are background.

The table also gives the values by which each of the samples were scaled in order to be combined. Each sample was generated to be a specific size, that is, a specific number of events. These sizes do not correlate to the same amount of real data, though. The sample for a common process may correspond to a relatively small amount of data, while that for a rare process may be equivalent to a very large amount of data; i.e. because of its rarity, a large amount of data is required in order to see it. These differences are taken into account by determining a scale factor for each sample according to its size and its cross section (which correlates to probability of

Table 4.1: Monte Carlo samples used in this analysis. The first line is signal; the rest are background. The scale factor is calculated with  $36.1 \text{ pb}^{-1}$  .

Sample	Generator	$n_{events}$	$\sigma$ (pb)	$\epsilon$	Scale factor
$Z \rightarrow e^+e^-$	POWHEG	1998990	1666.	1.	$3.01 \times 10^{-2}$
QCD BCtoE 20-30	PYTHIA	2243439	235500000.	0.00056	2.12
QCD BCtoE 30-80	PYTHIA	1995502	59300000.	0.00230	2.47
QCD BCtoE 80-170	PYTHIA	1043390	906000.	0.0104	0.326
QCD EM 20-30	PYTHIA	36920242	235500000.	0.0104	2.39
QCD EM 30-80	PYTHIA	71834019	59300000.	0.065	1.94
QCD EM 80-170	PYTHIA	8073559	906000.	0.155	0.628
$t\bar{t}$	PYTHIA	1099550	94.3	1.	$3.10 \times 10^{-3}$
$Z/\gamma^* \rightarrow \tau^+\tau^-$	PYTHIA	2057446	1666.	1.	$2.92 \times 10^{-2}$
$W \rightarrow e\nu$	PYTHIA	4856474	6153.	1.	$4.57 \times 10^{-2}$
$W \rightarrow \tau\nu$	PYTHIA	5207750	7899.	1.	$5.48 \times 10^{-2}$
WW	PYTHIA	110000	2.9	1.	$9.52 \times 10^{-4}$
WZ	PYTHIA	110000	0.34	1.	$1.12 \times 10^{-4}$
ZZ	PYTHIA	2113368	4.297	1.	$7.34 \times 10^{-5}$

the interaction). This scale factor is used to scale each sample to a given luminosity. The scale factor must also take into account any inefficiency in the generation process. For example, if the sample was generated such that at least one electron had an energy higher than 10 GeV, all the events whose highest-energy electron was lower than 10 GeV will be discarded. They still count towards the overall cross section, though, so they are taken into account by an efficiency number, essentially the fraction of events that are kept in the filtering process. The formula for the scale factor  $k$  is

$$k = \frac{\mathcal{L} \times \sigma \times \epsilon_{filter}}{n_{events}}$$

After multiplying each sample by its scale factor, samples and event numbers can be added together.

The QCD samples are broken into smaller sections for easier generation: three bins were used, given in terms of the interaction energy. They are also the only samples here to need an efficiency factor. Since much of what is produced by QCD will get cut out by the event selection requirements, it is useful to pare down the samples from the start, so they do not take up unnecessary space. The QCD samples have filters applied to select only events which could be background to an analysis using electrons and photons. The “BCtoE” samples include events with electrons from the decays of bound states of  $b$  and  $c$  quarks. The “EM” samples are “electromagnetic-enriched,” meaning the generation process applied a filter to include electrons and photons, as well as objects that look like electrons and photons. This second group also requires that each event not pass the BCtoE filter, so that the two samples are mutually exclusive and can be combined without double-counting.

## 4.2 Detector Simulation

After the generation of the main physics process, parton showering, hadronization, and decays, the role of the detector itself must be taken into account. The final-state particles interact with the detector, which causes signals representing the particle’s position and energy to be recorded as data. These must be properly modeled to know, for example, what sort of signal would result from the passage of a particle with a given momentum. In addition, the detector itself is not completely passive, in that it can change the properties of the particles passing through it during the course of measurement. Both of these roles necessitate a detailed simulation of the detector and its response.

### 4.2.1 GEANT Detector Model

The CMS collaboration uses the software package GEANT4 (v9.3) [33] to model the detector within the framework of CMSSW, the CMS-specific analysis software (see Section 1.7.1). GEANT4 provides a toolkit designed to accurately represent all facets of the detector simulation. These include the ability to construct a precise geometrical model of the detector itself, complete with any actual misalignments and a model of the detector’s magnetic field, as well as the physical properties of the materials used. In addition, the package also handles the properties of the fundamental particles involved, how they behave in the modeled magnetic field, and how they interact with the different materials present in the detector. For example, the detection of particles in the electromagnetic calorimeter depends on those particles causing a shower of other particles upon interacting with the calorimeter material; this must be modeled. Finally, GEANT4 also provides the ability to model the response of the electronics



used to detect the particles, for example the response of a photomultiplier tube to a light signal caused by the aforementioned shower.

#### **4.2.2 Level-1 Trigger Emulator**

In addition to modeling the detector components that do the actual detecting, it is necessary to include the response of the trigger system (Section 3.3.7), which serves multiple purposes. Modeling the trigger system enables the estimation of event rates for a given luminosity before the experiment actually runs with that luminosity. In particular, this has permitted the estimation of rates long before the detector was fully constructed, greatly aiding the experiment’s physics planning. In addition, comparison of the real-time “online” performance of the trigger with its software counterpart can indicate and aid in diagnosing problems with the online running.

The High-Level part of the trigger system (HLT), consisting of algorithms implemented in software, is simply run “offline” as an element of the detector simulation. However, the Level-1 Trigger (L1), being implemented in electronics instead of software, must be explicitly modeled. The software package that does this is called the Level-1 Trigger Emulator [34], since it aims to be a bit-by-bit emulation of the trigger hardware instead of just a simulation of the algorithms implemented. The L1 Emulator is modular in the same sense as the hardware system; information is passed between separate packages representing the different subsystems of the L1. Each element of the hardware, namely each type of processing card, has its own software class to handle its own specific functions. The software therefore aims to model each of the trigger’s processing steps in accurate detail, so that the overall result is identical.

## Chapter 5

# Event Reconstruction

The information from the detector for any given event gets read out over millions of channels from the many different subdetectors. These signals must be combined to provide meaningful physics information about the interaction that took place within the detector, namely the measurable quantities (like direction and energy) of the outgoing decay products.

### 5.1 Detector Object Reconstruction

The first step of the particle reconstruction involves translating the information from each detector channel, such as position and electronics signal, into useful quantities such as position in  $\eta$ - $\phi$  space and energy or momentum. This is done by algorithms mapping each individual detector cell to its  $\eta$ - $\phi$  placement and calculating its energy, which necessarily takes into account the position of each cell. The second step involves connecting information from different channels to build up a more complex picture of the particles that passed through the detector.

### 5.1.1 Electromagnetic Calorimeter Reconstruction

The information coming directly from the ECAL is read out in terms of each cell’s electronics response. The ECAL reconstruction algorithms translate this into an energy value, which is then calibrated according to the cell’s energy and  $\eta$ -position. The algorithms also calculate quantities relevant to the quality of the deposit, in particular whether or not the deposit happened at a time consistent with the LHC bunch collisions, i.e. if it was “in time” as opposed to “out of time.” This information is especially useful in identifying apparent energy deposits that have been found to come from particles the signal-conversion electronics themselves (the transducers); these fake deposits were discovered during commissioning and are known as “ECAL spikes.” Since the spikes can imitate energy deposits from actual particles, they must be removed from the information used to reconstruct electrons and other particles. They can be distinguished from real particle deposits due to their timing as well as the fact that the surrounding crystals have no trace of a deposit. Therefore, if a high-energy deposit has no or very little energy in its neighboring crystals, or if its timing is not consistent with a bunch crossing, it is considered a spike and taken out of the reconstruction.

### 5.1.2 Track Reconstruction

A track is a sequence of hits in the tracker, reconstructed to trace the trajectory of a passing particle. The Kalman Filter algorithm is used by default for CMS tracks, but it is not good at catching abrupt changes in the electron trajectory due to bremsstrahlung. Therefore, the Gaussian Sum Filter algorithm is used for electrons,

because it is able to find those hits in unexpected directions.

#### 5.1.2.1 Kalman Filter

The Kalman Filter (KF) tracking method [35] is seeded [36] by pairs of hits in the pixel detector. The seeding algorithm first searches for a hit in one of the outer layers of the pixel detector. If a hit is found, another hit is sought in a layer closer to the interaction point, looking in an  $\eta$ - $\phi$  window around the original hit. Only two out of the three pixel layers are required to have hits in order to maintain a high efficiency. Once a track seed is found, further hits are sought in each successive tracking layer. The Kalman filter method is used to predict possible locations for hits in the next layer based on the currently-known track parameters. Hits in that area are then sought and included in the track, combining each hit with the predicted location for that layer and weighting each value depending on the value's uncertainty. If there are multiple candidate hits in the next layer, a possible trajectory is calculated for each hit, along with a trajectory accounting for the case in which the hit in that layer was lost. This procedure is repeated for each layer: each of the calculated trajectories for a given layer is matched to hits in the next layer, for which new trajectories are calculated. To prevent the number of necessary calculations from growing too large, the number of possible trajectories at each step is capped at five. In the case of multiple possible trajectories for a given fully-reconstructed track, defined by two trajectories sharing more than half of each of their hits, the track candidate with fewer hits (or, in the case of the same number of hits, the track with the worst fit) is discarded.

### 5.1.2.2 Gaussian Sum Filter

The Kalman Filter track-fitting does not accurately account for the behavior of particles in a material, specifically energy lost in the material and changes in direction due to radiation. The KF description is in particular inadequate for electrons, which readily interact with matter in these ways. The Gaussian Sum Filter (GSF) algorithm [37] was therefore developed: essentially a Kalman Filter with a more sophisticated energy loss modeling. Instead of approximating the energy loss (which is non-Gaussian) with a Gaussian distribution, which KF implicitly does, the GSF method models it as a weighted sum of Gaussian distributions. This greatly improves the performance of the track-fitting for electrons. Figure 5.1 shows the  $\phi$ -position difference  $\Delta\phi$  between generated electrons and the reconstructed electrons, using the KF (dotted, red) and GSF (solid, blue) track-reconstruction algorithms. (The black, dot-dashed line is a version of the KF algorithm optimized for the HLT.) Figure 5.1a shows the results for 10-GeV electrons, while Figure 5.1b shows results for 30-GeV electrons. In both cases, the GSF algorithm performs better than the KF algorithm: the distributions for GSF are more peaked around zero, showing that there is less of a difference between the true and reconstructed values of  $\Delta\phi$ .

## 5.2 Electron Reconstruction

As an electron passes through the CMS detector, it leaves a signature pattern in the subdetectors. Characteristically, electrons produce a track in the tracker system, as well as an energy deposit in the electromagnetic calorimeter. Therefore an electron is reconstructed by matching tracks and energy clusters that appear to have been

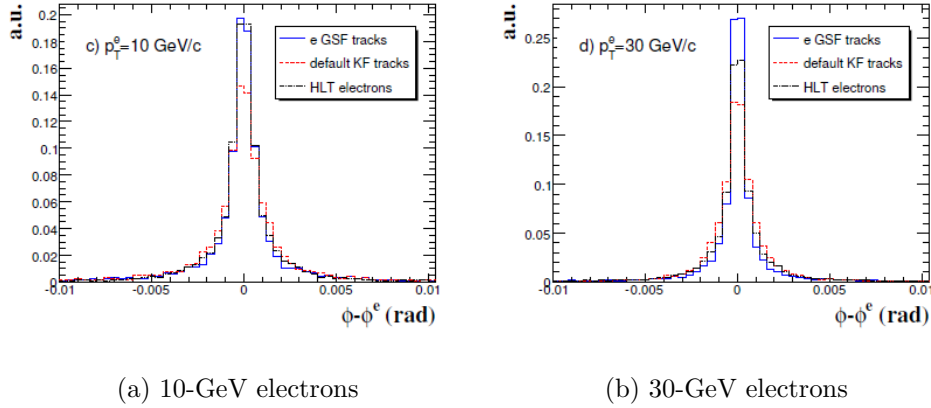


Figure 5.1: The  $\phi$  difference between Monte Carlo generated electrons and reconstructed tracks for different tracking algorithms: electron GSF tracks (solid, blue), KF tracks (dotted, red), and a version of the KF algorithm used at the HLT (dot-dashed, black). (a) shows results for 10-GeV electrons, while (b) displays 30-GeV electrons.

made by the same particle [38]. There are currently two approaches used to initiate electron reconstruction: the “ECAL-driven” method and the “tracker-driven” method, named according to which subdetector’s information initiates the reconstruction. Each method produces a collection of basic electron candidate objects, each consisting of a calorimeter cluster and hits in the first few layers of the tracker. These collections are then combined into one and used as seeds to reconstruct the electron tracks, producing fully-reconstructed electrons.

### 5.2.1 ECAL-driven Electron Seeding

The ECAL-driven electron reconstruction method starts with an energy deposit (or “supercluster”) in the ECAL and searches for hits in the pixel system that match the position of the calorimeter deposit.

### 5.2.1.1 Superclusters

The calorimeter energy deposit used in the electron reconstruction is called a supercluster: a cluster of clusters. A single electron or photon deposits most of its energy in a  $5 \times 5$  square of ECAL crystals, as shown in Figure 5.2. However, an electron passing through the tracker material in a strong magnetic field produces bremsstrahlung and electrons from photons that have pair-produced (or “converted”), causing the original electron’s energy to have spread out in  $\phi$  once it reaches the calorimeter. The process of creating a supercluster gathers these energy deposits to form the initial energy of the electron.

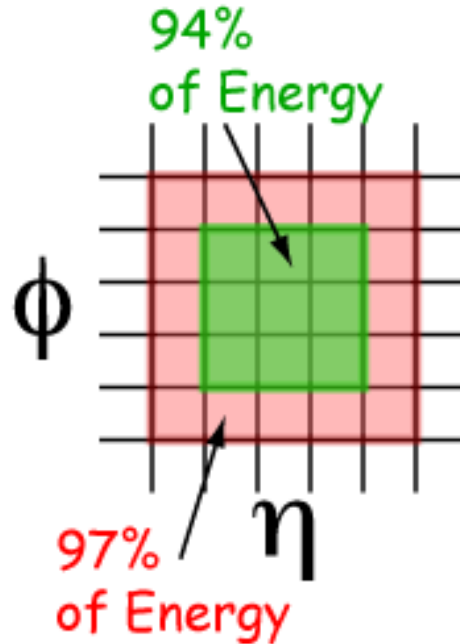


Figure 5.2: Typical energy distribution in a basic cluster.

The electron reconstruction currently uses two different superclustering methods, the “hybrid” supercluster method in the barrel, and the “multi5x5” clustering method

in the endcap. The hybrid algorithm forms superclusters and basic clusters from the same energy deposit information, while the multi5x5 algorithm first forms a single collection of basic clusters, which are then separately combined into superclusters.

The hybrid algorithm, shown in Figure 5.3, starts with a list of all ECAL crystals with an energy greater than a threshold; these crystals are considered seeds. Beginning with the highest seed crystal, the area around each seed is searched for energy deposits in steps of one crystal in  $\phi$ . For each  $\phi$  step, a “domino” of crystals is formed in  $\eta$ : one crystal to each side of the central crystal, or, if the energy sum of those three crystals is greater than a threshold, two crystals to each side of the central crystal, for a total of five crystals per domino. The process is done for a given number of  $\phi$  steps in both the positive and negative directions (currently 17 steps). As other seeds are encountered in this process, they are removed from the list of available seeds. Each domino with an energy higher than that of its two neighbors is considered as the seed for a basic cluster, and the collection of dominos formed by the search process is the basis for the supercluster. The basic clusters are formed by summing the energy of each local-maximum domino with those of its neighboring lower-energy dominos, excluding dominos that have already been used. The supercluster is then formed by summing the energies of the constituent basic clusters, with its seed considered to be the highest-energy basic cluster and its position given by the energy-weighted positions of the constituent clusters.

The multi5x5 algorithm, shown in Figure 5.4, first creates a collection of basic clusters from seeds, which are ECAL crystals with an energy higher than a given threshold. If a seed represents a local maximum, then its energy deposit is combined



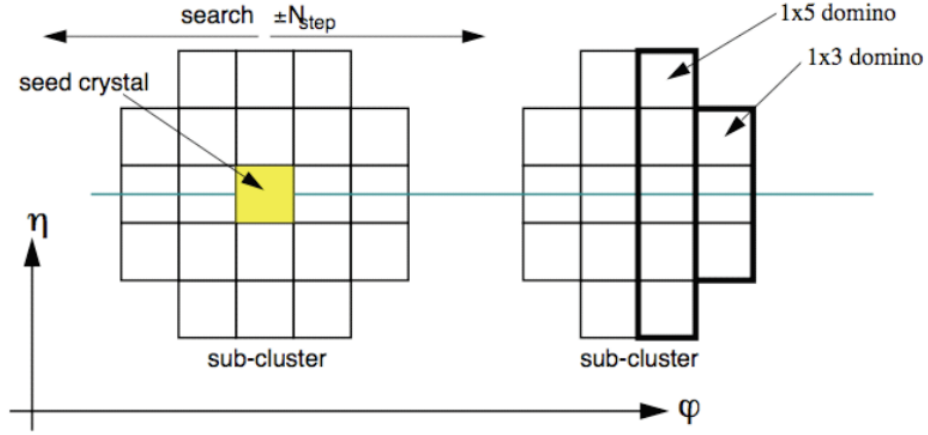


Figure 5.3: Illustration of the “Hybrid” supercluster algorithm. Dominoes with energy above a given threshold are constructed along the  $\phi$  direction in both directions out from the seed crystal.

with those from the crystals in the surrounding  $5 \times 5$  square to form a basic cluster, ignoring any crystals that have already been used to form the central  $3 \times 3$  part of another cluster. The basic clusters are then used as seeds for the superclustering algorithm. For each seed cluster with energy higher than a threshold, the energies of any other clusters within an  $\eta$ - $\phi$  window of the seed (longer in  $\phi$  than in  $\eta$ ) are combined with its own energy to create the supercluster, leaving out clusters that have already been used to form another supercluster. The position of the supercluster is given by the energy-weighted position of the individual clusters.

#### 5.2.1.2 Pixel Hit-matching

To reconstruct the full electron, the supercluster must be matched with a track. This is done by extrapolating the probable position of tracker hits from the supercluster’s position, as illustrated in Figure 5.5. Given the supercluster energy and the fact

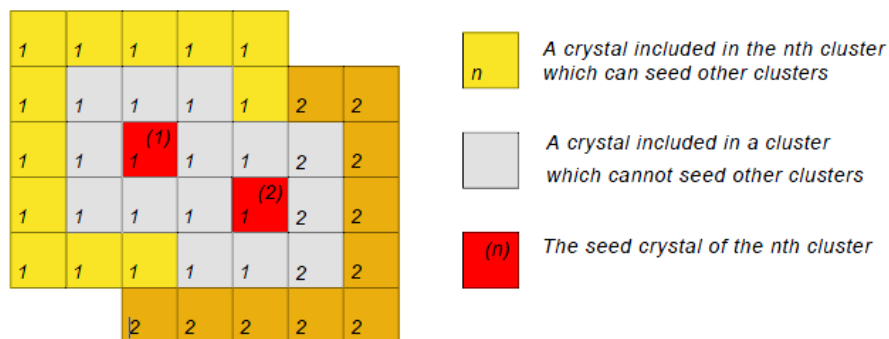


Figure 5.4: Illustration of the “Multi5x5” supercluster algorithm. Clusters seeded by seed crystals are grouped into superclusters.

that a non-radiating electron would have hit the calorimeter at the energy-weighted center of the supercluster’s energy spread, the electron’s initial (pre-radiation) trajectory through the tracker can be calculated for both the positive and negative electron charge cases. The reconstruction algorithm then looks for a matching hit in the first pixel detector layer within a  $\phi$ - $z$  window of this position for each charge case. If a hit is found, another hit is sought in the second pixel layer within a different  $\phi$ - $z$  window of the hit in the first layer.

### 5.2.2 Tracker-driven Electron Seeding

In the tracker-driven electron seeding method, electron-finding is seeded by tracks, which are followed out to the ECAL to search for calorimeter clusters associated with each track. This method was developed to better deal with low- $p_T$  electrons, for which the energy deposits from bremsstrahlung may be too widely separated to be matched, and non-isolated electrons within jets, whose energy deposits are not necessarily distinguishable from those of surrounding hadrons. For these electrons

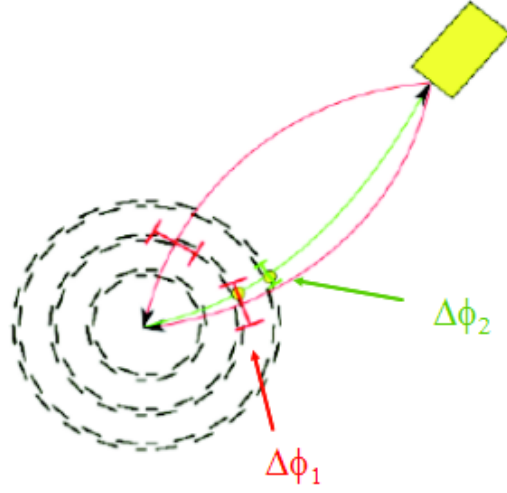


Figure 5.5: Schematic of pixel-hit search algorithm in electron-seeding. For both the positive and negative electron charge cases, a possible trajectory is extrapolated back from the calorimeter deposit given the deposit's energy. A hit is sought along either trajectory in either the inner or middle pixel layer within a window ( $\Delta\phi_1$ ). If a hit is found, a second hit is sought along that trajectory in the next pixel layer(s) ( $\Delta\phi_2$ ).

the calorimeter cluster-based seeding does not perform as well as for isolated, high- $p_T$  electrons.

The tracker-driven electron seeding method takes as input the default collection of tracks, obtained by an iterative usage of the KF algorithm. The method first tries to follow each track all the way to the calorimeter and search for nearby energy clusters. All clusters with an acceptable energy/momentum ( $E/p$ ) ratio with respect to the track are tested, and the cluster closest in  $\eta$ - $\phi$  space to the track is the one chosen.

Out of the tracks that were not well associated to any energy cluster, a preselection is applied to select those tracks that may have resulted from radiating electrons, which would not have been found by the cluster-matching method. If the track was

not matched because it had too few tracker hits and could not be traced to the calorimeter, or if the KF algorithm did not fit the track well enough because of possible bremsstrahlung, the tracks are passed on to the next step of the selection. A reduced GSF track-fitting algorithm is then run on these tracks, in an attempt to recover the bremsstrahlung-induced changes in track direction. This reduced version of the GSF algorithm runs much faster than that with the default parameters, but the performance is slightly reduced.

Finally, a multi-variate analysis (MVA) using boosted decision trees is performed on these candidates. The MVA algorithm is calibrated on a sample of electrons from  $b\bar{b}$  events, which are primarily non-isolated, and a sample of  $Z \rightarrow e^+e^-$  events, which provides high- $p_T$  electrons. The output of the MVA is a number indicating the likelihood of the object being an electron. Those objects whose MVA output is greater than a threshold are considered electron candidates. These candidates are then combined with those previously identified from the cluster-matching to produce the final collection of tracker-driven electron seeds.

### 5.2.3 Electron Track Reconstruction

The full collection of electron seeds, both ECAL- and tracker-driven, are used as the basis for reconstructing the electron track and hence completing the electron reconstruction. As mentioned previously, the electron reconstruction uses the GSF algorithm to reconstruct tracks. The track reconstruction efficiency is shown in Figure 5.6 as functions of  $p_T$  (Figure 5.6a) and  $\eta$  (Figure 5.6b). The plot vs.  $p_T$  shows curves for barrel and endcaps together (solid) and the barrel only (dashed). The efficiency drops for very low- $p_T$  electrons and when including the endcap. The efficiency

vs  $\eta$  dips slightly around  $\eta = 1.5$ , due to the overlap between the barrel and endcap, and also decreases towards 2.5, the boundary of the tracker.

The kinematics of the reconstructed electron are assigned to be a weighted combination of those of the constituent supercluster and track, and the final electron collection is saved for further analysis. Figure 5.7 shows the electron energy resolution on measurements from the ECAL (downward-pointing triangles), the tracker (upward-pointing triangles), and both measurements combined (circles). The ECAL has much better resolution at higher energy, while the tracker is better at lower energies. Combining the two gives better performance than either alone, especially around the region of 15 GeV.

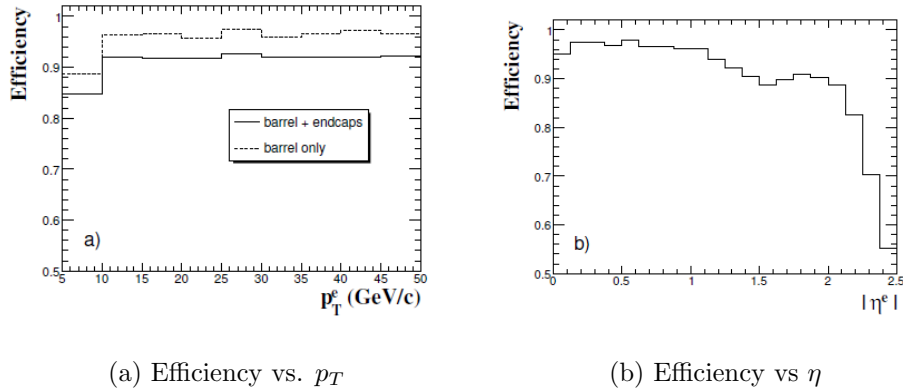


Figure 5.6: Electron (GSF) track reconstruction efficiencies (a) vs.  $p_T$  and (b) vs.  $\eta$ . In (a), the solid line shows the efficiency for the barrel and the endcaps together, while the dashed line shows the efficiency for the barrel only.

### 5.3 Beam Spot Reconstruction

The region where the beams overlap and protons may interact, the “luminous region,” is called the beam spot. Typically this area is a few centimeters long, with

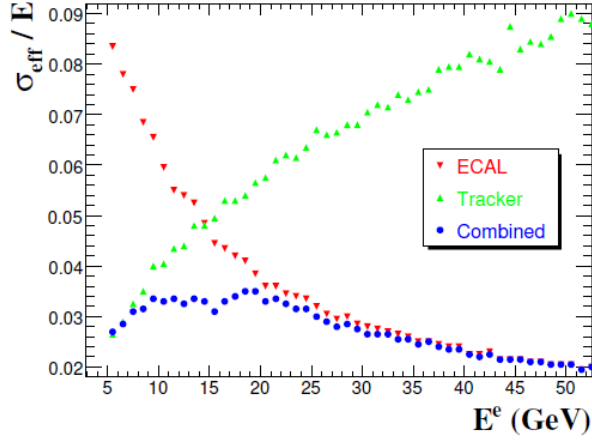


Figure 5.7: Electron energy resolution using different subdetectors' measurements: ECAL (downward-pointing triangles), tracker (upward-pointing triangles), and the two measurements combined (circles).

a width of 20-50 microns. The beam spot location can be used as an estimate for the initial position of tracks measured in the detector; it is therefore useful in track-seeding. Its position can be determined from measurements of tracks in the general track collection [39]. This is done by making a distribution of each track's distance of closest approach to the nominal beam spot (0,0,0) as a function of the track's  $\phi$  angle at its closest approach. If the beam spot is far from (0,0,0), the distribution looks sinusoidal. This distribution is then fit with a sine curve parametrized in the beam spot's actual  $x$ - and  $y$ -positions, and these values are extracted. Initially, one beam spot position was calculated for a full run. The calculation switched to using smaller run segments called "luminosity sections" (LS) in order to account for changes in the beam spot position during a run.

## 5.4 Primary Vertex Reconstruction

Since protons may collide anywhere within the region of beam overlap, the main interaction in a given event may not necessarily happen at the exact center of the detector. In particular, there may be a significant displacement in the  $z$ -direction. Determining the location of the main interaction, also called the primary vertex, is an integral part of reconstructing the event. For example, an electron may leave a deposit in a given calorimeter cell that has a fixed  $\eta$  position relative to the nominal interaction point, the very center of the detector (0,0,0). However, if the interaction producing the electron actually takes place at a different point, the electron's true  $\eta$  position will be different relative to the interaction. Therefore the position of the primary vertex should be taken into account when calculating the electron's  $\eta$  value.

The process of reconstructing the primary vertex [36] [40] involves creating primary vertex candidates from the tracks in the event, matching each track to the interaction that likely produced it. This is done by grouping the tracks according to their  $z$ -position at the point at which they pass most closely to the beam spot. The tracks are required to pass relatively close to the beamline, and they are also required to have a  $p_T$  greater than some threshold (with a default of 1.5 GeV). Tracks within a small distance (default 1 mm) of each other at the beam spot are considered to have come from the same vertex, and the primary vertex candidates are formed from these groups of tracks. At this point a fit is applied to each primary vertex candidate, and tracks found to be incompatible with the candidate are discarded until all tracks meet a given compatibility level. Finally, vertices that are incompatible with the position of the beam spot are discarded. (A second algorithm uses the beam spot as constraint on

the position of the vertex fit itself, but this algorithm was not fully commissioned at the time of this study.) If no reconstructed primary vertex candidates are found in an event, a “fake” primary vertex is added at the position of the beam spot. Since more than one interaction per event is possible but generally only one is of interest (the “primary” interaction), multiple candidates are ordered according to the transverse energy of their constituent tracks, and the highest of these is taken to be the primary vertex.



## Chapter 6

### Event Selection

Most analyses, including this one, are only interested in particle interactions that happen relatively rarely during proton collisions. Therefore, methods have been developed to sort through all the events and select the interesting ones for further study. This selection takes place both “online,” in real time as the detector is running, and “offline,” after the previously-selected data has been stored. The online selection serves primarily for reducing the volume of data enough that it can be stored, and so it is done centrally. In addition, the online selection is fairly general, while the offline selection is much more detailed and specific to individual analyses, and hence it is mostly done by the user of the data.

#### 6.1 Online

The online selection consists mainly of the trigger system, described in technical detail in Section 3.3.7. The implementation of the trigger system’s algorithms that are relevant to this analysis is discussed in the following sections, including both the Level-1 and the High-Level Triggers. Both levels reconstruct possible physics objects and apply criteria to select the interesting events. In general, the processing at the

Level-1 is quicker and coarser in order to sort through a larger volume of data, while the High-Level Trigger processing can afford to be longer and more thorough because it only deals with data not already discarded by the Level-1. In addition, as a last step, the information from the High-Level Trigger is used to group the data into primary datasets which are used as the basis for the offline selections.

### **6.1.1 Trigger Eras**

Since the LHC began taking data the event rate has changed by several orders of magnitude, and the trigger menus have evolved accordingly to deal with the changes. Initially, the collision rate was so low that minimum bias triggers ran unprescaled, so they were used to take the first analysis data. However, the collision rate soon increased to the point where the minimum bias trigger rate became too high and had to be prescaled, and electromagnetic object triggers were instead used to specifically capture events with electron-like objects. Eventually the electromagnetic trigger rate at the desired threshold also became too high, necessitating the extra constraints of the electron trigger at the same threshold. The rate for that trigger also increased, so to avoid prescaling the rate or increasing the threshold, tighter selection criteria were applied to the objects that fired the trigger. These criteria are looser than those applied in the course of this analysis and so are not expected to seriously affect the trigger efficiency for the analysis sample.

### **6.1.2 Level-1 Trigger**

Reconstructing and triggering on an electron with the Level-1 Trigger involves information from the calorimeters, processed by the Regional Calorimeter Trigger,

Global Calorimeter Trigger, and Global Trigger. Electrons and photons are indistinguishable in the L1 trigger and are therefore treated the same, as “ $e/\gamma$ ” (or EG) objects.

The RCT processing was described in detail in Section 3.3.7.2; this section provides details on the full-chain processing of  $e/\gamma$  triggers. The ECAL trigger primitive generation system (TPG) combines the energy deposits from a 5x5 square of ECAL crystals into a single energy value corresponding to one trigger tower. In addition, for each tower the ECAL TPG calculates a “fine grain veto” bit: if most of the tower’s energy is deposited in a 2x5 strip of crystals, then the energy pattern is considered consistent with that of an electron or photon, and the veto bit is not set. Otherwise, the veto bit is set. Similarly, the HCAL also combines energy deposits into trigger towers; however, the HCAL fine grain structure bit is not used in electron-finding. The information from the ECAL and HCAL is compressed and sent to the Regional Calorimeter Trigger. The RCT does the main job of electron-finding using several algorithms, detailed in Section 3.3.7.2 and recapped here. The decompressed ECAL energy of each trigger tower is examined and compared to that of its four adjacent neighbors. If the energy of the tower is greater than that of its neighbors, it is considered an  $e/\gamma$  candidate. The candidate energy is set to the energy of the tower in question plus that of its highest-energy neighbor. However, if the tower’s fine grain bit is set, or if the ratio of the tower’s HCAL energy to ECAL energy is too high, it is vetoed as a candidate. A candidate is additionally considered “isolated” if, out of the eight towers directly surrounding it, there are five contiguous towers forming an L-shape whose energies are low and who pass the fine grain and HCAL/ECAL

ratio veto. Otherwise, the candidate is “non-isolated.” The RCT sends the collections of isolated and non-isolated candidates to the Global Calorimeter Trigger, which sends the highest-energy ones to the final step of the L1, the Global Trigger. The Global Trigger then applies the criteria determining whether or not this event passes the current set of trigger paths, for example, “two  $e/\gamma$  objects with energy above 10 GeV” or “one  $e/\gamma$  object with energy above 17 GeV.” For this analysis, the L1 trigger used only required one  $e/\gamma$  object, above a threshold which changed from 5 GeV to 8 GeV as the luminosity increased (L1\_EG5 and L1\_EG8). A low threshold is used at the Level-1 Trigger to avoid interfering with the performance of the higher thresholds used in the High-Level Trigger. Efficiency distributions as a function of reconstructed supercluster  $E_T$  for the 5 and 8 GeV triggers are shown in Figure 6.1, using  $20 \text{ nb}^{-1}$  of early collision data. The efficiency is defined as the fraction of reconstructed electrons with  $E_T$  in a given bin that caused the given trigger to fire. The distributions are divided into barrel-only and endcap-only plots. In each case, a high efficiency is not reached until the supercluster  $E_T$  is several GeV above the Level-1 threshold. However, the HLT paths seeded by these triggers require a higher value of  $E_T$ , such that the Level-1 efficiency has already reached the maximum value and therefore does not cause a problem.

### 6.1.3 High-Level Trigger

The algorithms used to reconstruct trigger objects in the High-Level Trigger are the same as those used in the offline analysis and are described in Chapter 5. However, because of timing considerations, the algorithms are combined and configured differently at the HLT. The HLT has a limited amount of time in which to make a

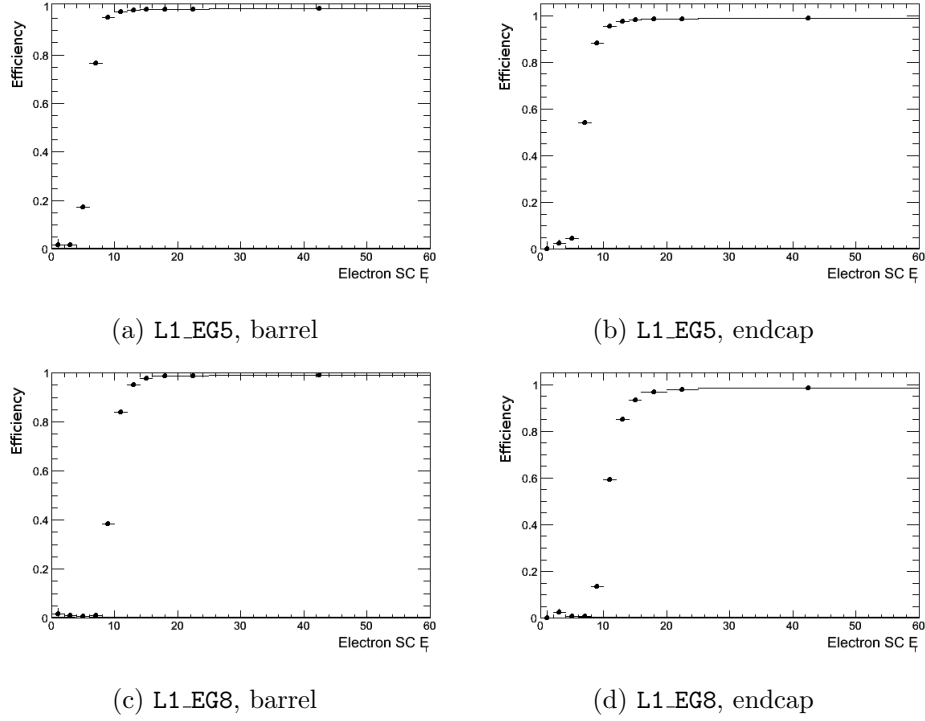


Figure 6.1: Efficiency distributions as a function of reconstructed supercluster  $E_T$  for the Level-1 5 and 8 GeV triggers using  $20 \text{ nb}^{-1}$  of early collision data. The efficiency is defined as the fraction of reconstructed electrons with  $E_T$  in a given bin that caused the given trigger to fire. (a) and (b) show barrel and endcap respectively for L1\_EG5, and (c) and (d) show barrel and endcap for L1\_EG8. In each case, a high efficiency is not reached until the supercluster  $E_T$  is several GeV above the Level-1 threshold.

keep/discard decision for a given event in order to keep up with the flow of events. Therefore the algorithms are optimized for the best performance in the shortest time, which in practice means fewer steps and less complexity than the implementation at the offline level, where no such constraint exists. In particular, while the offline-reconstructed electron collection includes tracker-driven electrons, those reconstructed at the HLT are ECAL-driven only, and the supercluster reconstruction algorithm (Section 5.2.1.1) uses a lower number of steps in the search process. Also, the size of the

windows in which to search for hits in the pixel-matching part of the reconstruction (Section 5.2.1.2) is larger than that used offline, to guarantee a high efficiency.

The luminosity increase and consequent evolution of trigger menus described in Section 6.1.1 required incremental changes in the definitions of the current HLT paths. However, a few requirements remained common to all the paths used. In particular, the execution of each path begins by taking the Level-1 objects that passed the given L1 seed path and retrieving the information from the ECAL regions around those objects. From this information, clusters of energy deposits are identified, and clusters having too narrow a spatial distribution are rejected as being spikes. The trigger paths used in this analysis, shown in chronological order in Table 6.1, all required (at least) one  $e/\gamma$  or electron candidate above a certain energy threshold, with possible other criteria applied to the candidate as well.

Table 6.1: Trigger paths used to select data, in chronological order of use. See text for explanation of path names.

Trigger	L1 Seed
HLT_Photon15_Cleaned_L1R	L1_EG5
HLT_Ele15_LW_L1R	L1_EG8
HLT_Ele15_SW_L1R	L1_EG8
HLT_Ele15_SW_CaloEleId_L1R	L1_EG8
HLT_Ele17_SW_CaloEleId_L1R	L1_EG8
HLT_Ele17_SW_TightEleId_L1R	L1_EG8
HLT_Ele17_SW_TighterEleIdIsol_L1R	L1_EG8

The paths are named according to the following considerations. Initially, the LHC collision rate was low enough that loose requirements and low thresholds could be used without overwhelming the system. The first trigger used did not require any

matches to hits in the pixel part of the tracker, in contrast to all subsequent trigger paths used – without tracking requirements, it was by definition a “Photon” trigger, as opposed to the “Electron (Ele)” triggers. The designation “Cleaned” means that a spike-cleaning algorithm was in place, as well. After a few menu iterations the energy threshold applied to the candidate, designated by the number in the path name, increased from 15 GeV to 17 GeV. The size of the window used to search for potential pixel matches also decreased, from “large-window” ( $LW$ ) to “startup-window” ( $SW$ ). Later, further criteria were applied to the shape of the total energy deposit ( $\sigma_{in\eta}$  ,  $H/E$ ); since this information comes only from the calorimeter, paths with such constraints have “Calo” in their name. Later paths included additional criteria, on the quality of the match between the energy cluster and the track that make up the electron ( $\Delta\eta_{in}$  ,  $\Delta\phi_{in}$  ), and were designated as “Tight” or “Tighter” according to the stringency of their constraints. Finally, constraints were added for the amount of energy surrounding the electron candidate, or “isolations” designated by “Isol” in the path name. These further criteria are described in more detail in Section 6.2.1; in the current section it is sufficient to say that they were added in steps to the trigger paths to gradually tighten the selection. Efficiency distributions using  $20 \text{ nb}^{-1}$  of data for an early trigger are shown in Figure 6.2. In this case, the efficiency is defined as the fraction of reconstructed electrons with  $E_T$  in a given bin that caused the given trigger to fire. Figure 6.2a shows the efficiency for the barrel, while Figure 6.2b is for the endcap (the empty bin is due to lack of statistics). The trigger reaches maximum efficiency well below the energy threshold used in the offline analysis, so the inefficiency at the “turn-on” does not affect the offline analysis.

However, the efficiencies for the triggers used in this analysis were determined using the tag-and-probe method, detailed in Section 6.2.2.2. The results for each of the triggers are also given in that section.

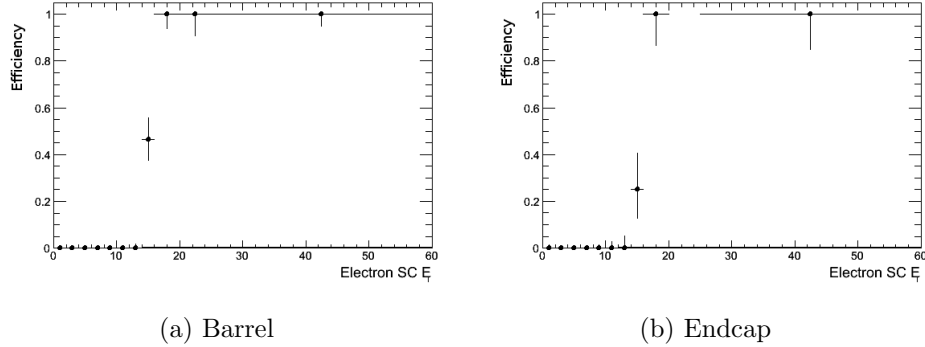


Figure 6.2: Efficiency distributions as a function of reconstructed supercluster  $E_T$  for an early HLT trigger using  $20 \text{ nb}^{-1}$  of collision data, `HLT_Phot15_L1R`. The efficiency is defined as the fraction of reconstructed electrons with  $E_T$  in a given bin that caused the given trigger to fire. (a) and (b) show barrel and endcap respectively. The empty bin in (b) is due to lack of events in that bin.

#### 6.1.4 Primary Datasets

The final step done centrally is the grouping of events passing similar HLT paths into primary datasets for storage. For example, in early running, all events passing a minimum-bias trigger were put into the MinimumBias dataset. Once the event rate increased and physics triggers fired more often, events were put into more specific datasets such as EG for all events passing  $e/\gamma$  (electron or photon) triggers, or later, Electron for all events specifically passing electron triggers. These primary datasets are the groupings of stored data that the offline analyses begin with. The specific datasets used for this analysis are given in Table 6.2.



Table 6.2: Primary datasets used in this analysis.

Dataset
/EG/Run2010-Dec22ReReco_v1/AOD
/Electron/Run2010b-Dec22ReReco_v1/AOD

## 6.2 Offline

The offline selection consists of any criteria applied to the data after it has already been stored, i.e. criteria applied to an already-existing primary dataset. This analysis uses data from two consecutive primary datasets: the EG dataset gathered during earlier data-taking (Run2010A, from run 135821 to run 144114), and the Electron dataset from later data-taking (the Run2010B era, runs 146240 to 149711). In addition, it is required that the primary vertex of each event be “good”: that is, within 24 cm of the nominal interaction point in the longitudinal direction and 2 cm in the transverse direction, and having a minimum of 4 degrees of freedom (called NDOF), which is a measure of the quality of the vertex fit. More detailed selections are applied to the event contents, which will be discussed in the following sections. The electrons in these events are required to pass a series of criteria to determine “good” electrons. Finally, specific selections are made on the characteristics of the event as a whole in order to get the final collection of  $Z \rightarrow e^+e^-$  candidate events.

### 6.2.1 Electron Selection

The electron selection starts with the full set of objects reconstructed as electrons, i.e. ECAL energy deposits (superclusters, see Section 5.2.1.1) matched with nearby tracks. The objects in this collection are not necessarily real electrons but are consistent with the electron signature at a low level. In order to select the reconstructed objects most likely to be real electrons from a  $Z$ , sets of further conditions are applied. First the electrons are required to be within the  $\eta$  region of ECAL in

which they can be fully measured, in the barrel,  $0 < |\eta| < 1.4442$ , and in the endcap,  $1.566 < |\eta| < 2.5$ . A 25-GeV cut on the supercluster transverse energy is applied, followed by a set of cuts designed to reject electrons from photon conversions. Another set of cuts aims to distinguish real electrons from other energy deposits which may mimic electrons, and finally a set of cuts to make sure the electron is isolated, i.e. not part of a jet unrelated to the  $Z$ .

The CMS vector boson analysis team created several different electron selections of varying cut tightness, based on a given efficiency of the cuts [41]. A tighter selection in general results in a purer sample of true electrons, but throws away many more real electrons than a looser selection. These “working points” have target efficiencies ranging from 95%-efficient at the loosest (WP95) to 60% at the tightest (WP60). For early data-taking the WP95 and WP80 selections were chosen as the baseline selections for the  $Z \rightarrow e^+e^-$  and  $W \rightarrow e\nu$  analyses, respectively. As more data accumulated, it became clear that WP80 provided better performance than WP95 for the  $Z \rightarrow e^+e^-$  analysis, as well. A deciding factor in the switch was the fact that the evolving trigger paths eventually used selections that were tighter than those used in the offline (WP95) analysis. This analysis uses the WP80 set of cuts for the complete dataset.

The plots in the following sections showing the distributions and cut values only display simulated data. The QCD Monte Carlo sample has effective electron isolation cuts already applied, so until the corresponding selection cuts are applied to data, the data does not agree with the Monte Carlo distributions. However, after all cuts have been applied the agreement is good; this will be demonstrated in a later section. All

results plots include the data distributions.

#### 6.2.1.1 Conversion Rejection

The conversion rejection step of the electron selection aims to eliminate photons that have converted into electron pairs. Several variables have been chosen to distinguish between conversions and prompt electrons (electrons from the interaction of interest), focusing on the track properties. Since prompt electrons are expected to hit the first layer of the tracker, any electron-associated track that is missing initial hits can be rejected as a conversion that occurred within the tracker. The looser requirements of the 95%-efficient working point allow an electron to have one missing hit; tighter working points such as WP80 require zero missing hits. Figure 6.3a shows the number of missing hits for each electron. In addition, the conversion rejection algorithm searches for candidate electron-pair partner tracks, i.e. track pairs that appear to come from the same point. Every electron track is compared to all opposite-charge tracks within a  $\Delta R$  cone of 0.3, and two values are calculated: a measure of the difference in the angles in the r-z plane between the two tracks ( $\Delta \cot \theta$ , Figure 6.3b), and the distance of closest approach between the two tracks in the x-y plane ( $dist$ , Figure 6.3c). Electron pairs from conversions are expected to have low values for both quantities, since both electron tracks begin at the point of conversion and initially have the same direction as the converting photon. The WP80 requirements apply a threshold at 0.02 for both quantities. The selection is such that an electron candidate that fails both the missing hits cut and one of the other cuts is rejected as a conversion. This way a single anomalous measurement does not result in a true electron being rejected.

### 6.2.1.2 Electron Isolation

The electrons from a Z decay are not expected to end up close to many other particles in the detector, since they are not produced as part of a jet. The object is to select those real electrons that are most likely to be prompt decay products, not those that come from some secondary interaction with many other end products. Therefore a set of cuts is applied requiring little detector activity in the area immediately surrounding the reconstructed electron. These so-called isolation cuts look at the energy deposits in the electromagnetic and hadronic calorimeters separately, as well as the total  $p_T$  of neighboring tracks, within specified  $\Delta R$  cones around the electron-associated deposit/track. These energies are divided by the  $p_T$  of the electron itself to arrive at a relative value, which allows for higher-energy particles that may deposit more energy in the surrounding area. The thresholds for each of the three types of isolation are set separately for barrel and endcap, because there is more material in front of the endcap, causing the electron energy to be more spread out. The thresholds are given in Table 6.3. Plots of the separate isolation distributions for both barrel and endcap are shown after the conversion rejection cuts in Figure 6.4 for track isolation, Figure 6.5 for ECAL isolation, and Figure 6.6 for HCAL isolation.

### 6.2.1.3 Electron Identification

Several “electron identification” variables are used to differentiate genuine electrons from other particles or conditions that may mimic electron behavior. Since an electron is reconstructed from a supercluster matched to a track, it is desired that the

Table 6.3: WP80 thresholds for relative isolation. The value of each type of isolation (ECAL, HCAL, track) is divided by the electron's  $p_T$ , and the result is required to be below the threshold.

Cut variable	Barrel	Endcap
Track	0.09	0.04
ECAL	0.07	0.05
HCAL	0.10	0.025

match is a good one. The quality of matching can be estimated by looking at measures of the distance between the two components. The position in  $\eta$  and  $\phi$  of the supercluster is compared with the  $\eta$  and  $\phi$  position of the track extrapolated back to the vertex, with the differences being labeled  $\Delta\eta_{in}$  and  $\Delta\phi_{in}$ , respectively. It is expected that a supercluster and track from the same electron will be close together, so upper limits on these quantities are defined as in Table 6.4. Distributions of electron  $\Delta\eta_{in}$  and  $\Delta\phi_{in}$ , each plotted after all the previous selection steps, are shown in Figure 6.7 and Figure 6.8.

The electron's energy deposit is also expected to be narrow relative to that of a jet. A measure of the width in the  $\eta$  direction is therefore calculated using the energies and positions of the individual ECAL crystals,  $\sigma_{i\eta i\eta}$ , and this quantity is required to be below the thresholds listed in Table 6.4. (The  $\phi$  direction is not examined because bremsstrahlung from the bending electron can cause a significant spread of the energy in  $\phi$ .) The definition of  $\sigma_{i\eta i\eta}$  is given in terms of the energies and  $\eta$  positions of the individual crystals  $i$  (including the seed crystal), as well as the energy and average position of the  $5 \times 5$  cluster of crystals:

$$\sigma_{i\eta i\eta} = \sqrt{\frac{\sum_i (\eta_i \times 0.0175 + \eta_{seed} - \eta_{5 \times 5}^{avg})^2}{\sum_i w_i}}$$

where each crystal's weight  $w_i$  is given by

$$w_i = 4.2 + \ln \frac{E_i}{E_{5 \times 5}}$$

The  $\sigma_{i\eta i\eta}$  distribution for electrons after all previous cuts is shown in Figure 6.9. In addition, an electron is expected to deposit most of its energy in the electromagnetic portion of the calorimeter. A large hadronic energy deposit is more likely to come from a jet, so a limit on the ratio of the energy deposit in the electromagnetic calorimeter to that in the hadronic calorimeter,  $H/E$ , is applied (values given in the table). The distribution of  $H/E$  for electron candidates is plotted after all previous selection steps in Figure 6.10.

Table 6.4: WP80 thresholds for electron identification variables. Each variable for a given electron is required to be below the stated threshold according to the electron's location in the detector. Definitions of the variables are given in the text.

Cut variable	Barrel	Endcap
$\sigma_{i\eta i\eta}$	0.01	0.03
$\Delta\phi_{in}$	0.06	0.03
$\Delta\eta_{in}$	0.004	0.007
$H/E$	0.04	0.025

#### 6.2.1.4 Matching Offline-Reconstructed Objects to Trigger Objects

In order to ensure that the offline-reconstructed objects being examined were also reconstructed by the trigger, each offline object is compared with the list of trigger objects firing a given path. If the offline object lies close enough to a trigger object (measured by  $\Delta R$ ), it is considered to have passed the trigger. Each event in this analysis was required to have at least one electron trigger-matched in this way, within

a  $\Delta R$  distance of 0.2. This demonstrates that the constituent objects in the event did in fact fire an appropriate trigger.

### 6.2.2 $Z \rightarrow e^+e^-$ Event Selection

In order to be included in the final selected sample of  $Z \rightarrow e^+e^-$  events, an event must have two electrons passing the selection cuts described in Section 6.2.1. Only one of the electrons is required to match to a trigger object, however; even if only one electron fires the trigger, the event is kept and the trigger’s purpose is served, and there is no necessity for both electrons to fire the trigger. The two electrons are also required to have an invariant mass between 60 and 120 GeV; this defines a window around the  $Z$  mass peak at about 91 GeV.

#### 6.2.2.1 Acceptance for $Z \rightarrow e^+e^-$ Events

The acceptance ( $A$ ) (see Section 1.5) is the factor representing the fraction of events theoretically able to be detected with the given experiment. It includes considerations related to a particle’s kinematic quantities (its position and momentum) as well as to the precise definition of the signal interaction. In particular, the particle-detecting elements of any given detector, including CMS, do not fully cover the area around the interaction point – by necessity, some of that area is taken up by the beam pipe. This means that any end-product particle that goes into a “dead” space instead of a detecting element will not be detected. Therefore the acceptance factor takes into account the actual solid-angle area covered by the relevant parts of the detector. In addition, it is generally more difficult to distinguish very low-energy objects from background noise, so the acceptance also includes a lower limit on the energy of the



particle.

In this analysis, the signal was defined to be those  $Z \rightarrow e^+e^-$  events whose invariant mass was between 60 and 120 GeV; this captures the Z peak around 91 GeV. The acceptance was defined as the fraction of those signal events whose electrons fall into the  $\eta$  region used for the analysis,  $|\eta| < 1.4442$  or  $1.566 < |\eta| < 2.5$ , and whose transverse energies were both above 25 GeV. These values can also be found in Table 6.5.

Table 6.5: Criteria for determining acceptance of  $Z \rightarrow e^+e^-$  events. Acceptance is defined as the fraction of signal events (within the mass window) whose two electrons pass the requirements in the table.

Kinematic quantity	Requirement
$\eta$	$ \eta  < 1.4442$ or $1.566 <  \eta  < 2.5$
$E_T$	$< 25\text{GeV}$

Acceptance cannot be calculated from data, because it is impossible to know how many events were missed – the only events we have are those which were not missed. Instead acceptance is determined by applying the defining criteria to a sample of simulated data, a sample large enough that statistical uncertainties become small enough to ignore. Since the simulated sample is expected to model real data well enough, this number is taken as the true acceptance for real data. However, the model used in simulation may actually differ slightly from physical reality. These possible differences are taken into account in the uncertainty calculated for the acceptance, which will be detailed in Section 7.2.3.

It is also useful to combine the supercluster reconstruction efficiency with the acceptance. The supercluster reconstruction efficiency is impossible to determine from

data for the same reason as for the acceptance – it would require knowing about events that were missed, in this case electrons that had impacted the detector (specifically ECAL) but which had not resulted in the formation of a supercluster. Therefore this was also determined from simulated data. Effectively it is combined with the acceptance by applying an additional requirement on the acceptance: the simulated event should have two electrons passing the  $\eta$  and transverse energy requirements, and those electrons should also both be matched to reconstructed superclusters. The fraction of total events passing these combined criteria is referred to as “ECAL acceptance” or  $A_{ECAL}$ .

The pure kinematic acceptance for this analysis was determined with the POW-HEG-generated Monte Carlo sample to be 0.423 and the ECAL acceptance was likewise calculated as 0.387. These values can also be found in Table 6.6.

Table 6.6: Acceptance values for  $Z \rightarrow e^+e^-$  events. Acceptance is defined as the fraction of signal events whose electrons can reasonably be expected to be seen by the detector. The criteria are give in Table 6.5.

Quantity	Value
$A$	0.423
$A_{ECAL}$	0.387

### 6.2.2.2 Efficiency of Selection for $Z \rightarrow e^+e^-$ Events

It is important to know how well the selection steps perform their task of keeping signal events; any signal events that are missed must be accounted for in the final calculation to get an accurate result. This factor is quantified in the efficiency, which is defined as the fraction of total objects or events passing a given selection. Simulated

data can be used to calculate efficiency, since it contains the “truth” information – the true total number of events, whether or not they survive a given selection step. However, the simulation may not correctly model some aspect of the real data, which would cause a discrepancy with the real-data efficiency and a corresponding inaccuracy in the final result. Therefore it is desirable to use so-called “data-driven” methods (see also Section 1.7), determining the efficiency as closely as possible using only the data itself. Because the truth information does not exist in real data, the number of events passing or failing a given selection must be determined with another method.

The tag-and-probe method is used to determine the efficiency of a given set of electron selection steps. In this method, a set of data events is identified which appear to be good  $Z \rightarrow e^+e^-$  candidate events. One of the electrons in each of these events must pass all selection cuts and essentially be identified as a golden electron; this is the tag. The criteria applied to the other electron are looser: it is not required to pass the selection cuts being tested. This is the probe electron. The event’s status as a  $Z$  candidate is determined by enforcing a mass window cut on the invariant mass of the tag-probe system (this is sufficient to select a high-purity sample of events in which both legs are real electrons). The naive selection efficiency is then given by the fraction of probe electrons that pass the requirement being tested.

However, a more sophisticated analysis of the efficiency can be performed by fitting the invariant mass spectra of the tag-probe pairs for both passing and failing probes to a lineshape representing both the signal and the background. Then the distribution of passing probes can be represented as the signal lineshape, multiplied by the efficiency and the total number of signal events, added to the background

lineshape, multiplied by the number of passing background events. The failing probe distribution can be represented in the analogous way, using  $(1 - \text{efficiency})$  instead. From this pair of fits the total number of events as well as the efficiency can be extracted simultaneously.

Several lineshapes were combined in this fit. The base signal lineshape was taken directly from a generator-level histogram of the  $Z \rightarrow e^+e^-$  invariant mass spectrum, which represents the true form of the invariant mass shape. This distribution was used together with a Gaussian distribution multiplied by a Crystal Ball function. The Gaussian has the general form

$$f(x) = \frac{1}{\sqrt{2\pi\sigma^2}} e^{-\frac{(x-\mu)^2}{2\sigma^2}}$$

and takes into account the “smearing” effects of the detector resolution: the measured values of a quantity form a distribution around the “true” value. The Crystal Ball (named after the Crystal Ball collaboration) has the form

$$f(x) = N \times \begin{cases} e^{-\frac{(x-\mu)^2}{2\sigma^2}} & \text{for } \frac{x-\mu}{\sigma} > -\alpha \\ A \times \left(B - \frac{x-\mu}{\sigma}\right)^{-n} & \text{for } \frac{x-\mu}{\sigma} \leq -\alpha \end{cases}$$

where

$$A = \left(\frac{n}{|\alpha|}\right)^n e^{\left(-\frac{|\alpha|^2}{2}\right)}$$

$$B = \frac{n}{|\alpha|} - |\alpha|$$

The Crystal Ball function is used to model processes where energy may be lost in the measurement. Together they factor in the changes to the invariant mass spectrum due to detector limitations. The two shapes were combined by a process called convolution;

the convolution of two distributions  $f(x)$  and  $g(x)$  is calculated by

$$(f * g)(x) = \int_{-\infty}^{\infty} f(y)g(x - y)dy$$

Convolving the distributions of two independent random variables gives the proper combined distribution, as opposed to addition or multiplication. The background was represented by an exponential lineshape, of the form

$$f(x) = \begin{cases} \lambda e^{-\lambda x} & \text{for } x \geq 0 \\ 0 & \text{for } x < 0 \end{cases}$$

The parameters and relative weights of the different lineshapes were varied to get the combination that best fit the actual data distribution. An example of the result of this fit is shown in Figure 6.11, for the isolation selection step in the barrel. Figure 6.11a shows passing probes only, Figure 6.11b shows failing probes only, and Figure 6.11c shows the fit for all probes. Black points are data, the solid line is the signal lineshape, and the dotted line is the background lineshape. In the “passing probes” and “all probes” plot, the contribution from background is very small.

However, the tag-and-probe may possibly introduce a bias into the calculation, in particular if observing one leg makes it more likely that the other leg is observed. For example, if the electrons are essentially back-to-back, one is more likely to fall within the detector coverage if the other one does as well. In addition, there is a slight discrepancy between the efficiencies calculated using data and those using the standard Monte Carlo sample. Therefore, the strategy in this analysis is to calculate the “true” efficiency from the simulation sample, as well as the tag-and-probe efficiencies from the real data and simulation samples. The “true” efficiency is then corrected by the

ratio of the data and simulation tag-and-probe efficiencies:

$$\epsilon^{corrected} = \epsilon_{MC}^{true} \times \left( \frac{\epsilon_{data}^{T\&P}}{\epsilon_{MC}^{T\&P}} \right)$$

This implies a certain amount of trust in the generator-level simulation of the interaction. The corresponding uncertainty in the efficiency due to the generator-level simulation is dealt with in Section 7.2.4.2.

The event selection efficiency in this analysis is determined by first obtaining the efficiencies of the individual selection steps given above. This also includes the initial step of reconstructing the electron objects from superclusters. Since each selection step is applied one after the other, the overall selection efficiency is given by the product of the individual efficiencies. In addition, since most steps are required to apply to both electrons, the single-electron efficiencies of these steps (the result of the tag-and-probe method) are squared to get the efficiency of both electrons passing that step. The trigger step, however, is a special case since only one electron is required to pass. In this case, the quantity used is the probability that at least one electron passes, which is equivalent to the probability both electrons fail subtracted from 1.

The formula used to calculate the overall event selection efficiency from the individual step efficiencies is therefore

$$\epsilon = (\epsilon_{reco}^2) \times (\epsilon_{isol}^2) \times (\epsilon_{ID}^2) \times (1 - (1 - \epsilon_{trig})^2)$$

The efficiencies are given for each selection step in Table 6.7 and for all the triggers used in data individually in Table 6.8. The full event selection efficiency was calculated to be  $61.0 \pm 0.5\%$ .

Table 6.7: Individual efficiencies of electron selection steps: reconstruction, isolation, identification, trigger, and the overall event selection efficiency.

Step	True MC	MC T&P	Data T&P	Ratio	Efficiency
Reco	0.965	0.972	$0.971 \pm 0.002$	$0.999 \pm 0.002$	$0.964 \pm 0.002$
Iso	0.926	0.927	$0.910 \pm 0.003$	$0.976 \pm 0.003$	$0.905 \pm 0.003$
ID	0.906	0.907	$0.897 \pm 0.003$	$0.989 \pm 0.003$	$0.896 \pm 0.003$
Trigger	0.959	0.941	$0.972 \pm 0.001$	$1.032 \pm 0.001$	$0.991 \pm 0.001$
Overall	0.654	0.665	$0.621 \pm 0.005$	$0.933 \pm 0.007$	$0.610 \pm 0.005$

Table 6.8: Efficiencies of all the triggers used in data as determined with the tag-and-probe method. A description of the fit is given in the text.

Trigger	Efficiency	Error (fit)
HLT_Photon15_Cleaned_L1R	0.976	0.002
HLT_Ele15_LW_L1R	0.961	0.005
HLT_Ele15_SW_L1R	0.981	0.003
HLT_Ele15_SW_CaloEleId_L1R	0.986	0.003
HLT_Ele17_SW_CaloEleId_L1R	0.992	0.002
HLT_Ele17_SW_TightEleId_L1R	0.973	0.002
HLT_Ele17_SW_TightEleIdIsol_L1R_v1	0.973	0.003
HLT_Ele17_SW_TightEleIdIsol_L1R_v2	0.977	0.002
HLT_Ele17_SW_TightEleIdIsol_L1R_v3	0.974	0.003
Overall	0.9763	0.0009

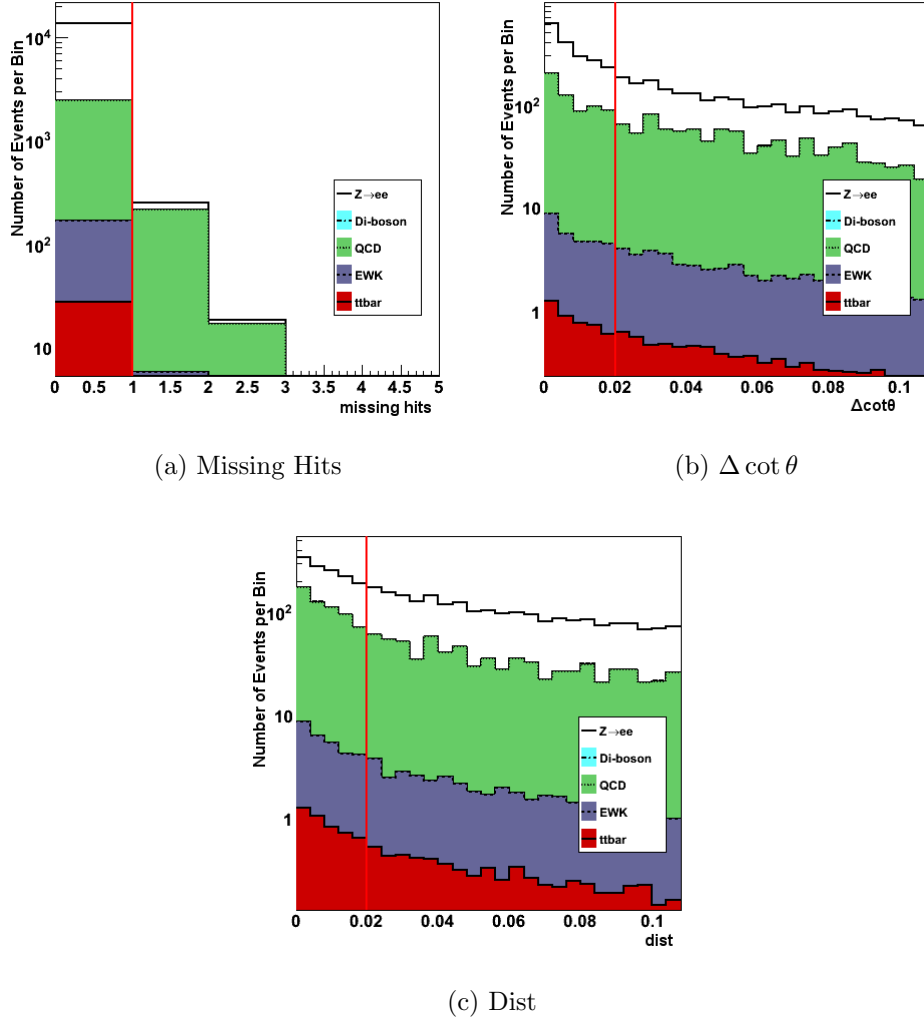


Figure 6.3: Conversion rejection variables after  $E_T$  cut: (a) the number of missing hits in the tracker, (b) the value of  $\Delta \cot \theta$  between the electron track and any partner track, and (c)  $dist$ , the distance of closest approach between the two tracks. The solid line against the white background shows the signal sample; the shaded areas with varied linestyles show the backgrounds. The vertical line shows where the cut was made.



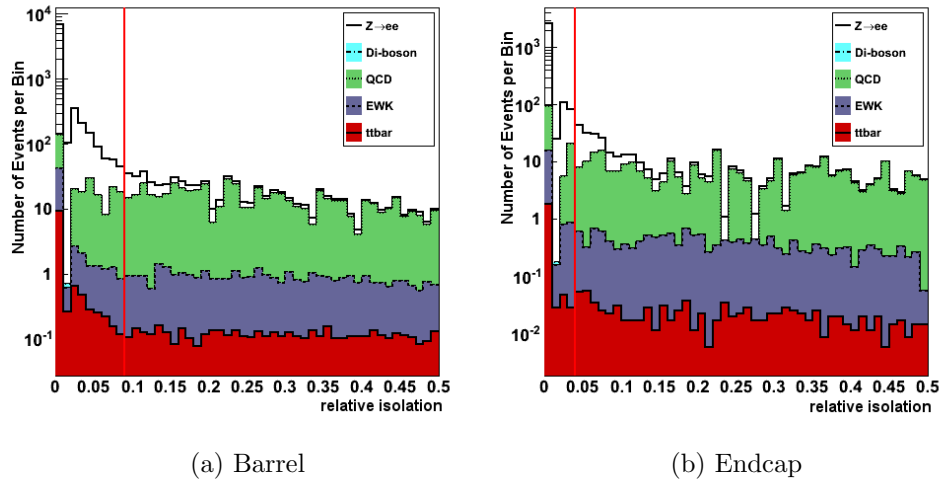


Figure 6.4: Electron tracker isolation variables after  $E_T$  and conversion rejection cuts, for (a) barrel and (b) endcap. Relative tracker isolation is equal to the sum of the  $p_T$  of tracks in a cone around the electron, divided by the electron's  $p_T$ . The solid line against the white background shows the signal sample; the shaded areas with varied linestyles show the backgrounds. The vertical line shows where the cut was made.

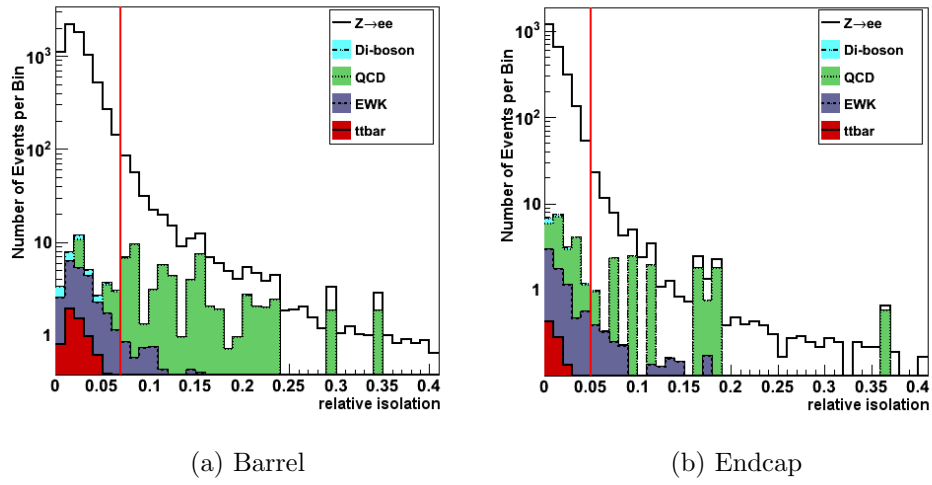


Figure 6.5: Electron ECAL isolation variables after  $E_T$ , conversion rejection, and tracker isolation cuts. Relative ECAL isolation is equal to the sum of the  $E_T$  of ECAL deposits in a cone around the electron, divided by the electron's  $p_T$ . The solid line against the white background shows the signal sample; the shaded areas with varied linestyles show the backgrounds. The vertical line shows where the cut was made.

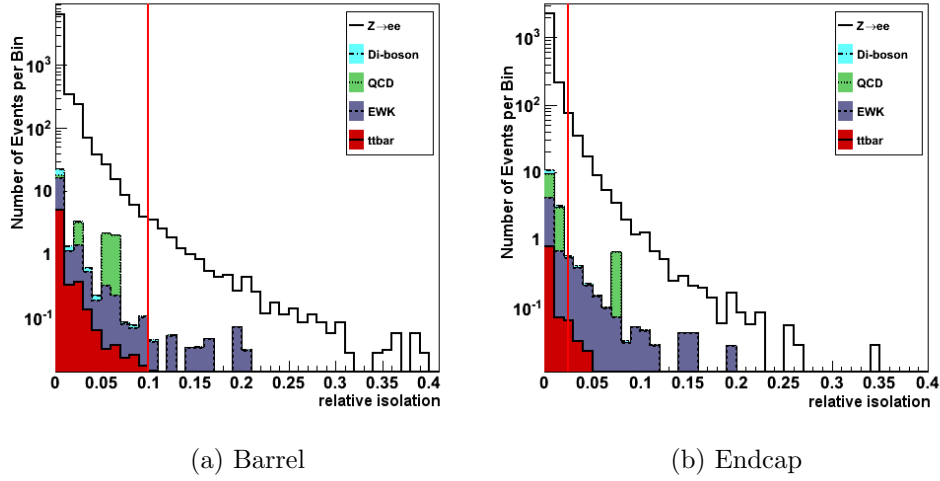


Figure 6.6: Electron HCAL isolation variables after  $E_T$ , conversion rejection, and tracker and ECAL isolation cuts. Relative HCAL isolation is equal to the sum of the  $E_T$  of HCAL deposits in a cone around the electron, divided by the electron's  $p_T$ . The solid line against the white background shows the signal sample; the shaded areas with varied linestyles show the backgrounds. The vertical line shows where the cut was made.

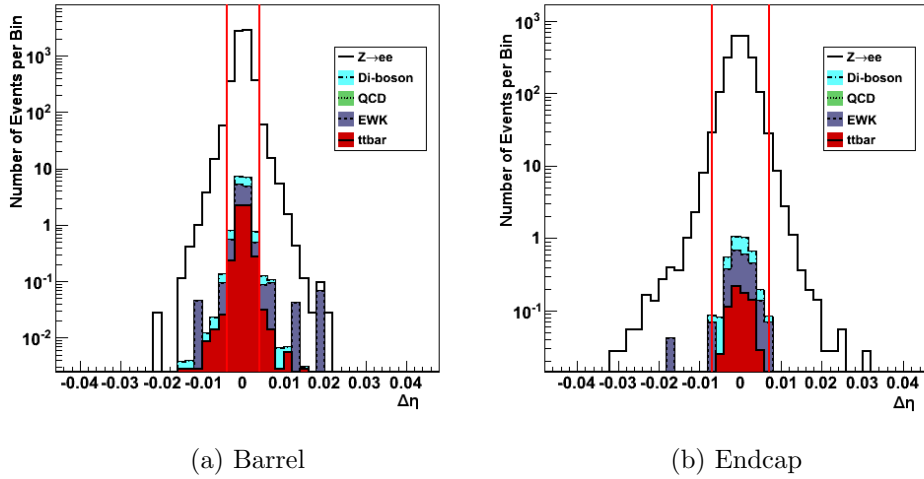


Figure 6.7:  $\Delta\eta_{in}$  electron identification variables after  $E_T$ , conversion rejection, and isolation cuts. A low  $\Delta\eta_{in}$  indicates a good match between an electron candidate's supercluster and track. Values shown for (a) barrel and (b) endcap. The vertical line shows where the cut was made.

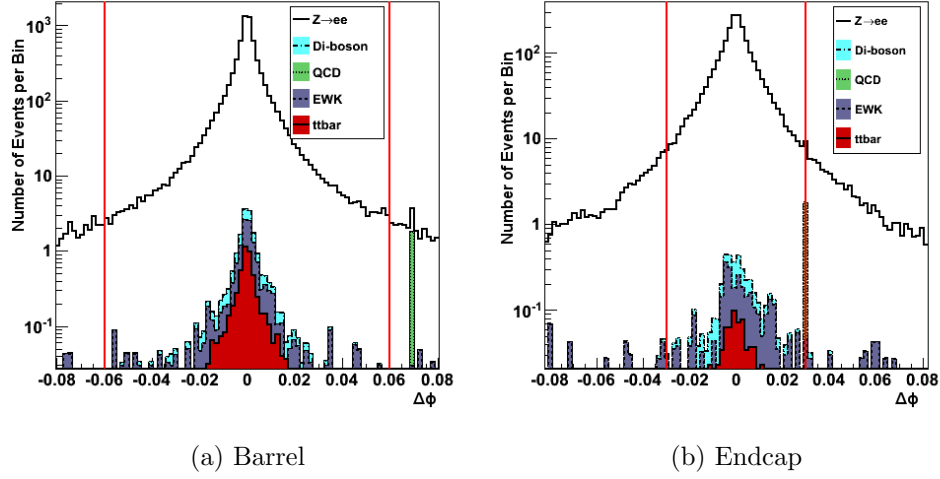


Figure 6.8:  $\Delta\phi_{in}$  electron identification variables after  $E_T$ , conversion rejection, isolation, and  $\Delta\eta_{in}$  cuts. A low  $\Delta\phi_{in}$  indicates a good match between the electron candidate's supercluster and track. Values shown for (a) barrel and (b) endcap. The vertical line shows where the cut was made.

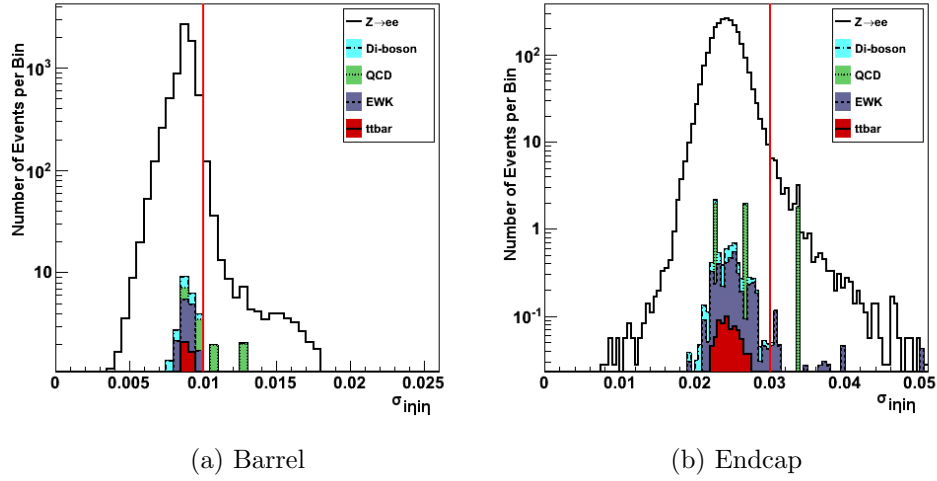


Figure 6.9:  $\sigma_{in\eta}$  electron identification variables after  $E_T$ , conversion rejection, isolation,  $\Delta\eta_{in}$ , and  $\Delta\phi_{in}$  cuts.  $\sigma_{in\eta}$  is a measure of the spread of the electron candidate's energy deposite in  $\eta$ . A true electron is expected to be relatively narrow in  $\eta$ . Values shown for (a) barrel and (b) endcap. The vertical line shows where the cut was made.

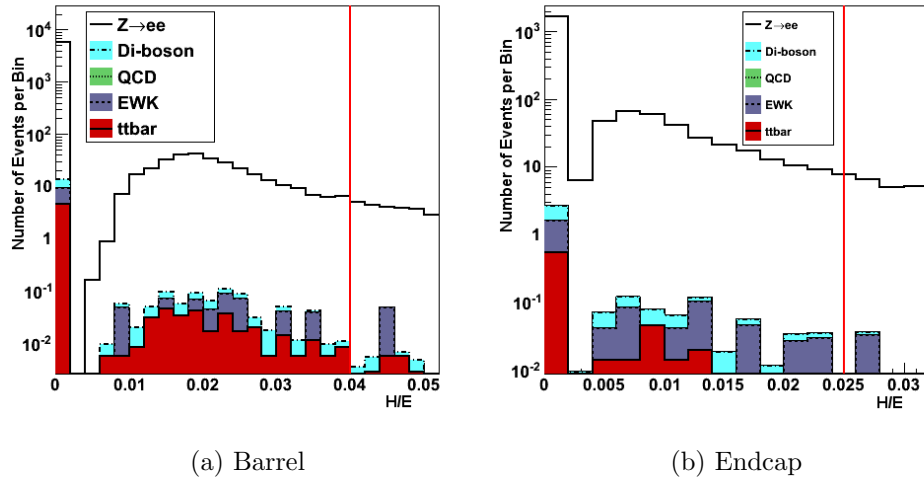


Figure 6.10: H/E electron identification variables after  $E_T$ , conversion rejection, isolation,  $\Delta\eta_{in}$ ,  $\Delta\phi_{in}$ , and  $\sigma_{in\eta}$  cuts. H/E is the ratio of the electron candidate's energy deposited in HCAL to that deposited in ECAL. A true electron is expected to deposit relatively little energy in the HCAL. Values shown for (a) barrel and (b) endcap. The vertical line shows where the cut was made.

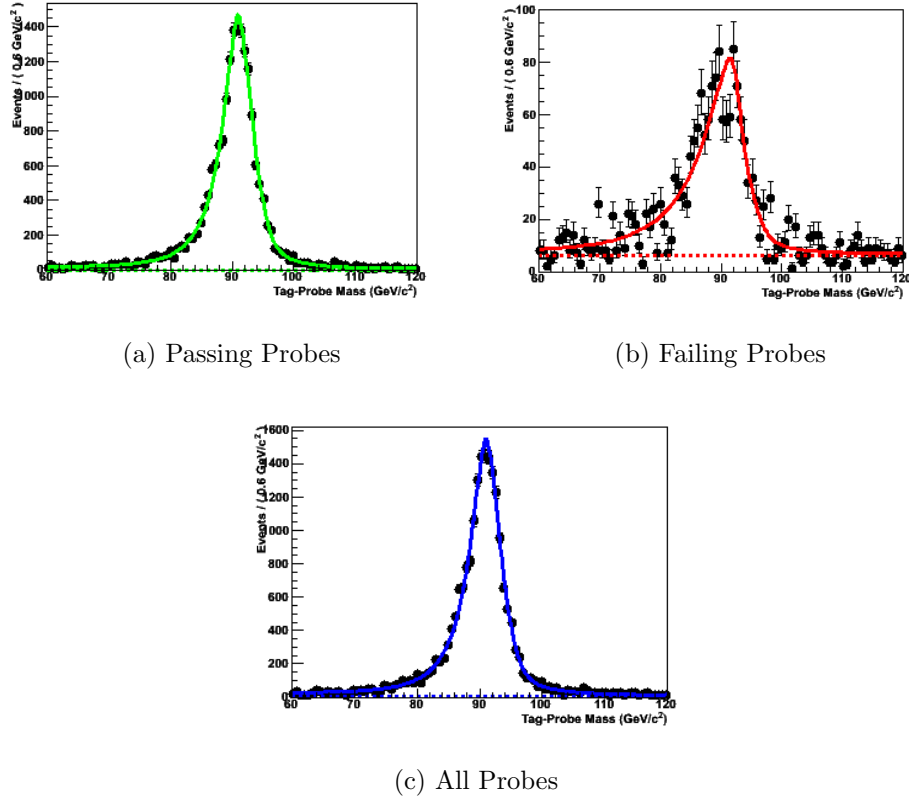


Figure 6.11: Example of tag-and-probe fits, for the isolation selection step in the barrel: (a) shows passing probes only, (b) shows failing probes only, and (c) shows the fit for all probes. Black points are data, the solid line is the signal lineshape, and the dotted line is the background lineshape.

## Chapter 7

### Analysis Method

The previous chapter explained how the data events used in the analysis were selected. The endpoint of that chapter was a set of  $Z \rightarrow e^+e^-$  candidate events: events that had two well-reconstructed electrons with an invariant mass between 60 and 120 GeV. This chapter explains the remaining ingredients in the process of extracting the cross section. This includes in particular estimating the number of background events, as well as determining the uncertainty inherent in each component and combining the uncertainties into one overall value.

#### 7.1 Background Subtraction

One of the ingredients in the cross section formula (see Section 1.5) is the number of signal events. However, it is expected that some number of non-signal (background) events will look enough like signal events to pass the full selection. These background events need to be accounted for in the final calculation to arrive at the most accurate result. Therefore, the number of background events should be estimated and subtracted from the total number of events; this estimation can be done in a variety of

ways. The methods used in this analysis are detailed in the following sections.

### 7.1.1 Monte Carlo Estimation

One estimate of the number of background events can be made directly from the Monte Carlo simulation, by counting the number of simulated events that pass the full selection. The numbers of passing events for the simulated background samples used are shown in Table 7.1, with a total of 18.5 events. The statistical error on this number is 4.3 events. However, the accuracy of this method may be questionable due to unaccounted differences between the simulation and real data. In particular, the detector may not be correctly modeled in the simulation, causing slight differences in event numbers that are non-negligible at this level. Therefore, data-driven methods of background subtraction are also used, and the results from all the methods are checked against each other to confirm the accuracy of each method.

Table 7.1: Number of events passing full selection for each background, estimated from Monte Carlo simulation.

Background Sample	Number of Events
Wenu	0.36
Wtaunu	0.0
Ztautau	6.4
Electroweak Total	6.7
ttbar	5.8
QCD	0.0
WW	1.5
WZ	1.4
ZZ	3.0
Di-boson Total	6.0
Total Background	18.5



### 7.1.2 Template Method

The template method is a data-driven method of estimating the background contribution in a selected data sample. In general, it uses modified cuts to select data events that are especially likely to be signal or background; these subsamples are called templates. Extra-tight cuts select a “signal-rich” sample, while a combination of loose and inverted cuts select a “background-rich” sample. A particular selection variable is chosen which has significantly different distributions for signal and background; here, the relative tracker isolation variable is used. The template method compares the distributions of that variable from the selected signal and background templates to the distribution from the full data sample. Essentially, the method determines what combination of the signal and background templates best fits the data distribution, in an effort to determine what fraction of the data sample is signal and what fraction is background. This method is only useful to determine the background from QCD; its technique relies on “background” electrons being qualitatively different from “signal” electrons (measured by the variable being used), but electrons from interactions similar to the signal interaction, such as  $W \rightarrow e\nu$ , are also high-quality or “signal” electrons. Objects arising from QCD interactions that are identified as “electrons” are more likely clusters of hadronic particles that come out looking like electrons, so they can be distinguished from “good electrons” and therefore the template method can identify them as background.

### 7.1.2.1 Template Definitions

Several new working points, based on WP80 (see Section 6.2.1), were defined to select the signal-like and background-like template samples, as well as the data distribution used in the comparison. Specific cut values for each working point are given in Table 7.2, as well as how each of the working points used in the template method is modified with respect to WP80. Cut values changed with respect to WP80 are displayed in italics.

The first working point, used to select the data, is called “Semi-Tight” and is identical to WP80 except for the removal of its relative track isolation requirement. This is solely to allow the full spectrum of track isolation values to be examined. All events with two electrons passing the Semi-Tight working point are included in the data sample.

The working point used to select the “signal-rich” data sample is called “Tight” and is based on the Semi-Tight working point but with a few cuts made tighter. (This is to ensure a very pure sample; however, a very tight working point would not work for standard data selection because its efficiency is lower – it cuts out too many good events. For the template method, though, a lower number of events is sufficient.) The tighter cut values were taken from WP70, another of the standard working points. Specifically, the values for  $\Delta\phi_{in}$  in both the barrel and the endcap,  $H/E$  in the barrel, and  $\Delta\eta_{in}$  in the endcap were tightened. To select the signal template sample, each event was required to have two electrons passing the Tight working point, and the two electrons were required to have opposite signs.

The final working point used for the template method is the “Loose” working

point, which is used in selecting the background template. The Loose working point is modeled on the Semi-Tight working point, as is the Tight, but for the Loose working point all the thresholds for the isolation and electron isolation variables are increased by a factor of 5. In addition, in order to get enough data for a reasonable background template, the ECAL isolation variable had to be further loosened, from 0.07 to 2.5 in the barrel and from 0.05 to 1.0 in the endcap, and the supercluster  $E_T$  cut had to be lowered from 25 GeV to 20 GeV. Events selected for the background template must have two electrons, one passing the Semi-Tight working point and one passing the Loose, and these two electrons are required to have the same sign in order to reject signal.

Table 7.2: Summary of the standard working point as well as the working point definitions used in the template method. “B” denotes the cut for the barrel, while “E” stands for the endcap. Italics indicate a cut changed relative to WP80.

Cut Variable	WP80		Semi-Tight		Tight		Loose	
	B	E	B	E	B	E	B	E
Conversion Rejection								
missing hits	0	0	0	0	0	0	0	0
dist	0.02	0.02	0.02	0.02	0.02	0.02	0.02	0.02
$\delta \cot \theta$	0.02	0.02	0.02	0.02	0.02	0.02	0.02	0.02
Relative Isolation								
ECAL	0.07	0.05	0.07	0.05	0.07	0.05	<i>2.5</i>	<i>1.0</i>
HCAL	0.1	0.025	0.1	0.025	0.1	0.025	<i>0.5</i>	<i>0.125</i>
track	0.09	0.04	<i>N/A</i>	<i>N/A</i>	<i>N/A</i>	<i>N/A</i>	<i>N/A</i>	<i>N/A</i>
Electron Identification								
$\sigma_{in\eta}$	0.01	0.03	0.01	0.03	0.01	0.03	<i>0.05</i>	<i>0.15</i>
$\Delta\phi_{in}$	0.06	0.03	0.06	0.03	<i>0.03</i>	<i>0.02</i>	<i>0.3</i>	<i>0.15</i>
$\Delta\eta_{in}$	0.004	0.007	0.004	0.007	0.004	<i>0.005</i>	<i>0.02</i>	<i>0.035</i>
$H/E$	0.04	0.025	0.04	0.025	<i>0.025</i>	0.025	<i>0.2</i>	<i>0.125</i>
SC $E_T$	25 GeV		25 GeV		25 GeV		<i>20 GeV</i>	

The mechanics of the fit are done by the ROOT class `TFractionFitter` [42], whose purpose is to perform the exact sort of fit needed for the template method. It determines the composition of template distributions that best fits a given “data” distribution using a likelihood fit. Statistical uncertainties in both the templates and the data are taken into account in the fitting process.

#### 7.1.2.2 Results

The relative tracker isolation distributions of the signal and background templates are shown in Figure 7.1. Each curve independently integrates to 1 and shows the fraction of events of the given type with relative tracker isolation in each bin. The background (dotted, red) has a much higher fraction of events with higher values of isolation than the signal (solid, black), which has a much higher fraction of events with lower values. The lowest bin contains 90% of the signal template compared with around 65% of the background template. These features enable the template method in general and the `TFractionFitter` in particular to fit the shape of the templates to the distribution of the data. The data distribution is shown in Figure 7.2 as the hollow circles (black), while the fit as determined by the `TFractionFitter` is displayed as asterisks (red). The agreement is very good, showing that `TFractionFitter` was able to make a good match between the data and its combination of templates.

Over the full range of the relative tracker isolation values used for the template fit, the fraction of signal was determined to be  $0.998 \pm 0.014$ , while the fraction of background was calculated to be  $0.0016 \pm 0.0020$ . However, the signal fraction over the full range is not useful, because this includes background events that would fail the tracker isolation selection cut. Therefore, the tracker isolation cut is effectively

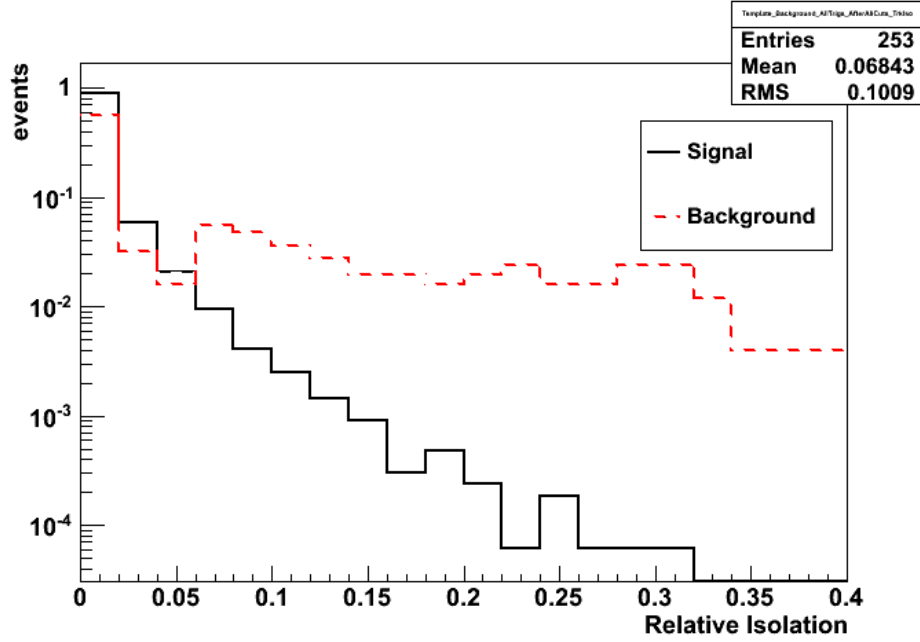


Figure 7.1: Shapes of signal and background templates used in template method of background subtraction. Each curve independently integrates to 1 and shows the fraction of events of the given type with relative tracker isolation in each bin. The solid (black) curve represents signal and the dotted (red) shows background.

reapplied by only looking at events which pass the cut. This is done by integrating the number of signal and background events below the threshold and redetermining the signal and background fractions, represented in the formula

$$f_{sig}^{thresh} = \frac{f_{sig} \times n_{sig}^{thresh}}{f_{sig} \times n_{sig}^{thresh} + f_{bg} \times n_{bg}^{thresh}}$$

which in essence scales the signal fraction according to the relative number of events below the threshold. In this case  $f_{sig}$  and  $f_{bg}$  are the signal and background fractions determined from the full isolation spectrum, while  $f_{sig}^{thresh}$  is the signal fraction below the isolation threshold.  $n_{sig}^{thresh}$  and  $n_{bg}^{thresh}$  are the integrated signal and background event numbers below the threshold. Since the barrel and endcap thresholds for relative

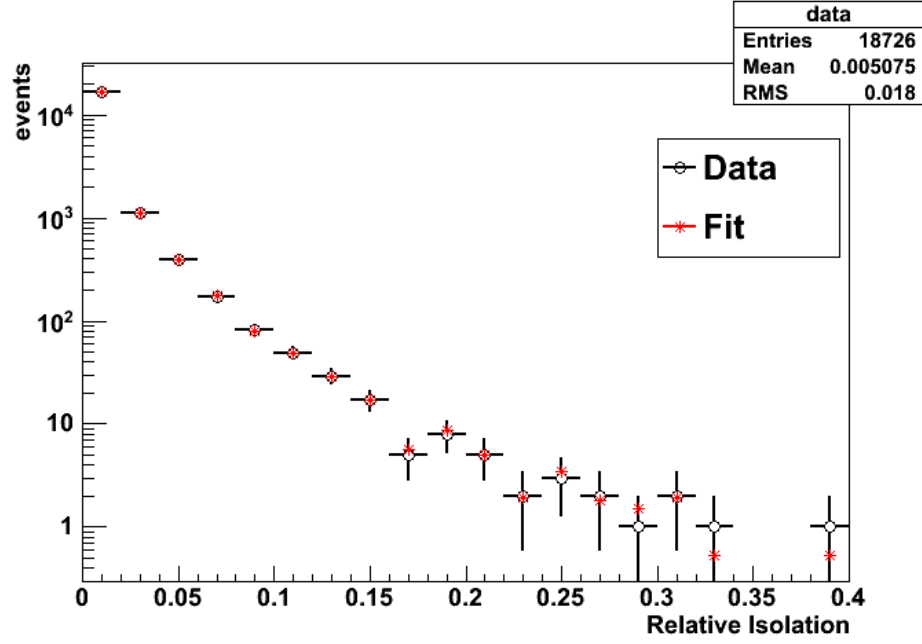


Figure 7.2: Results of template fit to data. The relative track isolation distribution for the data sample is shown as the hollow circles (black), while the TFractionFitter-determined template fit, using a combination of the signal and background templates, is shown as the asterisks (red).

tracker isolation are different, the integration and fraction redetermination was performed with each threshold separately. However, the differences in the final fractions were negligible (non-existent within significant figures), so using the barrel threshold vs. the endcap threshold was determined not to be a significant factor. The signal fraction below the threshold was determined to be  $1.000 \pm 0.014$ , and the background fraction  $0.000 \pm 0.002$ . It is expected that the background fraction below the cut threshold would be lower than over the entire spectrum, since more of the background distribution was above the cut threshold than the data distribution.

The signal and background fractions of the data sample determined both from the full isolation spectrum and from the spectrum below the cut threshold are shown

in Table 7.3.

Table 7.3: Signal and background fractions of data sample, for both the full relative tracker isolation spectrum and for the part of the spectrum below the cut threshold.

	Full spectrum	Below threshold
Signal fraction	$0.998 \pm 0.014$	$1.000 \pm 0.014$
Background fraction	$0.0016 \pm 0.0020$	$0.000 \pm 0.002$

The background fraction for the data sample measured below the isolation cut threshold translates to a event count of  $0 \pm 16.8$  events. (It should be recalled that this method is only considered valid for estimating QCD background.) The relative uncertainty on the number of signal events corresponding to the error (16.8 events) is 0.2%.

### 7.1.3 Sideband Subtraction

An additional method of estimating background was used, to cross-check the other two. The sideband subtraction method involves fitting the invariant mass peak with a lineshape to model the signal plus one to model the background. This is similar to the template method used in the previous section, in that a distribution is fitted to a composition of signal and background contributions. However, the sideband subtraction method uses a different variable distribution, the invariant mass peak, as well as a different set of components with which to fit the distribution. The name “sideband subtraction” refers to taking the distribution in the regions next to the peak, the “sidebands,” to represent the background part of the contribution, extrapolating it into the peak area, and subtracting it from the total distribution to leave only the signal contribution.

The data invariant mass spectrum is fitted with the same lineshapes used to determine the efficiency with the tag-and-probe method (see Section 6.2.2.2). The data is fit with the  $Z \rightarrow e^+e^-$  spectrum shape taken from the generator-level, convolved with a Crystal Ball function times a Gaussian function, which represents the signal, while using an exponential function to represent the background. The resulting fit is shown in Figure 7.3. Figure 7.3a shows the fit in linear scale, while Figure 7.3b shows the same plot in logarithmic scale. The total composition of lineshapes is shown as the solid line. The background contribution is shown as a dotted line, and is only visible in Figure 7.3a, the linear-scale plot. In logarithmic scale the exponential contribution is drawn around  $10^{-3}$  and hence is not displayed on the logarithmic-scale plot.

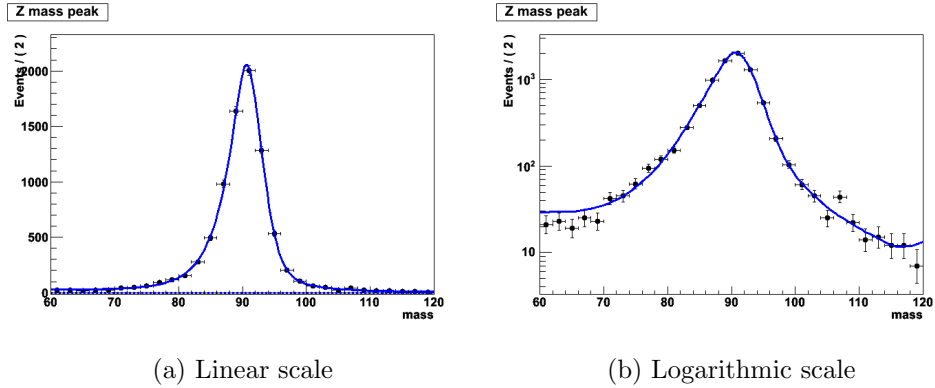


Figure 7.3: Fit of  $Z \rightarrow e^+e^-$  invariant mass peak for the purpose of background subtraction. (a) shows the fit in linear scale, while (b) shows the same plot in logarithmic scale. The total composition of lineshapes is shown as the solid line. The background contribution is shown as a dotted line, and is only visible in (a), the linear-scale plot. In logarithmic scale the exponential contribution is drawn around  $10^{-3}$  on the vertical scale and hence is not displayed on the logarithmic-scale plot.

In general it appears that the agreement of the fit with the actual data points is quite good. However, there are certain features of the fit that bear explaining. In



particular, at the lower and upper tails of the peak, the fit appears to be higher than the data points, and at the upper end an “uptick” in the fit curve appears. This is due to statistical fluctuations in the generator-level  $Z \rightarrow e^+e^-$  spectrum histogram. That histogram is very finely binned, and small fluctuations affect the shape of the final fit. The discrepancy at the lower end is likewise due to the shape of the generator-level histogram. The contribution of the background function to the overall fit is negligible. In addition, there appears to be a “shoulder” in the data points between about 75 and 80 GeV, as well as a fluctuation around 108 GeV. At this point in time these features in the shape are not understood but have been seen in other analyses as well. However, since they involve relatively few events, and because the analysis does not largely depend on the shape of the spectrum, for this analysis they can be ignored.

The composition of signal and background functions to the overall lineshape gives the number of background events to be  $0 \pm 14$  events.

#### 7.1.4 Comparison of Background Subtraction Methods

The three methods of background estimation detailed in the previous sections have yielded roughly consistent results, summarized in Table 7.4. Both of the methods that looked at data arrived at a total of 0 background events. The template method only gives an estimate for QCD events, but the estimate from the invariant mass fit applies to all sources of background. The template method in particular took many iterations of the criteria to obtain a “background-like” sample large enough to work with, indicating that the selection cuts are very effective at eliminating background. Both independent methods of analysis give the same result. Furthermore, the errors on the results from both methods are approximately the value of the background predicted

by the Monte Carlo simulation. Therefore, the actual background is between 0 and 19 events and consistent with all three methods. For the purposes of this analysis, the most conservative values obtained with any of the three methods were taken for both the estimated number of background events and the error estimate. This yielded a background estimate of 19 events from the Monte Carlo estimate, and an error of 17 events from the template method.

Table 7.4: Summary of background estimates from the three different methods used in this analysis. All three methods give roughly consistent results. In general the most conservative values have been used. The error on the number of events from Monte Carlo includes only the statistical error.

Method	Background events
Monte Carlo	$18.5 \pm 4.3$ (stat)
Template Method	$0 \pm 16.8$
Sideband Subtraction	$0 \pm 14$

## 7.2 Estimation of Systematic Uncertainties

### 7.2.1 Introduction to Error Analysis

When making any sort of measurement it is essential to know how accurate the result is. This accuracy can be quantified in the “error” or “uncertainty” on a measurement, meaning the bounds around the measured value within which the true value can be assumed to lie. A measurement with a smaller error is therefore a more accurate or “better” result, and hence calculating the error on a result is an extremely important part of any analysis.

An uncertainty on a quantity can be expressed in two different ways. The first

way is as an absolute uncertainty, with the same units as the quantity, for example “20.0  $\pm$  0.2 grams.” The second way is as an uncertainty relative to the value of the quantity itself, such as “20.0 grams  $\pm$  1%.” The “1%” comes from the value of the absolute uncertainty divided by the value of the quantity: 0.2 grams/20.0 grams = 0.01 = 1%. The relative uncertainty is therefore unitless.

In order to combine the effects of different (independent) uncertainties, it is necessary to add them in quadrature, as shown:

$$\left(\frac{\delta X_{tot}}{X_{tot}}\right)^2 = \sum_{i=1}^N \left(\frac{\delta X_i}{X_i}\right)^2 = \left(\frac{\delta X_1}{X_1}\right)^2 + \left(\frac{\delta X_2}{X_2}\right)^2 + \dots + \left(\frac{\delta X_N}{X_N}\right)^2$$

where  $X$  is the value of the given quantity and  $\delta X$  is the absolute error, making  $\frac{\delta X}{X}$  the relative error. Here, *tot* denotes the total uncertainty and  $i = 1, 2, \dots, N$  the uncertainties from individual sources. Only the relative uncertainties can be combined in this way, due to the lack of different units. This formula may be understood conceptually by analogy to the  $x$ - $y$  coordinate plane, in particular the formula for a given point’s distance to the origin. In the same way the square of the total distance from zero is given as the sum of the squares of the (independent) component distances, the square of the “total uncertainty” is given by the sum of the squares of the individual (independent) component uncertainties. Instead of calculating a distance in coordinate space, this distance is calculated in “uncertainty space.”

In high energy physics the sources of uncertainty are generally divided into two categories: statistical and systematic. Statistical error arises from the fluctuations possible when counting elements in a population. The higher the number of elements used in the study, the more accurate the measurement is likely to be. In a high energy physics analysis this corresponds to the number of events used. The relative

statistical error on a measurement is equal to the square root of the total number of events divided by the total number of events:

$$\frac{\delta x}{x} = \frac{\sqrt{N}}{N}$$

Where  $x$  is the quantity being measured and  $N$  is the total number of events used. In our case, the statistical error on the final result of 8453 events is given by

$$\frac{\sqrt{8453}}{8453} = 1.1\%$$

The statistical error is fixed for a given number of events; the only way to reduce the statistical error is to analyze more events.

The second type of error, systematic error, encompasses everything else that may inadvertently affect the result of the analysis. The particular sources are specific to the analysis in question, ranging from slight differences in theoretical predictions, reflecting our incomplete knowledge of the subject, to possible miscalibrations of the detector, to possible biases inherent in reconstruction or identification algorithms. The error is evaluated by changing something in the analysis and seeing how much the result itself would change. Some changes have very little effect, while some have larger effects. In general, it is only necessary to account for the larger effects, “larger” being defined by the scale of the statistical uncertainty. If the systematic error due to a particular source is much smaller than the overall statistical error, its contribution to the total uncertainty is relatively very small, and it can safely be ignored. It is therefore standard to try to adjust an analysis if necessary such that its systematic error is at most about the same as the statistical error. Such corrections might include using a reconstruction method whose errors are shown to be lower, or doing a more

thorough analysis in which case some errors can be reduced.

### 7.2.2 Systematic Uncertainty Due to Luminosity

As one of the necessary components in the cross-section calculation, any uncertainty on the measurement of the luminosity is relevant to the final result. The luminosity is measured by the forward hadronic calorimeter (HF) and calibrated using Van der Meer scans, as explained in Section 3.3.8. The largest uncertainty in the luminosity measurement comes from the measurement of the beam current. Other sources include the possibility that the double-Gaussian shape does not completely model the beam shape, possible inaccuracies in the measurement of the beam positions, and possible changes in the beam size during the Van der Meer scans. For the 2010 dataset, the luminosity measurement has an accepted relative uncertainty value of 4% [43].

### 7.2.3 Systematic Uncertainties from Theory

Uncertainties in theoretical predictions do not necessarily play a role in an experimental measurement. However, the theoretical models do affect the calculation of the acceptance (see Section 6.2.2.1). The acceptance must inherently be obtained from Monte Carlo simulation, making it dependent on the individual model used. Since there are many different possible corrections to the given Monte Carlo modeling, all of these variations should be taken into account. The official CMS  $Z \rightarrow e^+e^-$  analysis calculated [41] uncertainties in the acceptance due to various elements of theory, and these are given here.

The POWHEG [30] Monte Carlo simulated data sample used in the analysis

(see Section 4.1.2.2) does not include corrections from either resummation or NNLO QCD corrections. Resummation is a method for dealing with the tendency of the cross section to become infinite at low transverse momentum when calculating cross sections up to a given order. NNLO corrections include QCD diagrams at next-to-next-to-leading order and can affect the event distributions, but POWHEG only calculates the cross section fully to next-to-leading order (NLO). There are tools that can make these additional calculations, in particular the ResBos event generator [44]. ResBos was used to calculate the uncertainty due to these missing corrections.

Cross section calculations using matrix elements are generally done up to a fixed order and depend on the renormalization and factorization scales, energy scales that act as cutoffs for what treatments can be used. Varying these scales can estimate the uncertainty due to the missing higher-order corrections. The scales were therefore varied each way by a factor of two and the maximum difference in results was taken, using FEWZ [32] to calculate the cross section.

There are several well-known parton distribution function (PDF) sets (Section 2.1.3), which describe the structure of the proton and therefore affect how the proton constituents may form a Z. The output of simulations using these PDFs vary slightly from one to another. Three different PDF sets were used: CT10 [10], MSTW2008 [11], and NNPDF2.0 [45]. The value of the acceptance with each PDF was calculated in order to determine the spread between the three sets. In addition, the error function corresponding to each PDF was evaluated, and these were combined with the acceptance spread over the PDFs.

The POWHEG Monte Carlo simulation sample used for the analysis also does

not fully account for next-to-leading-order (NLO) electroweak corrections, in particular loop diagrams. In addition, the existing corrections, namely final-state radiation (FSR), can be modeled in different ways which can lead to different results. To deal with these sources of uncertainty, a separate generator, HORACE [46] [47], was used to make the full set of loop-diagram corrections. Additionally, the HORACE output using only FSR corrections was compared with the standard simulation sample (already including FSR) to estimate the uncertainty due to the FSR modeling.

The uncertainty due to the PDF set used was found to be 0.9%, while the rest of the sources (resummation, NNLO corrections, higher-order QCD corrections, parton distribution functions, final-state radiation, and NLO electroweak corrections) contributed a total of 1.4%, for a combined value of 1.7% relative uncertainty.

#### **7.2.4 Other Sources of Systematic Uncertainty**

In addition to the analysis-independent uncertainty due to luminosity, and the uncertainty in the acceptance from the theoretical modeling, there are several sources of uncertainty specific to this analysis that also need to be accounted for.

##### **7.2.4.1 Electron Energy Scale**

A typical source of systematic uncertainty is the energy scale of the physics objects used in the analysis, depending on the type of physics object. The electron energy scale is determined by the accuracy of the electromagnetic calorimeter (see Section 3.3.5.1) at measuring the energy deposited by the particles passing into it. The response of the ECAL is measured using a test beam setup: particle beams of known energies are directed at the calorimeter material, and the response is recorded. This

response is then correlated with the original particle energies. However, the correlation may not be completely accurate. Scaling the electron energy by an amount slightly less than or greater than 1 and then observing the resulting change in the number of  $Z \rightarrow e^+e^-$  events gives an estimate of the systematic error due to the electron energy scale. Uncertainties of 2% and 3% for the ECAL barrel and endcap respectively were used as conservative values [48]. The electron energy was then multiplied by 1.02 or 1.03 for the upper-end calculation, and 0.98 or 0.97 for the lower-end calculation, according to their position (barrel or endcap). Scaling the energy up resulted in finding 0.82% more  $Z \rightarrow e^+e^-$  candidate events. On the other hand, scaling the energy down caused the loss of 1.07% of the events. These two changes were averaged to give an overall relative error of 0.95% for the final result.

#### 7.2.4.2 Monte Carlo Sample for Efficiency

As discussed in Chapter 4, any given Monte Carlo simulation does not necessarily give a completely accurate model of particle interactions. Therefore, since part of the efficiency calculation was based on Monte Carlo simulation samples, it is quite possible that the numbers derived from simulation are not fully accurate. This must be accounted for as a systematic uncertainty, by redoing the calculation using samples from different Monte Carlo generators. In addition to the standard POWHEG generator sample, two samples generated by PYTHIA were used, differing in their treatment of the underlying event (see Section 1.4): Tune Z2 [29] and Tune D6T [49]. The “Monte Carlo true” and “Monte Carlo tag-and-probe” efficiencies were evaluated with each sample. The difference was quantified by taking the maximum spread between the values for each of the three samples and dividing that number by 2. The



maximum difference in efficiency occurred between the POWHEG and PYTHIA D6T samples, with a difference of 2.37%. The total relative systematic uncertainty that can be attributed to variation in the Monte Carlo sample is therefore 1.19%.

#### **7.2.4.3 Fitting for Efficiency**

The efficiency calculations in Section 6.2.2.2 had associated systematic errors due to the quality of the fit, which are the errors shown in Table 6.7. The error on the final event selection efficiency is 0.0047 in terms of absolute error, or 0.76% relative error.

#### **7.2.4.4 Background Subtraction/Modeling**

As described in Section 7.1.4, the uncertainty on the number of background events was taken to be 17 events, from the template method. This produces a relative uncertainty on the number of signal events (and hence final cross section) of 0.2%.

#### **7.2.5 Summary of Uncertainties**

A summary of the uncertainties on the final cross section resulting from various sources is shown in Table 7.5. The luminosity measurement contributes 4% of uncertainty, statistics 1.1%, theoretical systematics 1.7%, and experimental systematics 1.7%, for a total of 4.8%.

Table 7.5: Summary of relative uncertainties from all sources including luminosity, theoretical uncertainties, and experimental uncertainties.

Source	Value
Luminosity Uncertainty	4%
Statistical Uncertainty	1.1%
Theoretical Systematics	1.7%
Experimental Systematics	1.7%
Electron Energy Scale	0.95%
MC Sample for Efficiency	1.2%
Efficiency Fitting	0.76%
Background Subtraction/Modeling	0.2%
All error sources combined	4.8%

# Chapter 8

## Results

The previous chapters have gone through the steps for each part of the analysis and arrived at the necessary ingredients for the cross section calculation. Now, the relevant distributions will be presented as a cross-check, and the components will be assembled into a final result: the  $Z \rightarrow e^+e^-$  cross section. The result will also be compared with theoretical calculation and with other results to check its validity.

### 8.1 Distributions of Electron Kinematic Variables

The spectra of the electron kinematic variables after the full event selection, including the invariant mass cut, of both data and Monte Carlo samples are shown in Figure 8.1: electron transverse momentum  $p_T$ , pseudorapidity  $\eta$ , and azimuthal angle  $\phi$ . These basic distributions could indicate problems with the data. Large shape differences in the electron  $p_T$  plot can be a sign of unexpected background in the data sample; the  $\eta$  and  $\phi$  distributions can indicate issues with reconstruction algorithms or detector alignment. For example, a problem specific to the calorimeter endcaps might show up in the  $\eta$  distribution. Similarly, a non-uniform  $\phi$  distribution would indicate a problem, since the physics interactions are expected to be symmetric about

the beam axis. Each plot in Figure 8.1 also displays a ratio plot, showing the ratio of data to Monte Carlo event numbers in each bin; these give a quantitative measure of disagreement. In general the data distributions agree fairly well with the Monte Carlo distributions, especially in bins with many events (small relative error bars). This agreement demonstrates that the Monte Carlo accurately models the data, i.e. that the effects of the cuts on the data sample are understood. This is especially relevant because it is known that the QCD subsamples used (“EM-enriched” and “BC to E,” Section 4.1.3) do not model the full QCD background, only the background events more likely to be mistaken for electrons (see Section 6.2.1). In addition, the agreement demonstrates the validity of the corrections derived from Monte Carlo (acceptance and true efficiency).

## 8.2 Invariant Mass Spectrum

As explained in Section 2.2, the invariant mass of a set of decay-product particles is essentially the mass of the original particle that decayed. It is defined mathematically by

$$M_{inv}^2 = \left(\sum E\right)^2 - \left\|\sum \mathbf{p}\right\|^2$$

where  $\mathbf{p}$  is the momentum and  $E$  the energy for a given particle;  $\sum$  denotes the sum over all particles – a vector sum in the case of momentum, while  $\|\mathbf{p}\|$  denotes the momentum’s magnitude. In our case, for a two-particle system, this can be written as

$$M_{inv} = \sqrt{(E_1 + E_2)^2 - \|\mathbf{p}_1 + \mathbf{p}_2\|^2}$$

The invariant mass distribution within the mass window for the electron pairs in the events surviving all selection cuts is shown in Figure 8.2. There are a total of 8453 data

events passing the full event selection. An explanation of how the different simulation samples were combined can be found in Section 4.1.3. To combine data with Monte Carlo samples, the ratio of the data and Monte Carlo selection efficiencies, 0.933 (taken from Table 6.7), was used as the scale factor. The peak around the Z mass (91 GeV) is clearly visible in both the Monte Carlo (lines) and data (points) distributions. The background contributions estimated from Monte Carlo simulation are shown as the colored (grayscale) areas. A slight shift in the peak position along the x-axis is evident, due to slight miscalibrations of the calorimeter response to given energies. The transparency of the ECAL crystals have changed over time due to radiation, and the corrections for this transparency loss were not fully developed at the time of the data reprocessing. This difference is accounted for in the systematic uncertainty due to the electron energy scale (see Section 7.2.4.1). The selected events are also divided into categories according to which part of the detector, barrel or endcap, each of their electron legs were located, and the resulting invariant mass spectra are shown in Figure 8.3. Agreement in each case is good to within the uncertainty. The agreement in the invariant mass plots supports the use of this set of candidate events in the cross section calculation.

### 8.3 Distributions of Z Kinematic Variables

Since a significant number of  $Z \rightarrow e^+e^-$  candidate events have been identified, it is useful to examine the kinematic properties of these events. Even though this analysis does not depend on these properties, comparing the distributions from the data with those from the simulated samples can provide an additional check of validity of the simulation.

Figure 8.4 shows the distributions of standard kinematic variables for the reconstructed  $Z$  candidates: transverse momentum, rapidity, and azimuthal angle. The data (black dots) is compared with the simulation including background samples (lines/filled areas). As the ratio plots show, the agreement is good in general; large error bars indicate bins where the event count is not high enough to give a very precise estimate (such as the higher range of the  $Z$   $p_T$  plot). However, there are areas in which there is an evident discrepancy between the data and the simulation, most notably along the outer edges of the  $Z$  rapidity plot. Possible causes might include a slightly inaccurate description of the particle interaction in the generator, or a slight miscalibration of the detector. Since the difference is slight and is not relevant to this analysis, though, it can safely be ignored and the general agreement accepted.

## 8.4 Cross Section Measurement

As explained in Section 1.5, the interaction cross section is calculated from the formula

$$\sigma \times \text{BR} = \frac{(n_{\text{total}} - n_{\text{background}})}{\mathcal{L} \times \epsilon \times A}$$

in which  $n_{\text{total}}$ ,  $n_{\text{background}}$ ,  $\mathcal{L}$ ,  $\epsilon$ , and  $A$  have been determined experimentally. The measured values for these quantities are given in Table 8.1.

Plugging the values into the formula gives 990 pb for the cross section. The sources of error in the measurement (see Section 7.2.5) add a relative uncertainty of 4.8%, corresponding to 48 pb, for a final result of

$$\sigma(pp \rightarrow Z/\gamma^*) \times \text{BR}(Z \rightarrow e^+e^-) = 990 \pm 40(\text{lumi}) \pm 11(\text{stat}) \pm 17(\text{theory}) \pm 17(\text{syst})\text{pb}$$

Table 8.1: Quantities used to calculate cross section.

Quantity	Value
Luminosity $\mathcal{L}$	36.1 pb <sup>-1</sup>
$n_{total}$	8453
$n_{background}$	19
Efficiency $\epsilon$	0.610
Acceptance $A$	0.387

## 8.5 Comparison to Theory

To facilitate comparison of the cross section with theory, the CMS collaboration prepared a “standard” theoretical cross section value with FEWZ (see Section 4.1.2.3), using the appropriate detector boundaries for the acceptance. The FEWZ theoretical value obtained was  $972 \pm 40$  pb. The experimental value,  $990 \pm 48$  pb, agrees with the theoretical value within the errors on both values (the difference is 1.9% relative to the theoretical value).

## 8.6 Comparison to Other Experiments

The published CMS vector boson cross section analysis [41] measured a value of 992 pb:

$$\sigma(pp \rightarrow Z/\gamma^*) \times \text{BR}(Z \rightarrow e^+e^-) = 992 \pm 40(\text{lumi}) \pm 11(\text{stat}) \pm 16(\text{theory}) \pm 18(\text{syst})\text{pb}$$

The published CMS analysis was very similar to this one, so it is expected that the numbers should agree very closely. The difference between them comes to 0.2%.

The ATLAS collaboration also performed an analysis of the vector boson production cross sections [50]. The selection criteria were slightly different from those used in CMS: the electron  $\eta$  range used was  $|\eta| < 1.37$ ,  $1.52 < |\eta| < 2.47$ , the electrons

were required to have a transverse energy of 20 GeV instead of 25, and the invariant mass range was 66 to 116 GeV instead of 60 to 120 GeV. Nevertheless, the analyses are comparable. The  $Z \rightarrow e^+e^-$  cross section obtained by ATLAS is

$$\sigma(pp \rightarrow Z/\gamma^*) \times \text{BR}(Z \rightarrow e^+e^-) = 972 \pm 33(\text{lumi}) \pm 10(\text{stat}) \pm 38(\text{theory}) \pm 34(\text{syst})\text{pb}$$

This compares well with the number obtained in this analysis, as well as with the official CMS result.

The LHC  $Z \rightarrow e^+e^-$  cross section results are shown along with the Tevatron results in Figure 8.5, as well as the FEWZ NNLO calculation. The points are offset horizontally for clarity. As discussed in Section 2.3.2, the measurements with CDF and D0 were made at a lower center-of-momentum collision energy. The increase in cross section with collision energy is clearly seen in the figure. The fact that the Tevatron measurements were done with  $p\bar{p}$  collisions instead of  $pp$  increases the cross section by a slight amount relative to  $pp$  at the same energy.



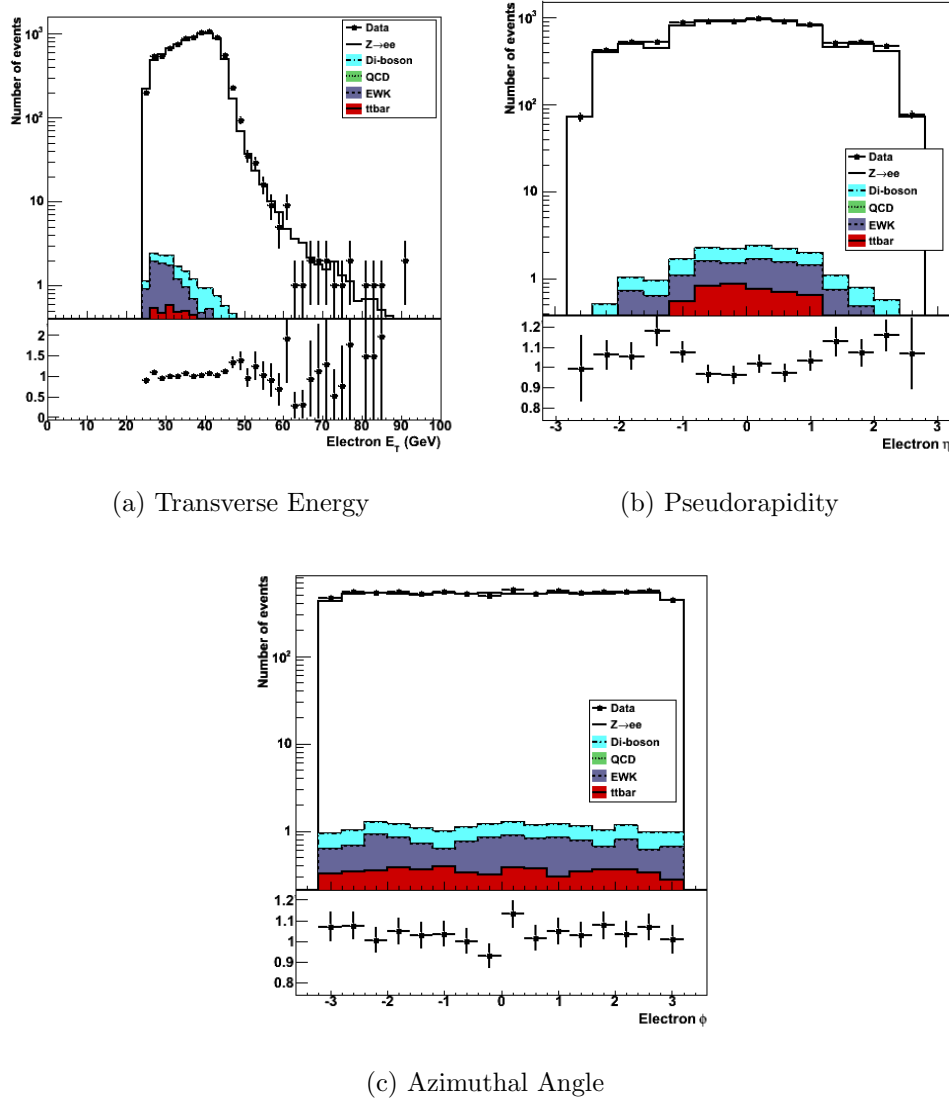


Figure 8.1: Spectra of reconstructed electron kinematic quantities after all event selection cuts. The plots show distributions for (a) electron transverse momentum  $p_T$ , (b) electron pseudorapidity  $\eta$ , and (c) electron azimuthal angle  $\phi$ . Each plot shows the data (black points with error bars) superimposed over the Monte Carlo distributions (colored/shaded areas with varied line styles). The signal Monte Carlo sample is shown by the solid black line against the white background. Most of the background has been cut out by the event selection. Below each plot is the ratio of the data to Monte Carlo event numbers for each bin.

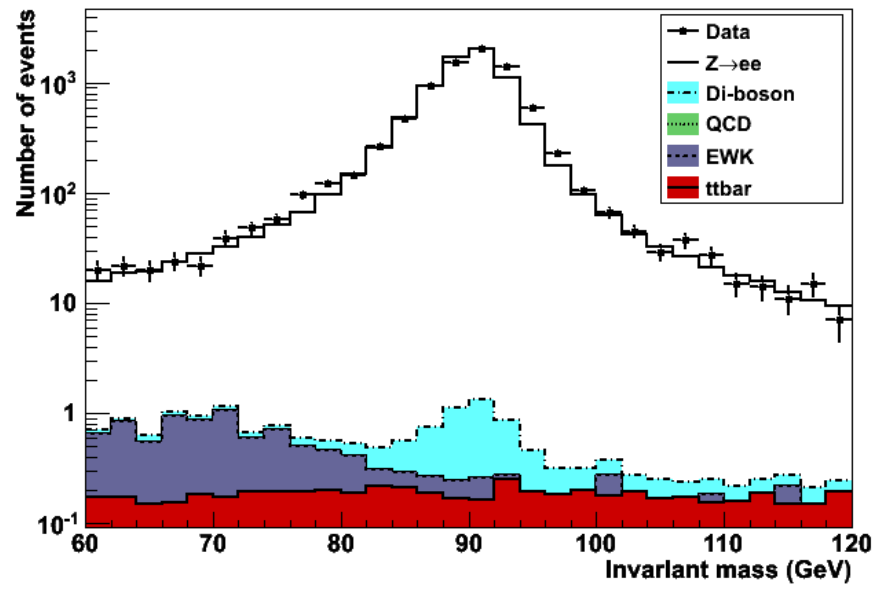


Figure 8.2: Electron-pair invariant mass after full selection. The peak around the Z mass (91 GeV) is clearly visible in both the Monte Carlo signal (solid line) and data (points) distributions. The background contributions estimated from Monte Carlo simulation are shown as the colored (grayscale) areas.

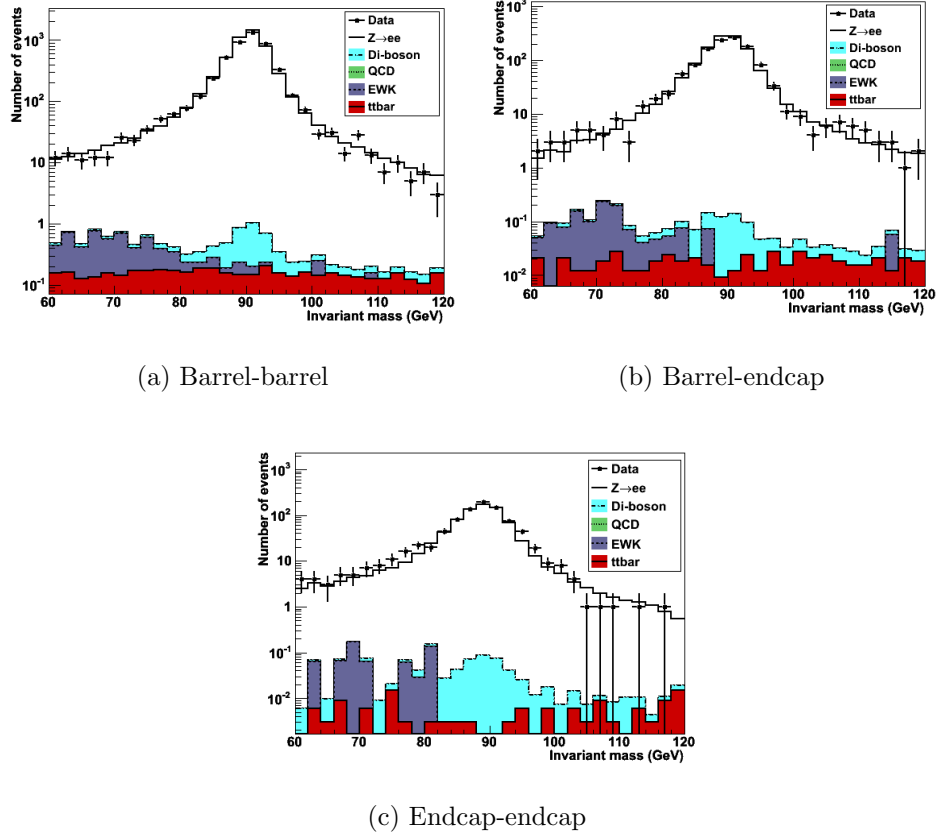


Figure 8.3: Electron-pair invariant mass by  $\eta$  region after full selection. Each combination of electron  $\eta$ -positions is distributed separately: both electrons in the barrel (a), one electron each in the barrel and the endcap (b), and both electrons in the endcap (c). Each plot shows the data (black points with error bars) superimposed over the Monte Carlo distributions (colored/shaded areas with varied line styles). The signal Monte Carlo sample is shown by the solid black line against the white background. Most of the background has been cut out by the event selection.

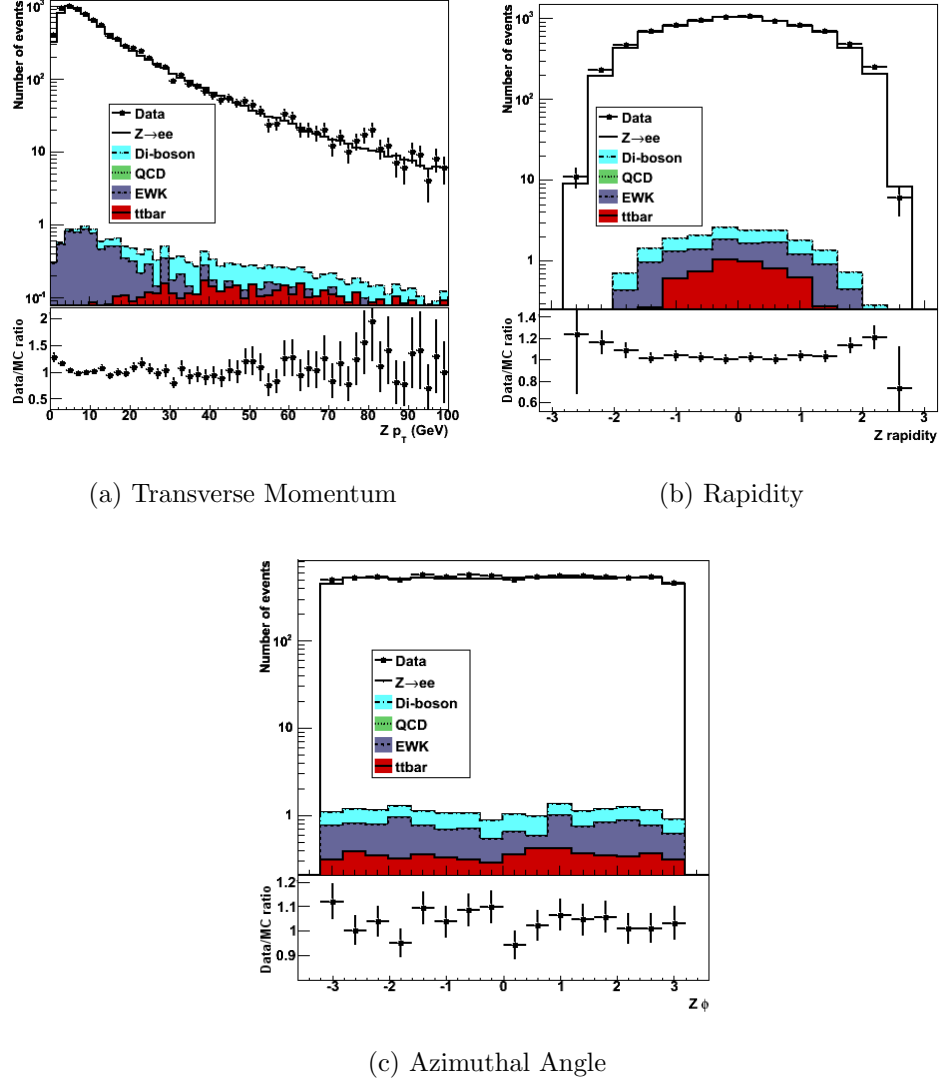


Figure 8.4: Kinematic quantities of Z candidates after full event selection: (a) Z transverse momentum  $p_T$ , (b) Z rapidity, and (c) Z azimuthal angle  $\phi$ . Each plot shows the data (black points with error bars) superimposed over the Monte Carlo distributions (colored/shaded areas with varied line styles). The signal Monte Carlo sample is shown by the solid black line against the white background. Most of the background has been cut out by the event selection. Below each plot is the ratio of the data to Monte Carlo event numbers for each bin.

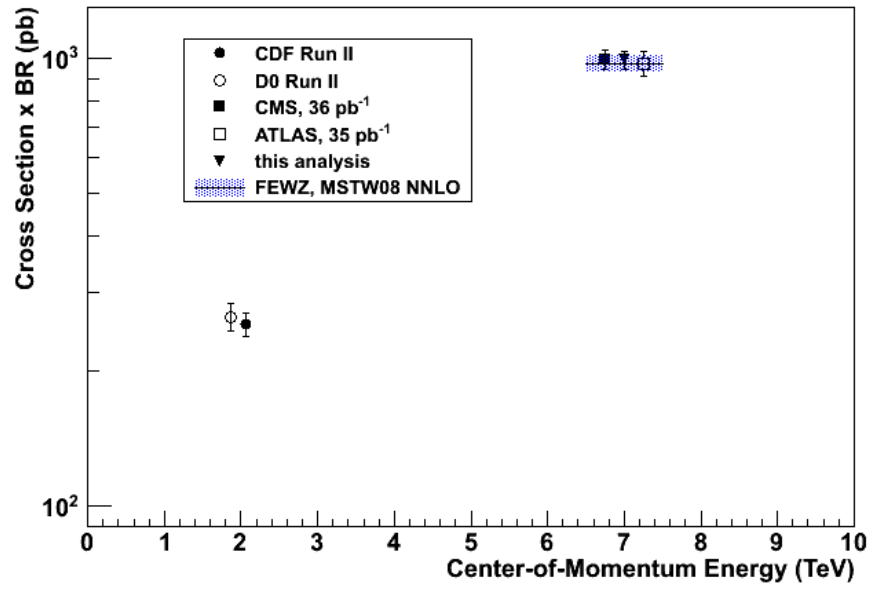


Figure 8.5: LHC  $Z \rightarrow e^+e^-$  cross section results, with Tevatron results and NNLO theory from FEWZ using MSTW08. The points are offset horizontally for clarity.

## Chapter 9

### Summary and Conclusions

This analysis measured the cross section of the  $pp \rightarrow Z \rightarrow e^+e^-$  interaction within an invariant mass window of 60 to 120 GeV, using  $36.1 \text{ pb}^{-1}$  of  $\sqrt{s} = 7\text{-TeV}$   $pp$  collision data. Each event was required to have passed the trigger and to have two well-reconstructed electrons, which resulted in 8453 events. The event selection efficiency was determined using the tag-and-probe method to be 0.610, and the acceptance was calculated using a POWHEG (NLO) Monte Carlo  $Z \rightarrow e^+e^-$  sample to be 0.387. Background was estimated from PYTHIA Monte Carlo samples, from a template method using signal- and background-like samples, and from a functional fit to the candidate invariant mass distribution. Systematic uncertainties were estimated by varying the electron energy scale, varying the Monte Carlo sample used for the efficiency ratio, and taking errors on the fit where fits were performed. The error on the acceptance due to theoretical uncertainties was taken from the official CMS analysis.

The cross section was determined to be

$$\sigma(pp \rightarrow Z/\gamma^*) \times \text{BR}(Z \rightarrow e^+e^-) = 990 \pm 40(\text{lumi}) \pm 11(\text{stat}) \pm 17(\text{theory}) \pm 17(\text{syst})\text{pb}$$

This result is in agreement with the FEWZ (NNLO) prediction of  $972 \pm 40 \text{ pb}$ . In

addition, it agrees with the CMS official measurement of 992 pb, as well as with the ATLAS measurement of 972 pb.

The agreement of these results bodes well for CMS: the detector is well calibrated and can produce a solid measurement of standard model physics. This points toward a future of successful new measurements and exciting physics.

## Bibliography

- [1] S. Abachi *et al.*, “Search for high mass top quark production in  $p\bar{p}$  collisions at  $\sqrt{s} = 1.8$  TeV,” *Physical Review Letters*, vol. 74, no. 13, pp. 2422–2426, 1995.
- [2] F. Abe *et al.*, “Observation of top quark production in  $p\bar{p}$  collisions with the collider detector at fermilab,” *Physical Review Letters*, vol. 74, no. 14, pp. 2626–2631, 1995.
- [3] G. Arnison *et al.*, “Experimental observation of lepton pairs of invariant mass around 95-GeV/ $c^2$  at the CERN SPS collider,” *Phys. Lett. B*, vol. 126, p. 398, 1983.
- [4] P. Bagnaia *et al.*, “Evidence for  $Z^0 \rightarrow e^+ e^-$  at the CERN anti-p p collider,” *Phys. Lett. B*, vol. 129, p. 130, 1983.
- [5] CMS Collaboration, “CMS Physics Technical Design Report, Volume II: Physics Performance,” *Journal of Physics G: Nuclear and Particle Physics*, vol. 34, no. 6, p. 995, 2007.
- [6] CMS Collaboration, “CMS Physics Technical Design Report Volume I : Detector Performance and Software,” *CERN-LHCC-2006-001*, 2006.
- [7] R. Brun and F. Rademakers, “ROOT - an object oriented data analysis framework,” *Nucl. Inst. and Meth. in Phys. Res. A*, vol. 389, pp. 81–86, 1997.
- [8] F. Halzen and A. D. Martin, *Quarks and Leptons: an Introductory Course in Modern Particle Physics*. John Wiley and Sons, 1984.
- [9] Y. Fukuda *et al.*, “Evidence for oscillation of atmospheric neutrinos,” *Phys.Rev.Lett*, vol. 81, pp. 1562–1567, 1998.
- [10] H.-L. Lai, M. Guzzi, J. Huston, Z. Li, P. M. Nadolsky, J. Pumplin, and C.-P. Yuan, “New parton distributions for collider physics,” *Phys.Rev.D*, vol. 82, p. 074024, 2010.
- [11] A. D. Martin, W. J. Stirling, R. S. Thorne, and G. Watt, “Parton distributions for the LHC,” *Eur.Phys.J.C*, vol. 63, pp. 189–285, 2009.



- [12] J. Pumplin, D. R. Stump, J. Huston, H. L. Lai, P. Nadolsky, and W. K. Tung, “New generation of parton distributions with uncertainties from global QCD analysis,” *JHEP*, vol. 2002, p. 012, July 2002.
- [13] K. Nakamura et al. (Particle Data Group), “2011 Review of Particle Physics,” *Journal of Physics G*, vol. 37, no. 7A, p. 075021, 2010.
- [14] The ALEPH, DELPHI, L3, OPAL, SLD Collaborations, the LEP Electroweak Working Group, the SLD Electroweak and Heavy Flavour Groups, “Precision Electroweak Measurements on the Z Resonance,” *Phys. Rept.*, vol. 427, p. 257, 2006.
- [15] CDF Collaboration, “First measurements of inclusive W and Z cross sections from Run II of the Tevatron collider,” *Phys. Rev. Lett.*, 2004.
- [16] D0 Collaboration, “Measurement of the Cross Section for W and Z Production to Electron Final States with the D0 detector at  $\sqrt{s} = 1.96$  TeV,” *D0Note 4403-CONF*, 2004.
- [17] L. Evans and P. Bryant, “LHC Machine,” *Journal of Instrumentation*, vol. 3, no. 08, p. S08001, 2008.
- [18] CMS Collaboration, “The CMS experiment at the CERN LHC,” *Journal of Instrumentation*, vol. 3, p. S08004, 2008.
- [19] CMS Collaboration, *CMS TriDAS project: Technical Design Report; 1, The Trigger Systems*. Technical Design Report CMS, CERN, 2000.
- [20] P. Chumney, S. Dasu, J. Lackey, M. Jaworski, P. Robl, and W. H. Smith, “Level-1 regional calorimeter trigger system for CMS,” *Proceedings of Computing in High Energy Physics and Nuclear Physics*, 2003.
- [21] W. Adam et al., “The CMS high level trigger,” *Eur. Phys. J.*, vol. C46, pp. 605–667, 2006.
- [22] CMS Collaboration, “Measurement of CMS Luminosity,” *PAS-EWK-10-004*, 2010.
- [23] S. van der Meer, “Calibration of the effective beam height in the ISR,” *CERN-ISR-PO/68-31*, 1968.
- [24] R. Steinhagen et al., “LHC beam stability and performance of the Q/Q’ diagnostics instrumentation,” *BIW10 Proceedings*, 2010.
- [25] CMS Collaboration, “CMS Luminosity Collision Data 2010.” <https://twiki.cern.ch/twiki/bin/view/CMSPublic/LumiPublicResults2010>.

- [26] M. A. Dobbs *et al.*, “Les Houches Guidebook to Monte Carlo Generators for Hadron Collider Physics,” 2004.
- [27] T. Sjöstrand, S. Mrenna, and P. Z. Skands, “PYTHIA 6.4 Physics and Manual,” *JHEP*, vol. 05, p. 026, 2006.
- [28] B. Andersson, G. Gustafson, G. Ingelman, and T. Sjöstrand, “Parton fragmentation and string dynamics,” *Physics Reports*, vol. 97, no. 2-3, pp. 31 – 145, 1983.
- [29] R. Field, “Early LHC underlying event data - findings and surprises,” 2010.
- [30] S. Alioli, P. Nason, C. Oleari, and E. Re, “NLO vector-boson production matched with shower in POWHEG,” *Journal of High Energy Physics*, vol. 2008, no. 07, p. 60, 2008.
- [31] Z. Was and P. Golonka, “TAUOLA as tau Monte Carlo for future applications,” *Nuclear Physics B - Proceedings Supplements*, 2004.
- [32] K. Melnikov and F. Petriello, “Electroweak gauge boson production at hadron colliders through  $O(\alpha_s^2)$ ,” *Phys.Rev.D*, vol. 74, p. 114017, 2006.
- [33] S. Agostinelli *et al.*, “Geant4 – a simulation toolkit,” *Nuclear Instruments and Methods in Physics Research Section A: Accelerators, Spectrometers, Detectors and Associated Equipment*, vol. 506, no. 3, pp. 250 – 303, 2003.
- [34] V. M. Ghete, “The CMS L1 trigger emulation software,” *CMS CR-2009/123*, 2009.
- [35] W. Adam, T. Speer, B. Mangano, and T. Todorov, “Track reconstruction in the CMS tracker,” *CMS NOTE 2006/041*, 2006.
- [36] S. Cucciarelli, M. Konecki, D. Kotlinski, and T. Todorov, “Track reconstruction, primary vertex finding and seed generation with the Pixel Detector,” *CMS NOTE 2006/026*, 2006.
- [37] W. Adam, R. Frühwirth, A. Strandlie, and T. Todorov, “Reconstruction of Electrons with the Gaussian-Sum Filter in the CMS Tracker at the LHC,” *CMS NOTE 2005/001*, 2005.
- [38] S. Baffioni, C. Charlot, F. Ferri, D. Futyan, P. Meridiani, I. Puljak, C. Rovelli, R. Salerno, and Y. Sirois, “Electron Reconstruction in CMS,” *CMS NOTE 2006/040*, 2006.
- [39] T. Miao, H. Wenzel, F. Yumiceva, and N. Leioatts, “Beam Spot Determination using Tracks,” *CMS NOTE 2007/021*, 2007.

- [40] P. Vanlaer, L. Barbone, N. D. Filippis, T. Speer, O. Buchmüller, and F.-P. Schilling, “Impact of CMS Silicon Tracker Misalignment on Track and Vertex Reconstruction,” *CMS NOTE 2006/029*, 2006.
- [41] CMS Collaboration, “Measurement of the W and Z inclusive production cross sections at  $\sqrt{s} = 7$  TeV with the CMS experiment at the LHC,” *CMS-PAS-EWK-10-005*, 2011.
- [42] “TFractionFitter.” <http://root.cern.ch/root/html/doc/TFractionFitter.html>.
- [43] CMS Collaboration, “Absolute luminosity normalization,” *CMS DPS-2011/002*, 2011.
- [44] C. Balasz and C.-P. Yuan, “Soft gluon effects on lepton pairs at hadron colliders,” *Phys.Rev. D*, vol. 56, pp. 5558–5583, 1997.
- [45] R. D. Ball, L. D. Debbio, S. Forte, A. Guffanti, J. I. Latorre, J. Rojo, and M. Ubiali, “A first unbiased global NLO determination of parton distributions and their uncertainties,” 2010.
- [46] C. M. C. Calame, G. Montagna, O. Nicrosini, and A. Vicini, “Precision electroweak calculation of the production of a high transverse-momentum lepton pair at hadron colliders,” *JHEP*, vol. 2007, no. 10, p. 109, 2007.
- [47] C. M. C. Calame, G. Montagna, O. Nicrosini, and M. Treccani, “Multiple photon corrections to the neutral-current Drell-Yan process,” *JHEP*, vol. 2005, no. 05, p. 019, 2005.
- [48] CMS Collaboration, “Electromagnetic calorimeter calibration with 7 TeV data,” *CMS PAS EGM-10-003*, 2010.
- [49] M. Albrow *et al.*, “Tevatron-for-LHC report of the QCD working group,” *Fermilab-Conf-06-359*, 2006.
- [50] ATLAS Collaboration, “A measurement of the total  $W^\pm$  and  $Z/\gamma^*$  cross sections in the  $e$  and  $\mu$  decay channels and of their ratios in  $pp$  collisions at  $\sqrt{s} = 7$  TeV with the ATLAS detector,” *ATLAS-CONF-2011-041*, March 2011.